

**Ordnung in Dünnen Filmen von Diblock-Copolymeren
durch Supramolekulare Strukturierung
(Order in Thin Films of Diblock Copolymers by
Supramolecular Assembly)**

DISSERTATION

zur Erlangung des akademischen Grades

Doktor rerum naturalium
(Dr. rer. nat.)

vorgelegt

am Fachbereich Chemie
der Fakultät Mathematik und Naturwissenschaften
der Technischen Universität Dresden

von

Ihor Tokarev

geboren am 28 May 1975 in Lviv, Ukraine

Gutachter: Prof. Dr. rer. nat. habil. M. Stamm

Prof. Dr. rer. nat. habil. T. Wolff

Prof. Dr. S. Minko

Eingereicht am: 24.03.2004

Tag der Verteidigung: 25.06.2004

Contents

List of abbreviations and symbols	VI
Introduction	1
Chapter 1. Molecular self-assembly in polymers and block copolymers. Theory and applications.	2
1.1. Self-assembly in block copolymers	2
• <i>Definitions and general remarks</i>	
• <i>Phase behavior of block copolymers</i>	
• <i>Block copolymers in thin films. Orientation of microdomains</i>	
• <i>Order in block copolymers</i>	
• <i>Applications of block copolymer thin films</i>	
1.2. Molecular assembly due to hydrogen bonding	14
• <i>Definitions, physical nature and classification of hydrogen bonds</i>	
• <i>Hydrogen bonds in polymers</i>	
1.3. Aim and outline of thesis	18
Chapter 2. Experimental	20
2.1. Sample preparation	20
• <i>Materials</i>	
• <i>Preparation of solutions of PS-<i>b</i>-P4VP+additive assembly</i>	
• <i>Preparation of PS-<i>b</i>-P4VP+additive assembly films</i>	
• <i>Preparation of bulk samples of S36V4 and S36V4+HABA assembly</i>	
• <i>Solvent vapor and temperature annealing of PS-<i>b</i>-P4VP+additive assembly films</i>	
• <i>Etching of S36V4+PDP assembly films</i>	
• <i>Sputter deposition of metals onto S36V4+HABA assembly templates</i>	
• <i>Nickel electrodeposition into S36V4+HABA assembly templates</i>	
• <i>Synthesis of brushes</i>	
2.2. Experimental methods	27
2.2.1. Ellipsometry	27
• <i>Principle</i>	
• <i>Ellipsometry of porous films</i>	

• <i>Instrumentation</i>	
2.2.2. Atomic force microscopy	29
• <i>Principle</i>	
• <i>Structural order analysis of AFM images</i>	
• <i>Instrumentation</i>	
2.2.3. Wide and small angle X-ray scattering	32
• <i>Principle</i>	
• <i>Instrumentation</i>	
2.2.4. X-ray reflectometry	34
• <i>Principle</i>	
• <i>Instrumentation</i>	
2.2.5. Grazing incidence small angle X-ray scattering	36
• <i>Principle</i>	
• <i>Instrumentation</i>	
2.2.6. X-ray photoelectron spectroscopy and photoemission electron microscopy	38
• <i>Principle</i>	
• <i>Instrumentation</i>	
2.2.7. Fourier transform infrared spectroscopy	39
2.2.8. Ultraviolet–visible spectroscopy	40
Chapter 3. Formation of PS-b-P4VP+HABA assembly	41
3.1. Spectroscopic study of P4VP+HABA assembly formation	41
• <i>Infrared spectra</i>	
• <i>UV-vis study of S36V4+HABA assembly</i>	
3.2. SAXS/WAXS study of S36V4+HABA assembly	44
Chapter 4. PS-b-P4VP+HABA assembly in thin films	47
4.1. S36V4+HABA films deposited from in 1,4-dioxane	47
• <i>Characterization of morphology</i>	
• <i>Characterization of the film porosity</i>	
• <i>Characterization of the chemical composition of the film interfaces</i>	
• <i>Discussion</i>	
4.2. S36V4+HABA films deposited from chloroform	54
• <i>Characterization of morphology</i>	

<ul style="list-style-type: none"> • <i>Characterization of the surface chemical composition</i> • <i>Discussion</i> 	
4.3. S33V8+HABA films	60
Chapter 5. Ordering of PS-b-P4VP+HABA films by solvent vapor annealing	63
5.1. Dioxane vapor annealing of S36V4+HABA films	63
5.2. Chloroform vapor annealing of S36V4+HABA films	69
5.3. Dioxane vapor annealing of S33V8+HABA films	70
5.4. Discussion	71
Chapter 6. Re-orientation of microdomains in PS-b-P4VP+HABA films by solvent vapor annealing	75
6.1. S36V4+HABA films	75
6.2. S33V8+HABA films	77
6.3. Discussion	78
Chapter 7. Study of PS-b-P4VP+PDP assembly in thin films	81
Chapter 8. Applications of templates from PS-b-P4VP+additive assembly films	90
8.1. Pattern transfer	90
8.2. Ordered arrays of metal nanoparticles by sputter deposition	92
<ul style="list-style-type: none"> • <i>Sputter deposition of chromium</i> • <i>Sputter deposition of gold</i> 	
8.3. Electrochemical growth of ordered arrays of Ni nanorods	102
Summary	105
References	109
Appendix A. List of publications	
Appendix B. Acknowledgment	
Appendix C. Versicherung	

List of abbreviations and symbols

AFM	Atomic Force Microscopy
BC	block copolymer
BCA	hydrogen-bond assembly of block copolymer and a low-molar-mass additive
BCC	body-centered cubic
c	speed of light ($2.998 \times 10^8 \text{ m} \times \text{s}^{-1}$)
C	cylindrical
$C\perp$	cylindrical perpendicular
$C//$	cylindrical parallel (in-plane)
d	film thickness
DC	direct current
di BC	dilock copolymer
dis	disordered state
DLS	Dynamic Light Scattering
e	1) electron charge ($1.602 \times 10^{-19} \text{ C}$); 2) ellipticity
<i>e.g.</i>	latin abbreviation meaning <i>for example</i>
<i>et al.</i>	latin abbreviation meaning <i>and others</i>
f	block volume fraction
FTIR	Fourier Transform Infrared
GISAXS	Grazing Incidence Small Angle X-ray Scattering
GPS	3-glycidoxypropyl trimethoxysilane
HABA	2-(4'-hydroxybenzeneazo)benzoic acid
$^1\text{H NMR}$	Proton Nuclear Magnetic Resonance
HPL	hexagonally perforated lamellar
J_{pulse}	pulse current density
k	wavevector
L	lamellar
$L\perp$	lamellar perpendicular
$L//$	lamellar parallel (in-plane)
LC	liquid crystalline
L_o	distance between adjacent microdomains
M	molarity (molar concentration)
M_n	chain number averaged molar mass
M_w	weight averaged molar mass
M_w/M_n	polydispersity
n	refractive index
N	total degree of polymerization
N_A	the Avogadro constant ($6.02214 \cdot 10^{23}$)

N_A and N_B	the average number of monomeric units in blocks A and B
NEXAFS	Near Edge X-ray Absorption Fine Structure
ODT	order-disorder transition
OOT	order-order transition
QMB	quartz microbalance
PBd	poly(1,2-butadiene)
PDP	3-pentadecyl phenol
PED	pulsed electrodeposition
PI	polyisoprene
PMMA	poly(methyl methacrylate)
PS	polystyrene
PS- <i>b</i> -PMMA	polystyrene- <i>block</i> -poly(methyl methacrylate)
PS- <i>b</i> -P2VP	polystyrene- <i>block</i> -poly(2-vinylpyridine)
PS- <i>b</i> -P4VP	polystyrene- <i>block</i> -poly(4-vinylpyridine)
PS- <i>b</i> -P4VP+additive	hydrogen-bond assembly of PS- <i>b</i> -P4VP and a low-molar-mass additive
PS- <i>b</i> -P4VP+HABA	hydrogen-bond assembly of PS- <i>b</i> -P4VP and 2-(4'-hydroxybenzene-azo) benzoic acid
PS- <i>b</i> -P4VP+PDP	hydrogen-bond assembly of PS- <i>b</i> -P4VP and 3-pentadecyl phenol
PSD	power spectral density
P(<i>S-r</i> -4VP)	random copolymer of styrol and 4-vinylpyridine
$P(q)$	form factor of scattered intensity
P2VP	poly(2-vinylpyridine)
P4VP	poly(4-vinylpyridine)
P4VP+HABA	hydrogen-bond assembly of P4VP and 2-(4'-hydroxybenzene-azo) benzoic acid
P4VP+PDP	hydrogen-bond assembly of P4VP and 3-pentadecyl phenol
q	scattering vector
q_z	z-projection of scattering vector (wavevector transfer)
R	reflection coefficient
R_g	gyration radius
RIE	reactive ion etching
RT	room temperature
$r_{N/C}$	ratio of areas of N 1s and C 1s peaks
r_{sw}	swelling ratio
S	spherical
SAXS	Small-Angle X-ray Scattering
sccm	standard cubic centimeters per minute, gas flow unit
SCF	self-consistent field
$S(q)$	structure factor of scattered intensity
S33V8	polystyrene- <i>block</i> -poly(4-vinylpyridine), $M_n = 41.0 \text{ kg}\times\text{mol}^{-1}$
S33V8+HABA	hydrogen-bond assembly of S33V8 and 2-(4'-hydroxybenzene-azo) benzoic acid

	acid
S36V4	polystyrene- <i>block</i> -poly(4-vinylpyridine), $M_n = 39.2 \text{ kg}\times\text{mol}^{-1}$
S36V4+HABA	hydrogen-bond assembly of S36V4 and 2-(4'-hydroxybenzene-azo) benzoic acid
S36V4+PDP	hydrogen-bond assembly of S36V4 and 3-pentadecyl phenol
T	temperature
TEM	Transmission Electron Microscopy
t_{pulse}	duration of current pulse
<i>tri</i> BC	triblock copolymer
UV	ultraviolet
UV-vis	ultraviolet-visible
vol%	volume percent
X	1) hydrogen-bond donor; 2) spatial coordinate
XPEEM	X-ray Photoemission Electron Microscopy
XPS	X-ray Photoelectron Spectroscopy
Y	1) hydrogen-bond acceptor; 2) spatial coordinate
α_c	critical angle
α_f	exit angle of X-ray beam (measured from the substrate plane)
α_i	incidence angle of X-ray beam (measured from the substrate plane)
Δ	ellipsometric angle
Φ	detector angle ($\Phi = \alpha_i + \alpha_f$)
χ	Flory-Huggins segmental interaction parameter
χ^N	incompatibility parameter
λ	wavelength of light
ρ	electron density
$r_e\rho$	scattering length density
σ	standard deviation
ψ	1) ellipsometric angle; 2) out-of-plane angle of scattered X-rays
2D	two-dimensional
\perp	perpendicular
//	parallel (in-plane)

Introduction

In this thesis we explore the phenomenon of molecular self-assembly in polymers, i.e. spontaneous aggregation of macromolecules into organized structures due to weak, noncovalent interactions (van der Waals forces, dipole-dipole interactions, hydrogen bonds). The typical examples of self-assembly in polymers are macrophase separation (polymer blends), microphase separation (block copolymers in melt and in solutions), crystallization, mesophase formation (liquid crystal polymers), formation of hydrogen- and π -bonded complexes. [För2002] Control of chemistry, architecture and size of macromolecules allows designing self-assembled materials with desired physical and chemical properties and phase structure with the feature size ranging from nanometers to microns. Some synthetic polymers reveal several different mechanisms of self-assembly giving rise to structures over many length scales. [Mut97, Ruo99] These functional polymeric materials have received growing attention in the last decade. In particular, they are considered to be promising for diverse nanotechnology applications. There are steady efforts in the direction of miniaturization and improvement of performance of integral circuits as well as electronic, optic, magnetic and electrochemical devices and sensors. In this respect, block copolymers which demonstrate self-assembly in ordered structures at the nanoscale are of great interest. Two-dimensional regular patterns formed by block copolymers in thin films have a potential application as templates for nanolithography and synthesis of a variety of inorganic and organic nanophase materials. [För98, Ham2003] Self-assembly in block copolymers is a subject of many theoretical studies and computer simulations. [Ham98] Considerable efforts made in this field improved our understanding of the physical processes underlying microphase separation of block copolymers in bulk and in thin films. However, there is a lack of theoretical works devoted to phase behavior of complex block copolymer systems, e.g. mixtures of block copolymer with homopolymers, low-molar mass additives or particles, concentrated solutions of block copolymers.

The objective of this thesis is development and study of novel block copolymer materials which demonstrate two different kinds of assembly: microphase separation giving rise to a number of ordered morphologies at the nanometer scale and molecular assembly due to hydrogen bonding. The latter was used to modify the properties of block copolymers by attachment of functional low-molar-mass molecules to one of the blocks. The low-molar-mass additive can be easily extracted from material resulting in ordered arrays of nanochannels in block copolymer matrix.

Chapter 1. Molecular self-assembly in polymers and block copolymers. Theory and applications

In this Chapter we give basic definitions used throughout the thesis and present the brief overview on theories of microphase separation in block copolymers and hydrogen bonding. We also review the recent experimental studies of hydrogen-bonded assembly of polymers and block copolymers in thin films followed by their applications for nanofabrication. In conclusion we give the outlook of the following experimental chapters.

1.1. Self-assembly in block copolymers

Definitions and general remarks

Block copolymers (BCs) are polymers composed of blocks of chemically dissimilar polymers joined together by covalent bonds in a variety of architectures. The important characteristics of BCs are

- the weight- or number-averaged molar masses (molecular weights) of BC and blocks denoted by M_w and M_n , respectively;
- the molar mass distribution M_w/M_n , which characterizes the BC polydispersity;
- the volume fractions of blocks f , which characterizes the BC composition.

Figure 1.1 shows typical BC architectures, which include linear diblock copolymers (*diBC*), triblock copolymers (*triBC*), multiblock copolymers, radial starblock copolymers and graft copolymers. [Ham98] Variety of methods of BC synthesis are given in reviews of S. Förster *et al.* [För98, För2002]. Living anionic polymerization is usually used when a narrow molar mass distribution is required.

Considering self-assembly of BCs, we should distinguish between *micellization* and *microphase separation*. [Ham98, För98] Micellization takes place in solutions of BCs composed of both soluble and insoluble blocks. Such BCs are called *amphiphilic*, implying dissimilarity in solubility of blocks in various solvents, not only in water. [För98] The *micellar core* is formed by insoluble blocks, which associate together to minimize unfavorable interactions with solvent, while the surrounding *corona* is formed by dissolved blocks. The polymer incompatibility drives self-assembly of bulk BCs into various ordered morphologies in melt. Spatial separation of blocks into different phases (*microdomains*) is restricted by the connectivity of the blocks. This kind of self-assembly is called microphase

separation. The two-length-scale self-assembly takes place in BCs containing either a crystallizable block (semicrystalline BCs) or a block with liquid crystalline (LC) side- or main-chain groups (LC BCs).

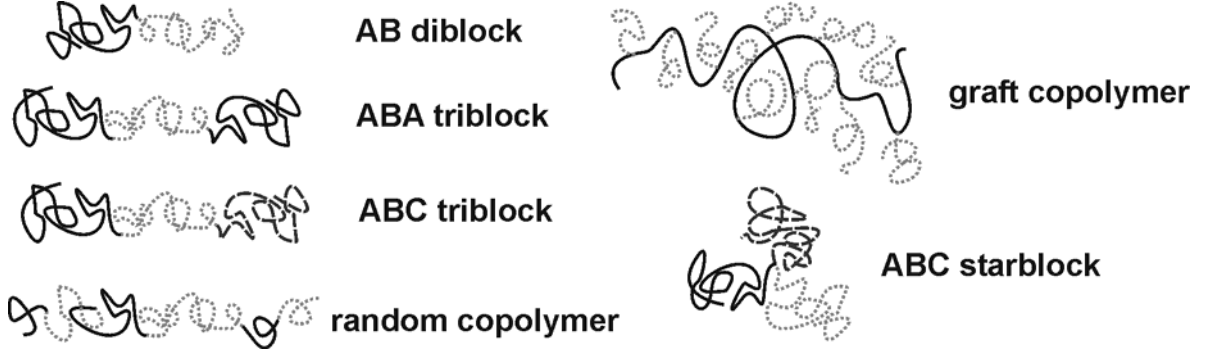


Figure 1.1. Typical architectures of BCs.

Phase behavior of block copolymers

BC microphase separation is well described considering two competing processes: the repulsion of dissimilar monomers and stretching of polymer chains. [Fre96] Incompatibility of blocks drives them to separate into a microdomain structure where the block junctions form microdomain interfaces. Thermodynamically, this process is parameterized by the enthalpy of demixing of polymer blocks ΔH_p . The surface to volume ratio and thus the interfacial free energy of the BC system decrease as the microdomains increase in size. Since the microdomain growth creates a density deficiency towards the microdomain center, the BC chains are stretched above the undisturbed Gaussian gyration radius R_g to fill the space. This process, which is accompanied by the reduction of the configurational entropy $\Delta S_{p,conf}$, opposes the block separation. The additional loss in entropy $\Delta S_{p,int}$ arises from confining the block junctions in the interfacial region. The sign of the change in Gibbs free energy

$$\Delta G_p = \Delta H_p - T\Delta S_{p,int} - T\Delta S_{p,conf} \quad (1.1)$$

indicates whether a transition from the phase with homogeneously mixed blocks (disordered state) to an ordered structure is favorable or not. The transition occurs when the enthalpic part dominates, *i.e.* $\Delta G_p > 0$. The demixing enthalpy ΔH_p is proportional to the dimensionless Flory-Huggins segmental interaction parameter χ , which exhibits the following temperature dependence:

$$\chi = C_1/T + C_2, \quad (1.2)$$

where C_1 and C_2 are BC dependent constants. The entropy penalty ΔS_p is inversely proportional to the total degree of polymerization N defined as

$$N = N_A + N_B, \quad (1.3)$$

where N_A and N_B are the average number of monomeric units in blocks A and B, respectively. The product χN expresses the enthalpic-entropic balance or, in other words, the degree of microphase separation. χN and the block volume fraction f completely determine symmetry and dimensions of microphase separated structure and are used for construction of BC phase diagrams.

BC phase behavior was the subject of numerous experimental and theoretical studies. In the literature, we find a number of examples of experimentally obtained BC phase diagrams. [Bat94, Kha95, Zha96, Sch96] Considerable success was achieved also in theoretical prediction of BC phase behavior. Satisfied results in explanation of experimentally observed BC morphologies were obtained within the mean field theories. The microphase separation theories were first developed for two limiting cases of strong and weak segregating BCs in melt [Hel75, Lei80] and later extended to BC solutions [Hon83, Whi92, Hua98a]. The phase diagrams of BCs in solutions was found to be similar to those calculated for melt. The Flory-Huggins parameter χ used in melt was replaced by the effective interaction parameter χ_{eff} in solutions.

The complete phase diagram of *diBC* in melt was calculated by M. W. Matsen *et al.* [Mat94, Mat96] within the full self-consistent field (SCF) theory (Figure 1.2). In the SCF calculations, the external mean fields acting on a polymer chain are calculated self-consistently with the composition profile. We start the detailed examination of the phase diagram for symmetric *diBC* ($f = 0.5$) at $\chi N \ll 10$, which corresponds to disordered (*dis*) state. The disordered state occurs at high melt temperatures, when the interactions between dissimilar monomers are weak. *diBC* chains behavior as Gaussian, *i.e.* $R_g \sim N^{1/2}$. Composition fluctuations reveal the characteristic length scale (observed in the scattering experiments) of

$$L^* \sim aN^{1/2}, \quad (1.4)$$

where a is the statistical segment (Kuhn) length. Decrease of T leads to growth of the interaction parameter χ , what is equal to the travel upwards in the phase diagram. The enthalpic-entropic balance is shifted and the transition from the disordered to microphase separated lamellar morphology occurs at $\chi N \approx 10$. The *diBC* phase behavior in the vicinity of the transition (called *order-disorder transition* or, shortly, *ODT*) was first examined by L. Leibler. [Lei80] Near the ODT, the *diBC* is weakly segregated and the composition profile is

nearly sinusoidal. The *di*BC is said to be in the weak segregation regime (or limit). L. Leibler applied Landau theory, where the mean field free energy was expanded with respect to the average composition profile. The theory predicts the second-order ODT at $(\chi N)_{\text{ODT}} = 10.5$. The equilibrium periodicity of lamellae L_o was found to be

$$L_o \approx 3.23R_g \sim N^{1/2}, \quad (1.5)$$

which indicates the Gaussian chain statistics. However, the more accurate SCF calculations [Mat96] give an exponent of 0.994. Further lowering T leads to sharpening of the interfaces between the blocks. The region of χN between 10.5 and ≈ 50 is considered as the intermediate segregation regime. [Ham98] The equilibrium periodicity of lamellae scales here with an exponent of 4/5. [Mat96] At $\chi N > 50$, the interfaces becomes very narrow and separated blocks form almost pure phases (microdomains). This region is referred to the strong segregation regime (or limit). The strong segregation approximation ($\chi N \rightarrow \infty$) to mean-field theories was realized by A. N. Semenov [Sem85]. He used electrostatic and classical elastic analogies to model the chain configurations. Calculations demonstrate strong and non-uniform stretching of *di*BC chains, which leads to an excess of chain ends in domain interiors. However, the stretching component of the free energy (per chain) scales as for a Gaussian chain

$$F_{\text{stretch}}/kT \sim L_o^2 / a^2 N. \quad (1.6)$$

The non-uniform chain stretching and the chain-end distribution are comprised in a constant prefactor. The stretching free energy is balanced by the interfacial free energy (per chain)

$$F_{\text{interface}}/kT \sim \gamma \sigma \sim Na \chi^{1/2} / L_o, \quad (1.7)$$

where $\gamma \sim \chi^{1/2} a^{-2}$ is the interfacial tension and $\sigma \sim Na^3 / L_o$ is the area per chain. Minimization of the total free energy with respect to interlamellar spacing results in the equilibrium periodicity of lamellae

$$L_o \sim a N^{\mu} \chi^{\nu}, \quad (1.8)$$

where $\mu = 2/3$ and $\nu = 1/6$. [Sem85] E. Helfand and Z. R. Wasserman [Hel76] used a narrow-interface approximation obtained $\mu = 9/14$ and $\nu = 1/7$. The theoretically estimated interfacial layer thickness in the strong segregation regime is

$$d_{\text{interface}} = a \chi^{-1/2}. \quad (1.9)$$

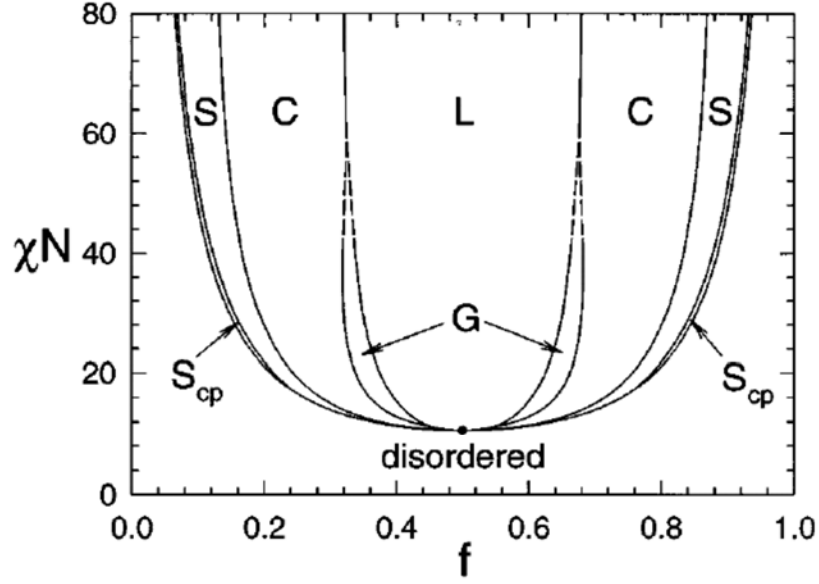


Figure 1.2. SCFT phase diagram of *diBC* melt.

Now we consider the effect of f on *diBC* morphology. As f appreciably deviates from 0.5, the flat lamellar interface can not be maintained by stretching of the major block. It becomes more energetically favorable to form curved interfaces. Also, in the intermediate segregation limit, increase of the *diBC* asymmetry results in the following sequence of *order-order transitions* (OOT): lamellar (L) \rightarrow bicontinuous cubic (*gyroid*) \rightarrow hexagonal cylindrical (C) \rightarrow body-centered cubic spherical (BCC S) morphologies \rightarrow *dis* state (Figure 1.3). SCF theory suggests that these OOTs are first-order transitions. The interfacial curvature is changed stepwise upon the transition from one morphology to another. All the listed morphologies are predicted to be stable. However, $L \leftrightarrow$ *gyroid* transition was demonstrated to proceed through the intermediate metastable *hexagonally perforated lamellar* (HPL) phase. [Haj97] The stability window of *gyroid* morphology was found to narrow with increase of χN completely disappearing in the strong segregation regime. Recent SCF calculations [Mat2001] give the following expressions for the L/C and C/S boundaries at $\chi N \sim 100$:

$$f_{LC} = 0.315 + 0.84 (\chi N)^{-1}, \quad (1.10)$$

$$f_{CS} = 0.114 + 2.07 (\chi N)^{-1}. \quad (1.11)$$

As it is seen in Figure 1.2, phase boundaries are near vertical (*i.e.* depend only on f) in the strong segregation regime and twist towards $f=0.5$ when approaching the ODT. Therefore, the curved phase boundaries allow the temperature induced OOT.

SCF calculations suggest ODT to the S morphology for all *diBC* compositions except $f = 0.5$ (the *critical point*). However, the direct transitions from the *dis* state to C , L [Bat94] and

gyroid [Haj94, Kha95] were experimentally observed for polystyrene-block-polyisoprene (PS-*b*-PI) in melt. Furthermore, the direct ODT to *C*, *gyroid* and *L* morphologies were detected in the solutions of PS-*b*-PI in selective and neutral solvents. [Han2000, Lod2003] This discrepancy arises primarily in inaccurate description of the *dis* state energy in the SCF theory. The direct first-order transitions were predicted by the mean-field theory, when small composition fluctuations were allowed. [Fre87] Furthermore, the second-order ODT at $f=0.5$ is replaced by a weak first-order transition and the critical point is shifted to

$$(\chi N)_{\text{ODT}} = 10.5 + 41.0 \bar{N}^{-1/3}; \quad (1.12)$$

A Ginzburg parameter $\bar{N} = 6^3(R_g^3 \rho)^2$, where ρ is the number density of *di*BC in melt, is typically of order 10^3 – 10^4 .

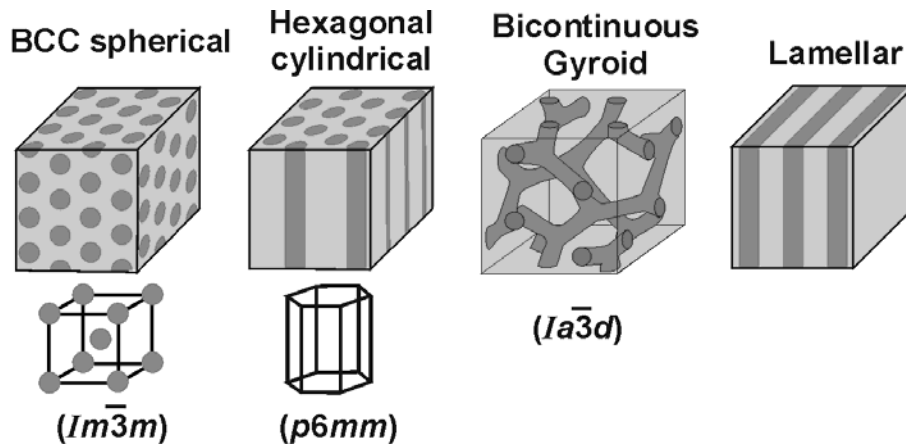


Figure 1.3. *di*BC morphologies.

In the phase diagram in Figure 1.2, the statistical segment lengths a of both blocks were chosen to be equal. If it is not the case, the phase diagram becomes asymmetric with phase boundaries shifted in the composition scale towards the block with larger a .

Block copolymers in thin films. Orientation of microdomains

To date, BC morphologies of thin films are attracted considerable attention of experimentalists and theoreticians. BCs prepared in thin films exhibit a variety of nanoscale in-plane patterns, which can be potentially used in a quickly growing area of nanotechnology. The phase behavior of BCs in thin films is considerably influenced by the interactions with air and substrate interfaces. Blocks having lower interfacial energy preferentially occupy the film interfaces. This typically induces the parallel alignment of *C* and *L* microdomains in respect to the film plane. [Fre87, Ana89]

Another feature of BCs in thin films, which arise from incommensurability of the bulk periodicity of parallel aligned microdomains L_0 with the film thickness d , is the formation of terraces. [Gre2001] In melt, BC film surface is reorganized so that the film thickness becomes quantized in accordance to L_0 (Figure 1.4). Terraces typically appear as islands or holes of the height L_0 , depending on the film thickness. In *di*BCs, quantization condition depends on whether the same block forms wetting layers at the film interfaces (symmetric wetting, Figure 1.4, left) or different blocks (asymmetric wetting, Figure 1.4, right). Thus, for films of the L morphology, the film thickness is quantized to values of

$$d = nL_0 \quad \text{and} \quad d = (n + 1/2)L_0 \quad (1.13)$$

for the symmetric and asymmetric wetting cases, respectively, where n is an integer.[Cou89, Rus89] The quantization relation for polystyrene-*block*-poly2-vinylpyridine (PS-*b*-P2VP) films of C morphology with asymmetric wetting of the interfaces found by M. H. Rafailovich *et al.* [Liu94] is a bit more complicated and expressed as

$$d = (n + \alpha)L_0 + \beta, \quad (1.14)$$

where $\alpha = 0.71$ is the fractional thickness of the first top cylindrical layer and β is the thickness of the lamellar layer adjacent to the substrate interface.

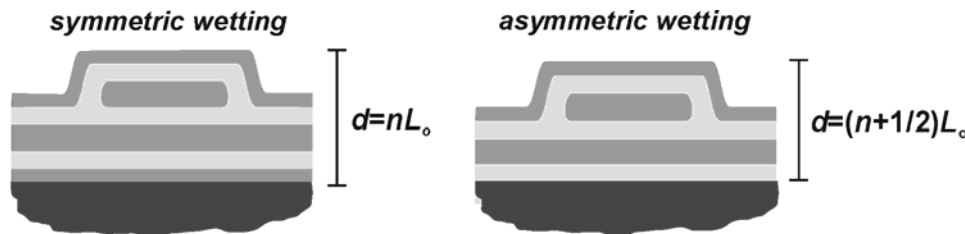


Figure 1.4. Quantization of the thickness of BC films.

Recently, influence of the confinement and the interfacial interactions on the morphology of *di*BCs in thin films were extensively studied theoretically within mean field theories [Pic97, Mat97, Hui2000] and Monte Carlo simulations [Gei99, Wan2001]. Unlike experimentally studied substrate supported films with free air surface, theoreticians deal with films confined in a slit, thus, omitting formation of terraces. The calculations exhibit qualitatively similar phase behavior for *di*BCs of C and L morphologies in the intermediate segregation regime. If there is no preference for blocks to wet the confining surfaces (neutral surfaces), L microdomains adopt perpendicular (\perp) orientation having lower free energy, independently on the slit width. Unlike, the orientation of C microdomains perpendicularly to

the boundaries becomes insensitive to the slit width for the surfaces having a slight energetic preference to the major block. Such asymmetry is attributed to balancing entropic preference for the minor block. [Hui2000, Qui2001] For a slit showing substantial preference to one of the blocks, parallel ($//$) orientation of microdomains is favored for all the slit widths except $(n + \frac{1}{2})L_0$ for the L morphology and $\frac{1}{2}L_0n + 0.75$ for the C morphology in the symmetrical wetting case, where the \perp orientation is realized. This is explained by the fact that the interfacial interactions can not compensate the increase of the free energy as a result of stretching or compression of chains to match the slit width. [Gei99] The windows of stability of the \perp orientation, however, gradually narrow with increasing the slit width and the surface interactions.

A special case worth noting is ultrathin BC films, *i.e.* with $d < L_0$. Theoretical predictions of thin morphology in this thickness region are rare and discrepant. We can mention two works, where the results of theoretical calculations were compared to experimentally observed morphologies. [Fas2000, Kra2002] The morphology of droplets of symmetric polystyrene-*block*-poly(*n*-lauryl methacrylate) (PS-*b*-PLMA) on Si substrate were studied at the droplet edge. [Fas2000] In agreement with the SCF calculations, the following sequence of morphologies was experimentally observed: $L//$ ($d \approx L_0$) \rightarrow hybrid $L//\perp$ ($d \approx 0.5 L_0$) \rightarrow $L\perp$ ($d \approx 0.3 L_0$) \rightarrow *dis* adsorption layer ($d \approx 15 \text{ \AA}$). Asymmetric polystyrene-*block*-polybutadiene-*block*-polystyrene (PS-*b*-PBd-*b*-PS) films on PBd covered substrate demonstrated the different sequence with agreement to calculations of H. P. Huinink *et al.* [Hui2000] within dynamic density functional theory: $C\perp$ ($d \approx L_0$) \rightarrow HPL ($d \approx 0.75L_0$) \rightarrow $C//$ ($d \approx 0.5L_0$) \rightarrow $C\perp$ ($d \approx 0.3L_0$) \rightarrow *dis* adsorption layer.

Ability to achieve a desired orientation of microdomains (typically $C\perp$ and $L\perp$ with respect to the film plane) is a crucial point for application of BCs in thin films. In practice, substrate-supported films with free surface typically avoid the \perp orientation due to formation of terraces. Indicative, in this respect, are the results obtained by H.-C. Kim and T. P. Russell [Kim2001], who studied morphological evolution of a polystyrene-*block*-poly(methyl methacrylate) (PS-*b*-PMMA) film of the C morphology having the thickness of $\sim L_0$ upon annealing. Terrace formation was found to be the slower process than microphase separation. Mismatch of the film thickness with the quantization relation resulted in the alignment of C microdomains normal to the film surface at the early stage of annealing. The cylinders re-oriented in-plane, when terraces of the height L_0 had developed. In contrast, the stable $L\perp$ morphology without formation of terraces was observed for one period thick PS-*b*-PMMA films. [Mor97]

Recently, it was demonstrated by T. P. Russell *et al.* [Kel96, Man97, Hua98b-c, Hua99] that PS-*b*-PMMA films of the *L* and *C* morphologies annealed on “neutral surfaces” adopt the \perp orientation, as theoretically predicted. Such surfaces were obtained by deposition of random copolymer of appropriate composition. Stability of *C* \perp morphology, however, was limited by the film thickness of $\sim L_0$.

There are many examples of \perp orientation of *C* and *L* microdomains, which is a result of preparation conditions. P. Mansky *et al.* [Man95] observed the *C* \perp morphology of polystyrene-*block*-polybutadiene (PS-*b*-PBd) films cast on water surface. The \perp orientation was explained by the pre-orientation of the chains parallel to the film interfaces due to equibiaxial flow propagation of dBC solution on the water surface prior to microphase separation. Surprisingly, following annealing of the films did not influence the orientation. The authors suggested that such films were metastable and re-orientation in the more stable // alignment did not occur because of substantial energy barrier between the orientations. G. Kim and M. Libera [Kim98] found dependence of orientation of *C* microdomains on evaporation rates of solvent from cast PS-*b*-PBd-*b*-PS *tri*BC films. The \perp orientation and satisfactory levels of ordering were observed at intermediate evaporation rates. Upon such conditions, PS cylinders were suggested to grow in the direction of the maximum gradient of solvent concentration and adopt the normal orientation. Dissimilarity in solvent mobilities in PS and PBd blocks assists the orientation, which provides continuous and direct transport pass to the surface during evaporation. Post-evaporation annealing of as-cast films, however, resulted in re-orientation of cylinders parallel to the film surface. Similar results are obtained for the *L* films [Sch92] as well as for *di*BC films of polystyrene-*block*-polyethyleneoxide (PS-*b*-PEO) [Lin2002] of *C* morphology.

In the last years, new approaches to control orientation and ordering of microdomains were reported. It was demonstrated [Mor96, Thu2000] that annealing of PS-*b*-PMMA films in external electric field of high strength (at least 30 kV/cm) leads to the orientation of *L* or *C* PMMA microdomains along the field lines, in either normal or in-plane direction depending on the applied electric field orientation. Remarkably, the desired \perp orientation was achieved for several micrometer thick films. The effect of external electric field on the BC film structure and on the ODT temperature was the subject of several publications.[Amu91, Amu94, Gur95] Chemically patterned substrates may also assist the formation of the *L* \perp morphology and provide long-range ordering of microdomains in thin *di*BC films. [Roc99, Yan2000]

Order in block copolymers

The high degree of a structural order is a crucial requirement for many applications of thin BC films. Depending on BC molar mass, incompatibility of block-forming polymers and preparation conditions, thin BC films self-assemble into morphologies with a liquid-like or crystalline order of microdomains. In the former case, the order persists in a distance not exceeding a few repetition periods of a microdomain structure, hence being short-range. In the latter case, BCs reveal regions with a long-range microdomain order. These regions (called *grains* or *domains*) have a random orientation with respect to each other. The mean grain size is one of the important characteristics of a BC order.

We consider two microdomain in-plane patterns important for practical applications. Hexagonal in-plane patterns are formed by $C\perp$ or S (BCC lattice plane (111) is coincident with the film plane) microdomains. In the hexagonal structure, each microdomain is surrounded by six closest neighbors. This six-fold symmetry is broken at the grain boundaries, where crystal axes change their directions. As a result, a string of microdomains surrounded by four, five, seven or even eight close neighbors appears. These defects of microdomain packing are called *dislocations*. Since the fraction of defects in BC directly relates to the grain size, it is usually used as a criterion of the structural order. While the grain size reflects the orientational order of a BC structure, the distribution of the microdomain spacing is the characteristics of its translational order. The BC structure which has only the short-range translational but quasi-long-range orientational order is called *a hexatic phase*. [Seg2003] In the hexatic phase, microdomains have on average six neighbors, *i.e.* each five-neighbored microdomain is always adjacent to another one having the seven close neighbors (so called *five–seven dislocations*). Therefore, the hexatic phase comprises defects formed at the grain boundaries as well as individual dislocations and dislocation clusters inside the grains. The microdomain shape and the microdomain size are two other parameters characterizing the quality of a BC structure. The narrow distribution (monodispersity) of the microdomain size is especially important when a BC film is used as a lithographic template. [Gua2002]

In-plane patterns formed by $C//$ or $L\perp$ microdomains also demonstrate variety of topological defects. The first type of defects is disclinations, which are recognized from either "bending" of the stripes or points, where stripes with three different orientations meet. The second type of defects is dislocations, which correspond to the insertion of an extra period in the stripe pattern. The ordering of the stripes in long-range patterns proceeds through migration and subsequent annihilation of complementary defects. [Har2000, Hah2001]

It was demonstrated that regular profiling and chemical patterning of substrates allow producing the macroscopic crystal-like ordering of microdomains in thin BC films. [Fas97, Yan2000, Seg2001] The required pattern periodicity is typically much larger than the spacing between adjacent microdomains and can be fabricated by methods of conventional photolithography and microprinting.

Applications of block copolymer thin films

The application of thin films of BCs as a lithographic mask and a template for synthesis of nanophase materials in many cases requires selective removal of one of the microdomain-forming blocks. UV radiation was demonstrated to degrade selectively PMMA block in PS-*b*-PMMA films.[Thu2000b,c] The pore size can be controlled by addition of different amounts of PMMA homopolymer. [Jeo2002] Selective removal of polyisoprene (PI) or PBd can be achieved by ozone etching *di*BCs, where the second block is PS.[Par97]

Production of nanostructures with BCs was recently reviewed in [Coh99, För2002, Ham2003, Liu2003]. In spite of large number of reported approaches, most of them can be ascribed to one of the next two groups: 1) application of BC as mask for lithographic transfer of their pattern into different substrates and 2) the use of BC microdomains as “nanoreactors” for synthesis of various nanophase materials.

The use of *di*BC films with a monolayer of ordered *C*// (PS-*b*-PBd) and *S* (PS-*b*-PI) microdomains for transfer of their patterns onto underlying silicon nitride (Si₃N₄) substrate were first demonstrated by M. Park *et al.*[Par97, Har98a] We shortly describe film processing on the example of transfer of hexagonal arranged *S* microdomains. First, PI spheres were either removed by ozonation or stained with OsO₄, respectively. Ozonation produced *S* voids in the PS matrix. Staining is necessary to make the PI spheres resistant to subsequent reactive ion etching (RIE). As a result of CF₄/O₂ RIE of such pre-treated films, caves (positive pattern transfer) or posts (negative pattern transfer) were formed onto underlying Si₃N₄. Similarly, staining with the following RIE was performed to transfer a fingerprint-like *L*// pattern. Later on, this method was extended to fabrication of regular arrays of gallium arsenide [Li2000] and gold nanodots [Par2001]. The application of BCs with a poly(ferrocenyldimethylsilane) (PFS) block allows to avoid ozonation or staining due to high resistance of PFS to the RIE.[Lam2000] In particular, PI-*b*-PFS was used in the multi-step lithographic process of fabrication of cobalt nanodots [Lam2000, Che2001]. Alternatively, PS-*b*-PMMA films with UV degradable PMMA block were employed to transfer *S* pattern onto silicon. [Asa2002, Nai2002] K. W. Guarini *et al.* prepared a well ordered *di*BC lithographic mask with \perp

oriented channels by deposition of PS-*b*-PMMA film on Si substrate modified with a random copolymer brush (neutral surface approach).[Gua2002a] The hexagonal pattern of the mask was first transfer by RIE into silicon oxide and then by chemical etching into silicon.[Gua2001, Bla2001] The obtained array of high aspect-ratio Si channels can find application in design of random access memory of high capacity. Fabrication of inverse structure, *i.e.* Si posts with potential applications in flat displays and microwave amplifiers was demonstrated in [Gua2002b].

We limit consideration of the second group of methods to synthesis of two-dimensional (2D) arrays of nanophase materials on solid substrates. Here, we can distinguish several approaches, where porous templates from BCs are used as a mask for growth of metal nanowires and nanodots. T. Thurn-Albrecht *et al.* [Thu2000b] applied strong electric field to micrometer thick PS-*b*-PMMA film to orient PMMA cylinders normal to gold covered substrate. Subsequently, the films were transformed into porous template by degradation of the PMMA cylinders by UV radiation. Finally, high aspect ratio cobalt nanowires were electrochemically grown on the gold substrate throughout the template channels. The obtained nanowires exhibit strong magnetic anisotropy and are potentially useful for high capacity magnetic storage media. This approach was also used for fabrication of nanoelectrode arrays. [Jeo2001] A simple method of fabrication of dense arrays of nanodots and nanochannels by evaporation of metals onto porous *di*BC templates was reported by T. P. Russell *et al.* [Shi2002] They prepared thin films of PS-*b*-PMMA with the volume PMMA fractions of 0.3 and 0.7. *di*BCs formed *C* microdomains of PMMA and PS, respectively. The desired perpendicular orientation of microdomains was achieved as described above by the neutral surface approach. In the course of UV degradation of PMMA the films were transformed into two kinds of templates, *i.e.* consisting of hexagonal arranged *C* channels in the PS matrix or hexagonal array of PS posts. The fabrication procedure was completed by evaporation of chromium or successively chromium and gold on the top of the templates, which were then removed by sonication in toluene. M. J. Misner *et al.* [Mis2003] demonstrated the possibility to fill template channels simply by dipping the template (again fabricated from PS-*b*-PMMA) into solution of cadmium selenide nanoparticles. However, this approach gave nonuniform filling the template channels.

Several papers were devoted to patterning of metal particles at surface of BC films. T. L. Morkved *et al.* found that evaporated gold selectively covers PS in PS-*b*-PMMA films and P2VP in PS-*b*-P2VP.[Mor94] Further, W. A. Lopes demonstrated [Lop2001, Lop2002] that evaporation of gold and silver on the top of asymmetric PS-*b*-PMMA films led to selective

decoration of PS *C//* microdomains, whereas indium, lead, tin and bismuth preferred PMMA matrix. Such a preference was explained by different surface mobilities of the metals in these blocks at elevated temperatures (typically 180° C). However, deposition of larger amounts of metal did not lead to coalescence of separate metal particles in continuous long nanowires. They rather formed metal islands ignoring the underlying *diBC* template. The single exception was silver, which demonstrated extremely high surface mobility on PMMA. It resulted in almost 100% selectivity in separation even for the deposited amounts of ~10 nm. Micrometer long continuous Ag nanowires were obtained with this approach. S. Horiuchi *et al.* [Hor2003] performed selective patterning of PS microdomains by exposure of PS-*b*-PMMA film to acetylacetonato-palladium vapors. Pd nanoparticles were formed by the following reduction of the complex. The selective patterning of PS-*b*-PMMA surfaces with passivated Au and Pd colloids was also reported by R. W. Zhener *et al.* [Zeh98, Zeh99] Subsequently, they used the surfaces patterned with metal nanoparticles as templates for the electroless growth of copper nanowires.

We found a variety of studies devoted to fabrication of metal and semiconductor nanostructures through complexation of metal salts with one of the blocks and their following reduction. [För98, Coh99, Ham2003, Liu2003] This approach called *loading* was realized in BC solutions as well as in bulk and film BC samples. Here, we should mention the micellar concept of patterning metals on surface developed by J. P. Spatz, M. Möller *et al.* [Spa96, Spa99] Gold salt (HAuCl₄) was added in micellar solutions of PS-*b*-PEO [Spa96] or PS-*b*-P2VP [Spa99] where PS blocks formed a micellar corona and PEO or P2VP blocks associated in micellar core. Tetrachloroaurate ions were bound as counterions to the polar core of the micelles. Such pre-loaded micelles were absorbed on different substrates as monolayers and the gold salt was reduced. As a result, quasi-hexagonal arrays of Au nanoparticles with the periodicity ranging from 20 to 200 nm were obtained.

1.2. Molecular assembly due to hydrogen bonding

Definitions, physical nature and classification of hydrogen bonds

Hydrogen bond (H-bond) is a strong intermolecular attractive interaction, which is formed between the following two atom groups. The first group includes a hydrogen atom H covalently bonded to an electronegative atom X (*hydrogen-bond donor*). The electron cloud of the hydrogen is delocalized towards the electronegative atom, hence inducing a positive partial charge at the hydrogen side. The second group involves an electronegative or neutral

atom Y with a lone pair of electrons (*hydrogen-bond acceptor*). Due to the small size of hydrogen atom as compared to other atoms, its partial charge reveals high charge density, which attracts a lone pair of another atom. In other words, 1s orbital of the hydrogen atom is partially overlaps with the lone pair orbital of the acceptor. Therefore, the H-bond X–H··Y (see Figure 1.5) is of not purely an electrostatic nature but also reveals features of a covalent bond. One of them is the directionality of H-bond. The *strong H-bonds* are linear, *i.e.* the X–H··Y angle is close to 180°. Such bonds are formed between very electronegative donor and acceptor atoms (e.g. in hydrofluoric acid). In the strong H-bond the donor atom comes into close vicinity to the acceptor atom with its lone pairs, what makes the bond essentially covalent in nature. The hydrogen atom is equidistant from both atoms (*symmetrical H-bond*). The potential energy function for hydrogen shows a single well between the donor and acceptor atoms. An H-bond of the *intermediate* strength is asymmetric, *i.e.* the hydrogen atom is shifted to the donor atom. Moreover, the distance between the donor and acceptors atoms is larger than in the strong H-bond. The potential energy function shows double well, in which its zero-point vibrational state is near the barrier. A *weak H-bond* has mostly electrostatic nature referring to conventional polar-polar interactions. [Fre2001] Besides the electronegativity of the donor and acceptors atoms, sufficient effect on the strength of H-bond has its environment and steric freedom of H-bond-forming groups. [Jef97] The strong H-bonds formed in the gas phase are significantly weakened in high-dielectric-constant media (*e.g.* polar organic solvents). The *intramolecular H-bonds* are typically weaker than intermolecular, which is a result of steric constraints for formation the linear H-bond.

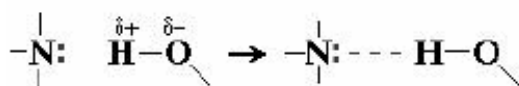


Figure 1.5. Formation of H-bond between phenolic group (oxygen is a hydrogen-bond donor) and amide (nitrogen is a hydrogen-bond acceptor).

In this study we deal with H-bonds formed by carboxylic, phenolic and pyridine functional groups. Figure 1.6 demonstrates possible ways of assembling of molecules with these groups. Hereafter, we apply the term *H-bond synthon* or simply *synthon* (usually used in the literature) to name the various combinations of assembling *via* hydrogen-bond-forming groups. Strong and directional O–H··O H-bond is formed in a dimer of phenol, the simplest synthon **I**. Two such H-bonds form centrosymmetric carboxylic dimer **II**. This synthon is

dominant (frequency of occurrence of 96% according to data of the Cambridge Structural Database) in the dry state, when competing donor and acceptor groups are absent. [Vis2002] Molecules with carboxylic groups also form chain sequences (*catemer*) **III**. If both hydroxyl and phenolic groups are present, the cyclic synthons **IV** and **V** may occur. [Vis2002] The pyridine group is known to be a strong H-bond acceptor. The hydroxyl-containing donors form with pyridine strong synthons **VI** and **VII** via O-H...N H-bond. [Vis2002, Vis2003] The synthon **VII** is stronger than **VI** due to contribution of weak C-H...O H-bond. Moreover, occurrence of this synthon is about ten times more frequent as compared to the synthons **I** and **II** [Vis2002]

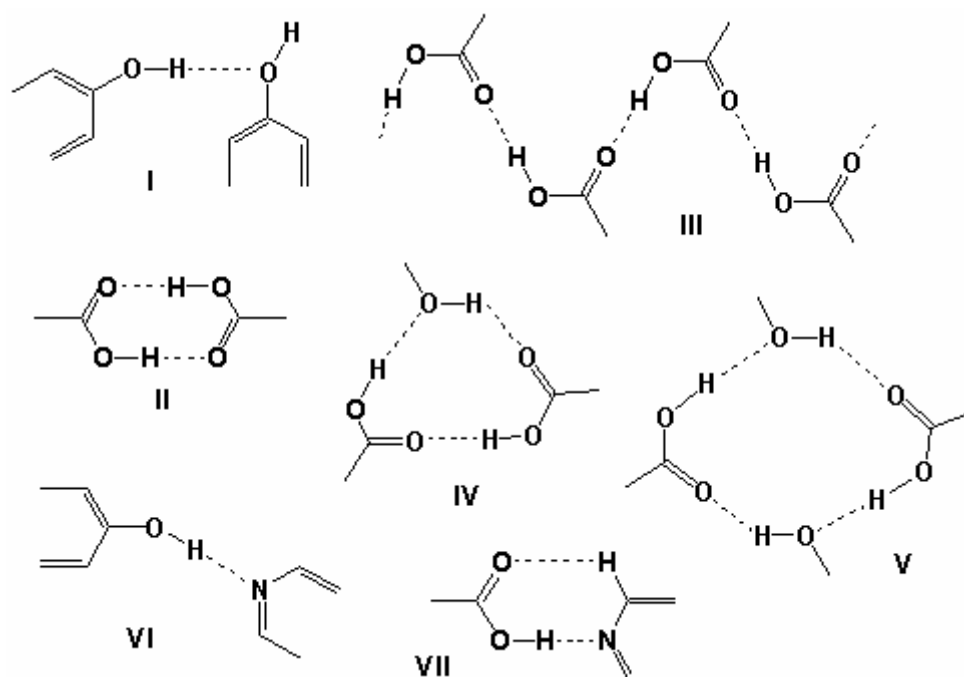


Figure 1.6. H-bond synthons with phenolic, carboxylic and pyridine groups.

Hydrogen bonds in polymers.

Blending of chemically dissimilar polymers allows producing new materials, which comprise the properties of their polymeric components. As it was previously discussed, incompatibility of chemically dissimilar polymers results in their phase separation. Unlike block copolymers, physical mixtures of two or more homopolymers demonstrate phase separation on macroscale. However, the single phase materials are frequently preferable. The common approach to miscible polymeric mixtures is introduction of groups capable to specific interactions, such as H-bonding or ionic interactions, in polymer chains of mixture components. Mixing is favored, when interpolymer interactions through H-bonds are stronger

than repulsive forces inducing macroscale self-assembly. Poly(2-vinylpyridine) (P2VP) and poly(4-vinylpyridine) (P4VP) are a wide used proton-accepting polymer, which forms miscible blends with a variety of proton-donating polymers such as poly(acrylic acid) (PAA) [Abe77, Jia2001], poly(ethylene-*co*-methacrylic acid) [Lee88] and poly(*p*-vinylphenol) [Lee86, Jia2001].

Groups capable to form H-bonds can be also used to provide polymers with various functionalities. For instance, coil polymer can be simply transformed into LC polymer by attachment of mesogenic side groups to a polymer backbone. Polyacrylate and P4VP demonstrate LC behavior after modification with stilbazoles [Kat92] and 3-pentadecyl phenol (PDP) [Ruo96], respectively.

This concept was also extended to block copolymers. [Kat92, Ruo99] O. Ikkala *et al.* [Ruo99] used strong H-bonding between 4-vinylpyridine monomer and 3-pentadecyl phenol (PDP) (see synthon **VI** in Figure 1.6) to modify the morphology of poly(styrene-*block*-4-vinylpyridine) (PS-*b*-P4VP). H-bonded assembly of PS-*b*-P4VP and PDP (PS-*b*-P4VP+PDP assembly) showed organization on two length scales (Figure 1.7). The larger structure was represented by microphase separated *di*BC domains (spherical, cylindrical or lamellar), while the smaller one (with periodicity of ~5 nm) was formed due to lamellar ordering of comb-like P4VP+PDP block. The modification of P4VP block with PDP shifted the symmetry of the larger length scale structure. In particular, PS-*b*-P4VP with the volume fraction of P4VP block of 0.12 changed the morphology from spherical to cylindrical or even lamellar depending on PDP amount added. [Ruo99] Oscillatory shear flow was applied to achieve macroscopic alignment of microdomains [Mäk2000, Mäk2001] Samples with aligned *C* microdomains were transformed into porous membranes by extraction of PDP from the P4VP+PDP microdomains with selective solvent. [Mäk2001]

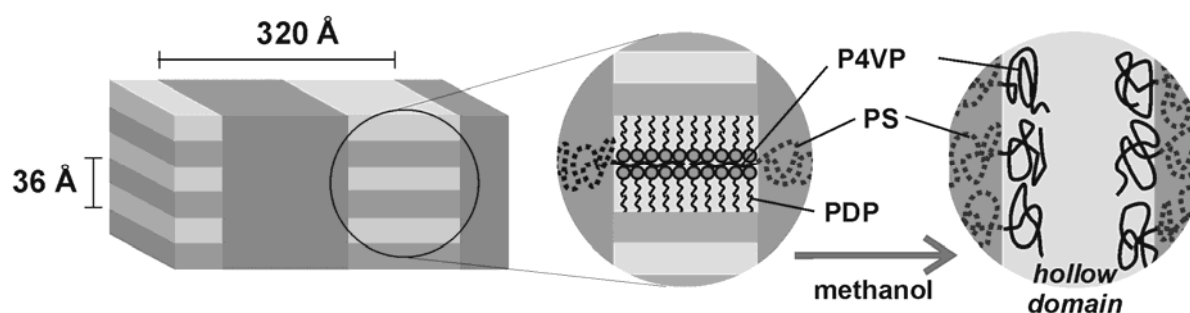


Figure 1.7. PS-*b*-P4VP+PDP assembly showing microphase separation into morphologies on two length scales. PDP can be extracted from microdomains by rinsing with selective solvent (methanol) giving rise to hollow channels.

1.3. Aim and outline of thesis.

In this work we develop and study polymeric materials which demonstrate two different kinds of assembly: microphase separation in BCs and molecular assembly due to H-bonding. Selective attachment of mesogenic molecules to one block via H-bonds was demonstrated to modify bulk properties of BCs. In principle, various functionalities can be introduced in a similar way. The aim of the thesis is to investigate phase behavior of hydrogen-bonded assemblies of BC and different low-molar-mass additives (hereafter BCA assemblies) in thin films. Confinement of a BCA assembly between two interfaces makes its phase behavior essentially complex.

In this work we study H-bonded assemblies of PS-*b*-P4VP with two different additives: 2-(4'-hydroxybenzeneazo)benzoic acid (HABA) and 3-n-pentadecylphenol (PDP). A molecule of HABA has a carboxylic group in the *ortho*-position and a phenolic group in the *para*-position. Both groups are capable to form strong H-bonds with nitrogen of the pyridine group as well as between themselves. The results of infrared spectroscopy study of H-bonding in solutions of PS-*b*-P4VP+HABA assembly are discussed in Chapter 3. The pattern of H-bonds is complex and depends on the solvent used. Unlike, a molecule of PDP has only one group (phenol) capable to form H-bonds. Moreover, its molecule is amphiphilic, *i.e.* consists of polar (phenol) and non-polar (alkyl tail) parts.

The morphology of PS-*b*-P4VP+HABA assembly is characterized in bulk and in “as deposited” thin films. The results of characterization of bulk samples of PS-*b*-P4VP and PS-*b*-P4VP+HABA assembly are presented in Chapter 3. We observe substantial modification of P4VP block with HABA, which changes the *di*BC symmetry. In Chapter 4 we study PS-*b*-P4VP+HABA assemblies with two different ratios between microdomain-forming blocks. Being deposited in thin films, they exhibit well defined *C* and *L* microdomain structures. The film morphologies are visualized after selective extraction of HABA from the P4VP+HABA microdomains, which transform to pores. Depending on solvent used for deposition, microdomains are oriented either perpendicular or parallel with respect to the film plane. The orientation is independent on film thickness (we studied film with the thickness of 20–100 nm) and insensitive to the chemical nature of substrate. Both *C* \perp and *C*// films reveal nanometer-thick disordered layers at the substrate and air interfaces. In Chapter 5 we demonstrate that the orientation of the “as deposited” assembly films does not change after their annealing in vapors of solvent used for deposition. Meanwhile, the solvent vapor annealing has significant effect on the microdomain ordering. We characterize the structural

order of assembly films swollen up to different swelling degrees. Optimized swelling conditions result in high-ordered microdomain structures. In Chapter 6, we demonstrate that orientation of microdomains can be switched from \perp to in-plane alignment and *vice versa* upon annealing in vapors of appropriate solvent. We discuss the observed microdomain orientation and the orientation switching in Chapters 5 and 6, respectively, using a model, which takes into account selectivity of solvent with respect to microdomain-forming blocks and phase transitions occurring during solvent vapor annealing.

In Chapter 7 we study the influence of nature of an additive on microdomain morphology in thin films on the example of PS-*b*-PVP+PDP assembly. We demonstrate that significant amount of amphiphile PDP phase segregates on the top of assembly films during the film formation. After following temperature annealing of the films, they exhibit complex thickness-dependent morphologies.

Some examples of application of thin films of BCA assembly are considered in Chapter 8. PS-*b*-PVP+HABA assembly films give a simple solution for the main problems of the use of BC thin films for templating of different materials. First, the desired \perp orientation of microdomains is readily achieved by choice of appropriate solvent for deposition and does not require preparation of “neutral” substrates [Kel96, Man97, Hua98b-c, Hua99] or application of strong external electric fields [Mor96, Thu2000]. Second, well-ordered microdomain structure is obtained within minutes by fast solvent vapor annealing of the films. Third, films are easily transformed into porous templates by convenient rinsing of the films in solvent selective for additive. The pore walls are formed by the reactive P4VP brush which can serve as active sites for chemical synthesis of nanoparticles in template pores. As it can be seen, our approach to nanoporous templates is very simple and fast. In chapter 8 we demonstrate the use of porous films of PS-*b*-PVP+PDP assembly as a mask for pattern transfer and of PS-*b*-PVP+HABA assembly as a template for fabrication of regular arrays of metal clusters by sputter and electrochemical deposition.

Chapter 2. Experimental

2.1. Sample preparation

Materials

diBCs of polystyrene-*block*-poly(4-vinylpyridine) (PS-*b*-P4VP) (Figure 2.1) and homopolymers of poly(4-vinylpyridine) (P4VP) and poly(1,2-butadiene) (PBd) were purchased from Polymer Source, Inc. The polymers were synthesized by anionic polymerization. The information on the molar masses (M_n) of the polymers and the *diBC* denotations used in the text below are given in Table 2.1. The *diBC* denotations are interpreted as follows: *e.g.* S34 means the PS block with length of about 34 kg/mol and V3 means the poly(4-vinylpyridine) block with length of about 3 kg \times mol $^{-1}$.

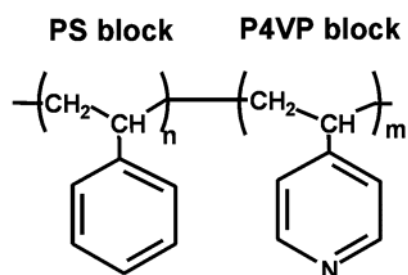


Figure 2.1. Polystyrene-*block*-poly(4-vinylpyridine)

Table 2.1. The parameters of the polymers used in the study.

Denotation in text	M_n , kg \times mol $^{-1}$	M_n/M_w	P4VP volume fraction
S36V4	39.2	1.06	0.094
S33V8	41.0	1.06	0.197
P4VP	3.0	1.50	1.0
PBd	50.0	1.06	-

Carboxyl-terminated random copolymers of styrol and 4-vinylpyridine (P(S-*r*-4VP)) containing from 9 to 33 % (with the step of 4–5%) of 4-vinylpyridine were synthesized by radical copolymerization ($M_n=9-11$ kg \times mol $^{-1}$, $M_w/M_n=1.86-2.23$). 3-Glycidoxypropyl trimethoxysilane (GPS) ABCR (Karlsruhe, Germany) was used as received.

Low-molar-mass additive, 2-(4'-hydroxybenzeneazo)benzoic acid (HABA, $\geq 99.5\%$ -pure) (Figure 2.2.a) was purchased from Fluka and used as is. 3-Pentadecyl phenol (PDP, $\geq 90\%$ -pure) (Figure 2.2.b) was purchased from Sigma-Aldrich. Before use, PDP was recrystallized five times with petroleum ether, filtered and dried at $40\text{ }^{\circ}\text{C}$ in vacuum for 2 days. The amount of residual admixtures in the purified PDP was less than 2% as was proved with ^1H NMR spectrometry.

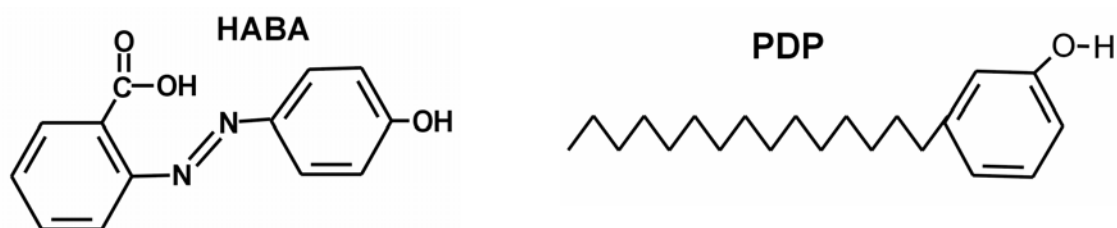


Figure 2.2. Low-molecular weight additives: a) 2-(4'-hydroxybenzeneazo)benzoic acid (HABA) and b) 3-Pentadecyl phenol (PDP).

Solvents – dichloromethane, chloroform, 1,4-dioxane, tetrahydrofuran (THF), toluene and methanol, – were purchased from Acros Organics. Prior to use, 1,4-dioxane was dried under sodium. Components of the Watts bath, nickel(II) sulfate hexahydrate ($\text{NiSO}_4 \cdot 6\text{H}_2\text{O}$, $\geq 99.99\%$), nickel(II) chloride hydrate ($\text{NiCl}_2 \cdot \text{H}_2\text{O}$, 99,95%) and boric acid (H_3BO_3 , 99.99%), were purchased from Aldrich. Chromium and gold targets ($\geq 99.98\%$) were purchased from MaTeck GmbH (Germany). Photoinitiator benzophenone ($\geq 99\%$ -pure) was purchased from Aldrich.

Highly polished silicon (Si) wafers {100} (Wacker-Chemitronics) and quartz slides were cleaned in an ultrasonic bath (dichloromethane) three times for 5 min. Then they were placed in either fresh prepared "piranha" bath (30 vol% H_2O_2 , 70 vol% of H_2SO_4 , *chemical hazard*) for 40 min or cleaning solution (25 vol% NH_4OH , 25 vol% H_2O_2 , *chemical hazard* and 40 vol% Millipore water ($18\text{ M}\Omega\text{ cm}^{-1}$)) for 1 h at $60\text{ }^{\circ}\text{C}$. [Ker90] Finally, the substrates were thoroughly rinsed with Millipore water and dried in argon flow.

Preparation of solutions of PS-*b*-P4VP+additive assembly

Preparation of solutions of PS-*b*-P4VP+additive assembly was similar irrespective of a low-molar-mass additive used. The assembly components were taken in the ratio of 1 mole additive to 1 mole 4-vinylpyridine monomer units of PS-*b*-P4VP. The mass and volume fractions of an additive and P4VP+additive in the assembly are listed in Tables 2.2 and 2.3.

The densities used for calculation of the volume fractions are PS $1.05 \text{ g}\times\text{cm}^{-3}$, P4VP $1.07 \text{ g}\times\text{cm}^{-3}$, P4VP+HABA $1.10 \text{ g}\times\text{cm}^{-3}$ (as determined by “buoyancy” method).

Table 2.2. Mass fractions calculated for equimolar assembly compositions.

Denotation in text	Mass fraction of P4VP+HABA in PS- <i>b</i> -P4VP +HABA assembly	Mass fraction of HABA in PS- <i>b</i> -P4VP +HABA assembly	Mass fraction of P4VP+PDP in PS- <i>b</i> -P4VP +PDP assembly	Mass fraction of PDP in PS- <i>b</i> -P4VP +PDP assembly
S36V4	0.255	0.178	0.288	0.214
S33V8	0.448	0.312	-	-

Table 2.3. Volume fractions calculated for equimolar assembly composition.

Denotation in text	Volume fraction of P4VP+HABA in PS- <i>b</i> -P4VP +HABA assembly	Defect of volume formed after extraction of HABA from PS- <i>b</i> -P4VP +HABA assembly
S36V4	0.243	0.168
S33V8	0.428	0.290

Chloroform, 1,4-dioxane, THF and toluene were used as solvents for preparation of assembly solutions. The HABA solubility is high in polar 1,4-dioxane, THF and methanol ($\geq 40 \text{ g}\times\text{l}^{-1}$ at RT), while it has limited solubility in nonpolar chloroform ($\approx 2.8 \text{ g}\times\text{l}^{-1}$ at RT) and toluene ($\approx 0.13 \text{ g}\times\text{l}^{-1}$ at RT). Amphiphile PDP is good soluble in all the solvents mentioned above. The solubility of PS-*b*-P4VP was found to be determined by the major PS block. PS is soluble in chloroform, 1,4-dioxane and THF and insoluble in methanol.[Bra99] Chloroform and methanol are known to be good solvents for P4VP. [Ruo99] To determine solubility of the P4VP block in other solvents, we used a homopolymer of P4VP ($3 \text{ kg}\times\text{mol}^{-1}$) as a reference. We found that 1,4-dioxane and THF do not dissolve but swell P4VP.

The assembly components were dissolved separately. Afterwards, the PS-*b*-P4VP solution was drop-by-drop added to the additive solution, while heating near the boiling point

of the solvent in ultrasonic bath. The heating and ultrasonification were necessary for better mixing and uniform assembly formation. The total concentration of chloroform solutions of PS-*b*-P4VP+HABA mixture was limited by the HABA solubility and was about 1% when S36V4 was used and 0.6% for S33V8. The mixture solutions were kept overnight to complete hydrogen bonding.

Small amount of precipitate caused by aggregation of PS-*b*-P4VP+HABA molecules is formed in chloroform solutions if stored for several days. The aggregate size is ranged from 92 to 480 nm, as determined by Dynamic Light Scattering (DLS) measurements. The precipitate is almost completely removed prior to deposition by filtering using a 0.1 μm filter. The DLS measurements also show formation of micelles with the mean size of ~ 51 nm ($\sigma = 14$ nm) in 1,4-dioxane solutions of S36V4+HABA (S33V8+HABA assembly is not characterized). The micellization is a result of the poor solubility of the P4VP block in 1,4-dioxane. Because of the small micelle size, they easily come through the used 0.1 μm filters.

Preparation of PS-*b*-P4VP+additive assembly films

Thin films of PS-*b*-P4VP+additive assembly were deposited by either dip- or spin-coating from filtered solutions. The thickness of the resulted films depends on the solution concentration as well as the withdrawal rate used for dip-coating and the revolution rate used for spin-coating. Withdrawal of substrate with the higher rate results in the thicker films. However, the maximal withdrawal rate is limited by the stability of deposited films. We observed ruptures in the films deposited with the withdrawal rate >2 $\text{mm}\times\text{s}^{-1}$. In our experiments, the withdrawal rates ranged from 0.1 to 1.0 $\text{mm}\times\text{s}^{-1}$. The obtained films were very uniform in thickness. In contrast, spin-coated films frequently exhibited appreciable wave-like variations in thickness. It is known that spin-coating on small-size substrates from viscous solutions leads to formation of standing wave pattern. [Car93] Films prepared by dip-coating are typically several times thinner as compared to spin-coated films for a given solution concentration. We used spin-coating when the desired thickness could not be obtained by dip-coating. In particular, S33V8+HABA assembly films were spin-coated from the 0.6% chloroform solution. The revolution rates of 500–3000 rpm were used.

The additives were extracted from P4VP+additive microdomains with selective solvent resulting in porous assembly films (templates). We rinsed the films four times in methanol for several minutes and dried in an argon flow.

Preparation of bulk samples of S36V4 and S36V4+HABA assembly

Preparation of bulk samples of S36V4 and S36V4+HABA for SAXS measurements was performed as follows. The S36V4+HABA assembly prepared in chloroform was precipitated in hexane and dried at 40° C for 2 days under vacuum. S36V4 powder and S36V4+HABA assembly precipitate were pressed in about 0.1–0.4 mm thick films within a wire ring support. Since the films are in the disordered state, their annealing is required. However, the conventional temperature annealing can not be applied for the S36V4+HABA assembly because of the high melting point of HABA (204–208° C). Furthermore, the heating of the samples to the temperature of 180° C leads to HABA decomposition. Instead, we performed the solvent vapor annealing of the films. For this, the films were placed into a closed glass vessel with a dish containing 1,4-dioxane for several hours. We stopped the swelling, when the film surface appeared glossy, preventing film disruption. The removed films were allowed to dry in air.

Solvent vapor and temperature annealing of PS-*b*-P4VP+additive assembly films

We applied solvent vapor annealing of PS-*b*-P4VP+HABA films to induce ordering or re-orientation of their microdomain structure. Film samples were placed into a closed glass vessel or an ellipsometric cell (for *in-situ* experiments) containing a dish with appropriate solvent. The films were swelled at room temperature (RT) until the desired swelling ratio r_{SW} defined as the ratio between the film thicknesses in the swollen and dry states was achieved. The desired ratio typically occurred for 5–40 min depending on r_{SW} . To achieve much longer swelling duration, samples were placed into a closed glass container with a pinhole in a cover prior to be introduced in a vapor atmosphere. The swelling ratio was monitored either ellipsometrically *in-situ* or evaluated by visual observation of film color.

Temperature annealing S36V4+PDP films was performed at 120 °C under vacuum. The annealing time ranged from 4 h to 7 days. Afterwards, the films were slowly cooled to RT.

Etching of S36V4+PDP assembly films

S36V4+PDP films were etched in oxygen plasma at different depths from the top to observe the inner film structure. Oxygen was chosen because the physical degradation of polymer chains is enhanced by chemical oxidation of the products. Unlike etching in plasma of nonreactive argon, the products of the reactive oxygen plasma etching are effectively removed, hence not accumulating on film surface. [Coll95]

Successive etching of S36V4+PDP assembly films was performed locally through a mask (Si wafer). Between repeated etchings the mask was shifted in a new position revealing an unexposed part of the film surface. As a result, regions on the film surface with the stepwise increase of the etch depth were obtained.

The oxygen plasma was produced by MicroSys 400 apparatus (customized by Roth&Bau, Germany) equipped with the 2.46 GHz electron cyclotron resonance plasma source. The effective microwave power of 250 mW, the pressure of 9.3×10^{-3} mbar, and the oxygen gas flow of 25 sccm resulted in the etch rate of $\sim 9 \text{ nm} \times \text{min}^{-1}$.

Sputter deposition of metals onto S36V4+HABA assembly templates

Sputtering of chromium and gold on the top of S36V4+HABA assembly templates was performed in a sputter coater supplied by tectra GmbH Physikalische Instrumente (Germany). The working chamber of the sputter coater with an installed sample was evacuated to pressure $\sim 1 \cdot 10^{-4}$ mbar and refilled with high-purity argon several times prior to sputtering. The sputtering was performed in argon plasma in the DC mode. The current of 0.04–0.12 A and the pressure of $(1.4\text{--}2) \cdot 10^{-3}$ mbar were chosen to give the stable plasma and the deposition rates of $0.2\text{--}0.5 \text{ nm} \times \text{min}^{-1}$ for chromium and $3\text{--}5 \text{ nm min}^{-1}$ for gold. The deposited amount (parameterized by the thickness of a layer) was monitored *in-situ* by a quartz microbalance (QMB) installed in a sputter chamber.

Nickel electrodeposition into S36V4+HABA assembly templates

Nickel was electrochemically deposited into channels of S36V4+HABA assembly templates prepared on different electrodes, *i.e.* Ni or Cr covered Si(100) wafers or doped Si(111) wafers.

The Ni electrodes have been fabricated via successive sputtering of Cr as an adhesive layer (5 nm thick) and Au layer (30-50 nm thick) on Si wafers. Ni films (30nm thick) were deposited on the top of Au electrodes by electrodeposition in galvanostatic regime using Watts bath as described elsewhere.[Thu2000b] Ni deposition reveals low roughness (rms roughness less than 2 nm on $1 \mu\text{m}^2$). Si(111) doped wafers were used without modification showing atomically smooth surface (less than 0.2 nm on $1 \mu\text{m}^2$ rms roughness) and high enough electroconductivity.

The mosaic Cr electrodes were fabricated as follows. First, 30 nm thick Cr layer was sputtered on Si wafers. Then, a thin film of PBD with addition of 5% of photoinitiator (benzophenone) was spin-coated onto the Cr covered wafer and illuminated with UV light (365

nm mercury lamp) through the 2000 mesh Ni TEM grid (Plano W. Plannet GmbH, Germany). The following washing of the film with toluene resulted in 60 nm thick cross-linked PBd squares arranged in 12 μm periodic square pattern. Micromapping ellipsometry showed that the shadowed location is Cr surface with no traces of PBd.

Ni was electrodeposited into the cylindrical channels of the template using an Autolab/PGSTAT30, an Ag/AgCl reference electrode and a platinum wire counter electrode. The Watts bath of the composition: 250 $\text{g}\times\text{l}^{-1}$ NiSO_4 , 100 $\text{g}\times\text{l}^{-1}$ NiCl_2 , 40 $\text{g}\times\text{l}^{-1}$ H_3BO_3 (pH = 4.0) was used. Methanol (30 vol%) was added to Watts bath to improve wetting of template channels by the electrolyte.

Ni electrodeposition through the template on the Ni and mosaic Cr electrodes was performed in the DC galvanostatic mode at the current density of 0.3 $\text{mA}\times\text{cm}^{-2}$ for 1000 s. Electrodeposition through a template on the Si(111) electrode was performed in the direct current (DC) galvanostatic mode (with the same parameters as above) and the pulsed galvanostatic mode as proposed by U. Gösele *et al.* [Nie2000] Native oxide layer of Si(111) interferes DC deposition. Higher cathodic potentials are required to allow tunneling through this oxide layer which can cause the side reaction of hydrogen evolution. Moreover, the slow diffusion-driven transport of Ni ions results in their exhaustion into the channels. The insulating effect of the native oxide is overcome by pulsed electrodeposition (PED). The current density (J_{pulse}) and the time (t_{pulse}) necessary to deposit Ni ions contained in the template channels during one deposition pulse can be calculated from the following simple expression, which is just the modified Faraday law:

$$J_{\text{pulse}}[\text{mA}\times\text{cm}^{-2}] \cdot t_{\text{pulse}} [\text{s}] = 2 \cdot 10^{-11} e [\text{C}] \cdot c [\text{M}] \cdot N_a \cdot K_{\text{eff}} \cdot f_{\text{pore}} \cdot d [\text{nm}]. \quad (2.1)$$

Here, e is the electron charge, N_a is the Avogadro number, c is the Ni ion concentration, K_{eff} is the current efficiency, f_{pore} is the template pore fraction and d is the template thickness. For the following parameters: $c = 2.2 \text{ M}$, $f_{\text{pore}} = 0.15$, $d = 60 \text{ nm}$, $K_{\text{eff}} = 1$ and $t_{\text{pulse}} = 0.02 \text{ s}$ we obtained $I_{\text{pulse}} \approx 2 \text{ mA}\times\text{cm}^{-2}$. We used a relative high current density to increase the number of nucleation sites in each channel. Subsequently, the second short pulse of the opposite current has to be applied to discharge the capacitance of the oxide layer. It leads, however, to partial dissolution of the Ni deposit. Finally, the template is conditioned at the zero current to allow recovering the Ni ion concentration into the channels. Afterwards, the steps are repeated. The optimized deposition parameters and the measured potentials are summarized in Table 2.4.

After Ni electrodeposition the templates were removed by washing in a nonselective solvent (chloroform).

Table 2.4. Parameters of impulse electrodeposition of Ni on Si(111). 50 scans performed.

Step	Current density $J_{\text{pulse}}, \text{mA} \times \text{cm}^{-2}$	Pulse duration $t_{\text{pulse}}, \text{s}$	Potential, V
1	-5.0	0.02	-5.0 ÷ -5.5
2	2.0	0.01	3.0 ÷ 3.5
3	0.0	0.97	-0.45 ÷ -0.55

Synthesis of brushes

Effect of a substrate surface energy on SMA morphology was studied with the use of Si wafers modified with one-component random P(S-*r*-4VP) and binary PS-P2VP brushes of different composition. Brushes were prepared by a "grafting to" approach which is described in detail elsewhere.[Min2002] Thickness of resulted brush layers ranges from 4 nm to 7 nm (ellipsometry).

2.2. Experimental methods

2.2.1. Ellipsometry

Ellipsometry is a non-destructive optical technique for characterization of surfaces, ultrathin films and multiple layers. It is widely used in industry (*e.g.*, microelectronics, optics) and surface science to control deposition, growth and etching of films, to study adsorption and swelling, optical anisotropy. It allows *in-situ* measurements. The comprehensive description of this technique was done by R. M. A. Azzam and N. M. Bashara. [Azz97]

Principle

Ellipsometry measures change in polarization of monochromatic light which is reflected upon a flat surface with single or multiple layers on it. Quantitatively, this change is defined as the ratio of the complex Fresnel reflection coefficients R for the p - and s -components of polarization:

$$\frac{R_p}{R_s} = \frac{|R_p|}{|R_s|} e^{i(\delta_p - \delta_s)} = \tan \psi e^{i\Delta}. \quad (2.2)$$

The ratio comprises the relative changes in amplitude and phase of the p - and s -components, which are expressed in ellipsometry by the angles ψ (in form $\tan \psi$) and Δ , respectively.

For a given multilayer system (with the m interfaces), the ellipsometric angles Δ and ψ are functions of all the optic parameters, the angle of incidence φ_i (measured from the substrate normal) and the wavelength λ

$$\tan \psi e^{i\Delta} = \rho(N_0, N_1, N_2, \dots, N_m, d_1, d_2, \dots, d_{m-1}, \varphi_i, \lambda). \quad (2.3)$$

The measurement of Δ and ψ at one wavelength and one angle of incidence allows to determine *only two* real parameters of the system under study, assuming that all the rest are known.[Azz97] Therefore, for multilayer polymer films, the common approach is ellipsometric measurements after each stage of film preparation. [Min02]

In practice, only one parameter has to be unknown, when measuring the transparent films thinner than 20 nm. Variation in a film thickness in this region causes mostly the phase shift between the s - and p -component polarizations (Δ), while their amplitudes are slightly affected (consequently, $\tan \psi$, too). Therefore, imprecision in a measurement of ψ has a considerable effect on a calculated refractive index and a thickness. For such films, we consider refractive index of a film as a known parameter and determined the film thickness. This requires only measurement of Δ .

Since Fresnel equations for the reflection coefficients are nonlinear and transcendent, hence analytical inversion of Δ and ψ into optic parameters of a multilayer film is impossible. Instead, computer ellipsometric programs (in our study, we used the programs supplied by the manufacturer of the ellipsometer) calculate the ratio of the reflection coefficients by varying one or two parameters of a layer model with following comparison of it with experimentally measured Δ and ψ . Reflection coefficients of a multiple layer are calculated by the layer matrix methods. [Lec87]

Ellipsometry of porous films

Porous assembly films show significant spatial variation of refractive index from 1 (pores) to 1.59 (PS-*b*-P4VP). However, this film heterogeneity is not resolvable for visible light, since the pore size (~ 10 nm) is much smaller than the wavelength used ($\lambda=632.8$ nm for He-Ne laser). The common approach to describe optical properties of such porous media is based on the effective medium theories. They replace a porous medium with the dielectric constant of the matrix ε and the pore fraction f_{pore} by an effective homogeneous medium with

the effective dielectric constant ϵ_{eff} . Dielectric media with the high pore fractions are well described by the symmetrical Bruggeman formula [Bru35]:

$$(1 - f_{pore}) \frac{(\epsilon - \epsilon_{eff})}{(\epsilon + 2\epsilon_{eff})} + f_{pore} \frac{(1 - \epsilon_{eff})}{(1 + 2\epsilon_{eff})} = 0, \quad (2.4)$$

In our ellipsometric calculations, a porous assembly film is treated as optically homogeneous. We use the Bruggeman formula to evaluate the pore fraction, assuming that the measured refractive index n is the root square of the effective dielectric constant ϵ_{eff} .

Instrumentation

Ellipsometric measurements were performed with a null ellipsometer (OPTREL GbR, Germany) and a rotating-analyzer (RA) ellipsometer SE400 (SENTECH Instruments GmbH, Germany). The instruments has the typical polarizer-compensator-surface-analyzer (PCSA) arrangement of polarizing components and use a He-Ne laser as a light source ($\lambda = 632.8$ nm). The RA ellipsometer is equipped with focusing optics collimating a laser beam in a 30 μm size spot on sample surface and a XY-stage for mapping measurements. The operation principles of the null and RA ellipsometers are described elsewhere.[Azz97] The measurements were performed at the angle of incidence of 70°.

Swelling films of a block copolymer assemble in solvent vapors were studied *in-situ* with a home made ellipsometric cell. The cell of trapezoidal shape is equipped with two quartz windows at 70° to arrange the normal direction of the probing beam.

2.2.2. Atomic force microscopy

Principle

Atomic Force Microscopy (AFM) is a scanning technique which analyzes forces acting on a cantilever-like probe with a nanometer sharp tip at the end brought into the close vicinity of a sample surface. In this work, AFM measurements were performed in *intermittent contact mode (IC-mode)* or *tapping mode*TM (Digital Instruments). In IC-mode, a probe cantilever is driven to vibrate with high amplitude (10–100 nm) near its resonant frequency by a piezoelectric element. Since the contact time between the tip and the sample is two orders shorter as compared to *contact mode*, the IC-mode is less damaging and typically used for imaging topography of soft materials. Additionally, it provides valuable information about local viscoelastic properties and probe-sample polar/nonpolar interactions (phase imaging). [Mag97] Because of the high amplitude of oscillation, the tip propagates through regions of

attractive (Van der Waals, electrostatic) and repulsive forces in a single oscillation cycle. The amplitude and the frequency of the cantilever decrease while approaching the sample surface. Upon scanning, these parameters (and, hence, the force gradient) are maintained constant at a set-point level by the feedback loop. It is achieved by adjusting the tip-sample distance. The feedback signal and the phase lag of the cantilever oscillation relative to the driving oscillation are displayed yielding height and phase images, respectively.

Structural order analysis of AFM images

The ordering degree of the $C\perp$ microdomains was deduced from the statistical analysis of AFM images of washed S36V4+HABA films. We used WSxM 3.0 (Nanotec Electronica S.L.) and Scion Image (Scion Corporation) programs to determine the positions of the pore centres and the pore dimensions from $1\times 1\ \mu\text{m}^2$ AFM images. These data were used to evaluate the fraction of defects (*i.e.* pores with the number of neighbours different from six) f_{defect} , the center-to-center distance distribution, the pore size distribution and the mean pore ellipticity e ($e^2 = 1 - b^2/a^2$, where a and b are lengths of the ellipse major and minor axes). We should note, that the typical resolution of the digitized images (512×512 pixels) is of about 1.95 nm that is only 4–5 times smaller than the pore size. To evaluate the errors arising from the digitalization, we generated a digital image with a perfect pattern of hexagonally packed round pores (Figure 2.3a). Such an ideal image has the feature size and the resolution comparable to $1\times 1\ \mu\text{m}^2$ AFM images. The results of calculations of the pore shape (“flooding” procedure) and the pore center positions and are shown in Figure 2.3b. Analysis of the image showed non-zero value for the mean pore ellipticity ($e = 0.44$), the non-zero center-to-center distance distribution ($\sigma \approx 7\%$ of the mean interpore distance d_{inter}) and the non-monodisperse pore size ($\sigma \approx 3\%$ of the mean pore size). We should also note additional error sources arising from size and shape of an AFM tip and piezo’s temperature drift during scan. The AFM tip geometry affects only the results of the pore size and shape analysis, while stretching or compressing of the AFM images in the direction of the slow scan broadens the center-to-center distance distribution. To minimize the effect of the temperature drift, we scanned the film surface several times before to capture an image. The examination of FFT plots obtained from AFM images allowed to detect the image distortion from the non-round shape of the first-order ring. The influence of the above mentioned errors becomes appreciable when analyzing the size and distance distributions of high-ordered BC patterns. Therefore, the comparison of the ordering degree of such films is infeasible. The only reliable parameter for characterization of the order is the defect fraction which is almost unaffected by

these errors. Packing defects were revealed by counting the number of the neighbors found around each pore (excluding the pores at the image boundaries) within a circle of a radius $r_{\text{search}} \approx (3/4)\sqrt{3}L_0$, where L_0 is the interpore distance. The radius value was optimized to give the minimum amount of the pores with the neighbor number different from six.

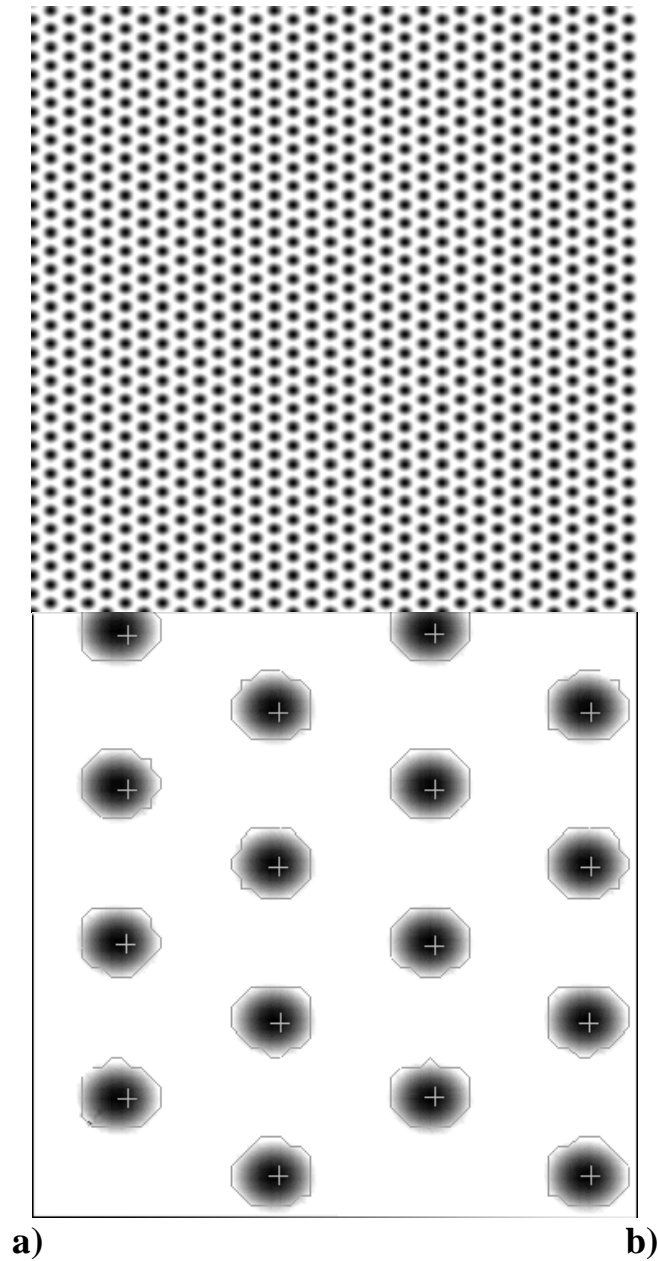


Figure 2.3. Digital image (resolution 512×512 pixels) showing a computer generated pattern of hexagonally ordered round holes (a) and the corresponding 10-fold zoom with the results of calculations of the positions of the hole centers (crosses) and the pore shape (solid line).

The degree of orientational order (the averaged size of ordered grains) was evaluated from profiles of the 2D autocorrelation function (AF) plots obtained from the $2 \times 2 \mu\text{m}^2$ AFM images. The profiles originated in the center of the plots (*i.e.* in the position of the zero-order correlation peak) and crossed any of six first-order correlation peaks. The distance from the profile origin to the point, where fault in the recurrence of the high-order correlation peaks occurs, determines the correlation length, which is related to the mean grain size. We should note that such statistical analysis is feasible only for structures, where the grain size is small as compared to the AFM image size.

Instrumentation

AFM measurements were performed with a Dimension 3100 (Digital Instruments, Inc., Santa Barbara) and CP (Park Scientific Instrument, Inc) atomic force microscopes in the tapping mode. The AFM probes of the spring constant of $1.5\text{--}3.7 \text{ N}\times\text{m}^{-1}$, the resonant frequency of 45–65 Hz and the tip radius of about 10–20 nm were used. Processing (flattening, filtering) and analysis of AFM images (power spectral density (PSD) and fast Fourier transform (FFT) plots) were performed with the WSxM software (Nanotec Electronica).

2.2.3. Wide and small angle X-ray scattering

Wide Angle X-ray Scattering (WAXS) and Small Angle X-ray Scattering (SAXS) are cognate techniques used to study structures on length scales comparable to atom/molecule and colloid size, respectively.[Bal89] In particular, WAXS is usually used to determine a structure of polymeric crystals. SAXS is a classical technique for characterization of bulk morphology of BCs. Patterns of scattered intensity comprise the structural information, such as size and shape of microdomains, the mean inter-domain distance, microdomain arrangement and ordering.

Principle

The interaction of X-rays radiation with matter results in both scattering and absorption of the X-rays. Scattering comes from collisions of photons with bound electrons and can be elastic (with no energy exchange, *i.e.* wavelength remains the same) or inelastic (or Compton, resulting in loss of the photon energy). Only elastic scattering gives rise to systematic interference between X-rays scattered by different volume elements of the structure (so called *coherent scattering*), while inelastic one produces continuous background.

Two-phase structures consisted of particles of colloid size in a matrix scatter in the small-angle region. The scattered intensity $I(\mathbf{q})$ (we consider only elastic scattering) is the product of the structure $S(\mathbf{q})$ and particle form $P(\mathbf{q})$ factors:

$$I(\mathbf{q}) = NS(\mathbf{q})P(\mathbf{q}), \quad (2.5)$$

where N is the number of particles per volume unit, $\mathbf{q} = \mathbf{k}_I - \mathbf{k}_O$ is the wavevector transfer or scattering vector (\mathbf{k}_I and \mathbf{k}_O are the wavevectors of the incident and the scattered X-ray waves, respectively; $|\mathbf{q}| = q = 4\pi\sin\Theta/\lambda$, where 2Θ is the angle between the incident and scattered X-rays).

The form factor $P(\mathbf{q})$ includes scattering arising from size and shape of particles. This scattering dominates in diluted systems, where $S(\mathbf{q}) \rightarrow 1$. $P(\mathbf{q})$ is often expressed as $\langle f(\mathbf{q})^2 \rangle$, where $f(\mathbf{q})$ is the Fourier transform of the electron density ρ of a particle and the average is performed over all the particles and their orientations. For anisotropic particles with a high ratio of length L_{particle} to radius R_{particle} (e.g. cylinders) oriented with an angle α between their axis and the normal to the incident beam, the form factor is given by [Fou51]

$$P(\mathbf{q}) = (\Delta\rho)^2 V^2 \int_0^{\pi/2} \left[\frac{2J_1(\mathbf{q}R_{\text{particle}} \sin \alpha)}{\mathbf{q}R_{\text{particle}} \sin \alpha} \frac{\sin((\mathbf{q}L_{\text{particle}} \cos \alpha)/2)}{(\mathbf{q}L_{\text{particle}} \cos \alpha)/2} \right]^2 \sin \alpha d\alpha, \quad (2.6)$$

where $\Delta\rho$ is the difference in electron densities of particles and a matrix, J_1 is the first order Bessel function of the 1st kind. $P(\mathbf{q})$ plot shows three characteristic regions of q -values.

- 1) The region of the low q -values ($|\mathbf{q}| < R_g$), which is well described by Guinier's approximation: $P(\mathbf{q}) = (\Delta\rho)^2 V^2 \exp(-q^2 R_g^2 / 3)$, where R_g is the averaged gyration radius of particles. For cylindrical particles, $R_g = (R_{\text{particle}})^2/2 + (L_{\text{particle}})^2/3$. In this region, a system is averaged with respect to particle position and rotation. For a system of disperse shaped and sized particles R_g reflects a second moment of the shape and size distributions about the mean.
- 2) The region, where scattering is governed by particle dimension ($2\pi/2R_{\text{particle}} < |\mathbf{q}| < 2\pi/L_{\text{particle}}$). The particles with cylindrical, disc-like and spherical shapes are considered as one-dimensional (1D), two-dimensional (2D) and three-dimensional (3D) objects, respectively. Scattering is proportional to $1/q^{dm}$, where dm is the dimension of the object. Thus, for cylindrical particles $I(\mathbf{q}) \sim L_{\text{particle}} \cdot R_{\text{particle}}^4 / q$.
- 3) The region of high q -values ($|\mathbf{q}| > 2\pi/2R$), which is described by Porod's law: $I(\mathbf{q}) \sim S_{\text{interface}}/q^4$, where $S_{\text{interface}}$ is the specific surface of the particle/matrix interface. This

relation is valid only for smooth and sharp interfaces. Scattering from diffuse and fractal interfaces show significant deviations from Porod's law.

In the non-dilute case, scattering due to the interparticle positional and orientational correlations becomes appreciable. It is taken in account by the structure factor $S(\mathbf{q})$, which depends on the position of the centers of gravity of two particles \mathbf{R}_i , \mathbf{R}_j and their relative orientations [Mai92]:

$$S(\mathbf{q}) = 1 + \frac{1}{NP(\mathbf{q})} \left\langle \sum_{i \neq j}^N \exp(i\mathbf{q}(\mathbf{R}_i - \mathbf{R}_j)) f_i(\mathbf{q}) f_j(\mathbf{q}) \right\rangle, \quad (2.7)$$

where N is the number of particles. Particle orientation is included in $f_i(\mathbf{q})$ and is averaged over all the particles. As can be easily seen, that the structure factor becomes independent from the form factor only for particles of isotropic shape ($f_i(\mathbf{q}) = f_j(\mathbf{q})$).

Diffraction of X-rays by an ideal crystal is described by the following structure factor [Als2001]:

$$S(\mathbf{q}) = \frac{\sin^2(N_1 \mathbf{a}\mathbf{q}/2)}{\sin^2(\mathbf{a}\mathbf{q}/2)} \cdot \frac{\sin^2(N_2 \mathbf{b}\mathbf{q}/2)}{\sin^2(\mathbf{b}\mathbf{q}/2)} \cdot \frac{\sin^2(N_3 \mathbf{c}\mathbf{q}/2)}{\sin^2(\mathbf{c}\mathbf{q}/2)}, \quad (2.8)$$

where \mathbf{a} , \mathbf{b} and \mathbf{c} are the unit cell vectors (*i.e.* the lattice parameters along x , y and z coordinates, respectively). The structure factor shows maxima at integer values of $\mathbf{a}\mathbf{q}$, $\mathbf{b}\mathbf{q}$ and $\mathbf{c}\mathbf{q}$. They correspond to the angles 2Θ of the scattered X-rays determined by Bragg's relation: $\lambda = 2d_{\text{abc}} \sin \Theta$, where d_{abc} is the spacing between the lattice planes. The maxima become sharper with increasing of N and reduce to δ -functions, when $N = \infty$.

The intensity distribution of an assembly of random oriented crystals (polycrystal) can be considered as the sum of the intensity distribution of the individual crystals, what results in dithering reflections over the circle with the radius $q = 2\pi/d_{\text{abc}}$.

Instrumentation

SAXS: homebuilt pinhole system mounted on a rotating anode generator ultraX-18 (RIGAKU-efg, Berlin) with confocal Max-Flux-Optics (Osmic, Troy, MI) equipped with an area detection system HiStar/GADDS (BRUKER-axs, Karlsruhe, Siemens Analytical, Madison / WI).

WAXS: 4-circle diffractometer P4 with an area detection system HiStar/GADDS.

2.2.4. X-ray reflectometry

X-ray reflectometry is a non-contact technique for characterization of interfaces, ultrathin films and multiple layers. It is routinely used for determination of interface distances with subnanometer resolution, layer density, average interface roughness and the roughness correlation function. Theory and instrumentation of X-ray reflectometry are well described in the monograph of M. Tolan. [Tol99]

Principle

A X-ray reflectometer records the angular dependence of the intensity of a monochromatic X-ray beam reflected upon a film. The refractive index (n) in the X-ray region is expressed as

$$n = 1 - \delta + i\beta, \text{ where} \quad (2.9)$$

$$\delta = \frac{\lambda^2}{2\pi} r_e \rho \quad \text{and} \quad \beta = \frac{\lambda^2}{4\pi} \mu$$

where $r_e = e^2 / (4\pi\epsilon_0 mc^2) = 2.814 \times 10^{-5}$ is the classical electron radius, ρ is the electron density and their product ($r_e \rho$) is the scattering length density; μ is the linear absorption coefficient. For most materials $\delta \sim 10^{-6} - 10^{-5}$, therefore, the real part of the refractive index is slightly smaller than unity. Therefore, the total external reflection from a vacuum/medium interface takes place at the angles of incidence α_i (measured from the substrate plane) below the critical angle $\alpha_c \approx \sqrt{2\delta}$. At $\alpha_i > \alpha_c$, the reflectivity (determined as the ratio of reflected to incident intensity) can be approximately given by [Ham94]

$$R(q_z) = \left| \frac{8\pi^2}{\lambda^2 q_z^2} \int \frac{d\rho(z)}{dz} \exp(-iq_z z) dz \right|^2. \quad (2.10)$$

where $q_z = k \cdot \sin \alpha_i$ is the wavevector transfer ($k = 2\pi/\lambda$). As it is seen from Equation (2.10), the intensity rapidly decays with the angle of incidence as q_z^{-4} . However, rough interfaces additionally damp intensity of the specular reflected X-rays because of scattering in off-specular directions. In a film, interference of the beams multiple reflected from the film interfaces results in modulations of the intensity with α_i or so called “fringes”. The fringe periodicity depends on the film thickness.

It is worth to note that X-ray reflectometry is sensitive only to the vertical electron density profile $\rho(z)$ of a sample. Since the electron densities of most polymers are very close,

polymer interfaces are typically indistinguishable for X-rays. This is known as the contrast problem. [Sta92]

Instrumentation

The reflectivity curves were recorded with the X-ray diffractometer XRD 3003 T/T (Seifert-FPM, Freiberg, Germany) operating at wavelength of 1.54 \AA^{-1} ($\text{CuK}\alpha$). X-ray reflectivity curves of multilayer films were analyzed with the *Internet* available program *Parratt32* or *The Reflectivity Tool*, which realizes Parratt's recursive method for rough interfaces. [Par54] The analysis requires an assumption concerning the film electron density profile. The profile parameters (typically distances between interfaces, electron density of layers, interface roughnesses) are optimized to obtain the best fit between theoretical and experimental reflectivity curves.

2.2.5. Grazing incidence small angle X-ray scattering

Grazing Incidence Small Angle X-ray Scattering (GISAXS) is a non-contact technique for characterization of lateral and normal density correlations, shape/morphology of nanoscopic structures on surface and in thin films.

Principle

GISAXS is a realization of Small-Angle X-ray Scattering (SAXS) in the Bragg (reflection) geometry (Figure 2.4). X-rays are incident on a sample under study at a grazing angle α_i , typically, just above the critical angles α_c of materials constituting a multilayer film. This angle of incidence insures the full penetration of the layer and the sufficiently large film volume involved in scattering. The intensity of scattered X-rays is recorded by two-dimensional (2D) detector and scattering direction is described by the exit angle α_f and the out-of-plane angle ψ .

Diffuse scattering of X-rays from a rough multilayer film was considered by V. Holy and T. Baumbach [Hol94] within the distorted-wave Born approximation. The scattered intensity is expressed as

$$I_{diff}(q) = \frac{Fk^2}{8\pi^2} \sum_{j,k=1}^N (n_j^2 - n_{j+1}^2) (n_k^2 - n_{k+1}^2)^* \times \sum_{m,n=0}^3 \tilde{G}_j^m \tilde{G}_k^{n*} \exp\left\{-\frac{1}{2}\left[(q_{zj}^m \sigma_j)^2 + (q_{zk}^{n*} \sigma_k)^2\right]\right\} S_{j,k}^{mn}(q) \quad (2.11)$$

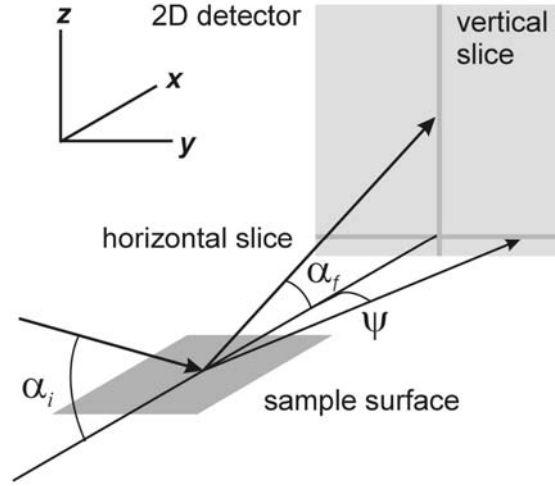


Figure 2.4. Schematic of the experimental set-up of GISAXS.

where the scattering function $S_{jk}^{mn}(q)$ is defined as

$$S_{j,k}^{mn}(q) = \frac{1}{q_{zj}^m q_{zk}^{n*}} \iint \left(\exp\{q_{zj}^m q_{zk}^{n*} C_{j,k}(X, Y)\} - 1 \right) \exp(-i(q_x X + q_y Y)) dX dY. \quad (2.12)$$

F is the illuminated area, n_j is the refractive index of j -th layer, σ_j is the rms roughness of j -th interface. $G_j^0 = T_{i,j} T_{f,j}$, $G_j^1 = T_{i,j} R_{f,j}$, $G_j^2 = R_{i,j} T_{f,j}$, $G_j^3 = R_{i,j} R_{f,j}$, where $T_{i,j}$, $T_{f,j}$ and $R_{i,j}$, $R_{f,j}$ are the amplitudes of the transmitted and reflected waves within j -th layer, respectively. The amplitudes can be calculated by the recursive methods (for instance, Parratt's method). $q_{zj}^0 = k_{zi,j} + k_{zf,j}$, $q_{zj}^1 = k_{zi,j} - k_{zf,j}$, $q_{zj}^2 = -q_{zj}^1$, $q_{zj}^3 = -q_{zj}^0$ are the z -component of the wavevector transfer, where $k_{zi,j}$ and $k_{zf,j}$ are the z -component of the incident and transmitted wave vectors in j -th layer, respectively. $C_{j,k}(X, Y)$ is the height-height correlation function. Its Fourier transform $\bar{C}(q_x, q_y) = \int C(X, Y) \exp(-i(q_x X + q_y Y)) dX dY$ gives the power spectral density (PSD) function. From Equation (2.12) several sequences can be derived.

- $I_{diff}(q)$ is proportional to the differences of the second power refractive indices Δn^2 of neighboring layers which compose a film. As in X-ray reflectometry, pronounce diffuse scattering can be achieved for layers having a sufficient electron density contrast.
- Diffuse scattering is enhanced at α_f equal to the critical angles of constituent layers, what results in characteristic diffuse scattering peaks (so called Yoneda peaks). [Yon63]
- In general, $I_{diff}(q)$ is not proportional to PSD function. The special case important for interpretation of scattering data is the horizontal cuts of the 2D scattered intensity (so-called *out-of-plane scans*). The Fresnel transmission coefficients act here as overall scaling factors. Therefore, for small $|q_z|^2 C(X, Y)$, the scattering intensity becomes proportional to

the PSD function of the in-plane fluctuations of the electron density in the film. [Tol99, Mü12000]

- X-rays scattered diffusely from layer interfaces with partially or fully correlated roughness interfere constructively giving rise to the resonant diffuse scattering (RDS). It appears in q_z -dependence as modulations of scattering intensity with period Δq_z determined by Bragg condition $2\pi/d_c$, d_c being the distance between the correlated interfaces. [Mü198]

Instrumentation

GISAXS measurements were performed at the beamlines BW4 and A2 of the Hamburg Synchrotron Radiation Laboratory (HASYLAB) in the Deutsches Elektronen-Synchrotron (DESY) center. White synchrotron radiation was monochromatized to 1.38 Å at BW4 and to 1.54 Å at A2. Two-circle goniometer with a z -transition table was used for the reflection mode. The sample-detector distances varied from 2.01 to 2.21 m. The 2D patterns of the scattered intensity were recorded with a detector consisting of 512×512 pixels array (BW4) and image plates (A2). At BW4, a beam stop was installed in the position of the reflected beam to block spill-over of intensive specular radiation in the scattering plane.

Analysis of GISAXS data from BC assemblies in thin films was performed by direct extraction of ensemble averaged in-plane periodicities from horizontal profiles of 2D scattered intensity distribution plots.

2.2.6. X-ray photoelectron spectroscopy and photoemission electron microscopy

X-ray Photoelectron Spectroscopy (XPS) is a widely used technique to investigate the chemical composition of surfaces. [Mui79] A related microscopic technique is X-ray Photoemission Electron Microscopy (XPEEM). [Stö2000]

Principle

XPS analyses kinetic energy distribution of electrons knocked out of inner-shell orbitals of atoms by a monochromatic beam of soft X-rays. The kinetic energy E_k of the photoemitted electrons is determined as follows:

$$E_k = hc/\lambda - E_b, \quad (2.13)$$

where hc/λ is the energy of the X-ray photons and E_b is the electron binding energy.

Soft X-rays ionize mostly electrons from the core orbitals (the K-shell), which binding energies are characteristic of a given atom and slightly influenced by chemical environment. In contrast to X-rays, free electrons pass small distances in a material without scattering. Thus, only the photoelectrons ionized close to the sample surface can be detected. The sampling depth of XPS is typically less than 10 nm. It can be varied by changing the angle between the surface normal and the electron-optic system.

XPEEM operates at the photon energies corresponding to the absorption edges of the characteristic core orbitals with the aim to contrast/visualize studied elements. This requires recording so-called X-rays Near Edge X-ray Absorption Fine Structure (NEXAFS) spectra of the elements. In contrast to XPS, NEXAFS measures the electron yield, while the X-ray photon energy (hc/λ) is scanned across the absorption edge of the core orbital of an element. The photoelectron emission intensity is strongly enhanced at absorption edges giving rise to characteristic peaks of elements.

Instrumentation

XPEEM and XPS measurements were performed at Berlin Synchrotron Source (BESSY II). The spectromicroscopic characterization was performed by a PEEM with integral sample stage (FOCUS IS-PEEM) (Omicron NanoTechnology GmbH, Switzerland). The setup was equipped with a CCD camera and an Imaging Energy Filter (IEF). The total intensity of the CCD camera was used to record the NEXAFS signal. In principle, pixel resolved local spectroscopic information can be obtained from the PEEM images (μ -NEXAFS). The IEF was used to record XPS spectra. The instrument is operated at the BESSY-U49/2 beam line which provides energies in the range of 100 ÷ 1200 eV with an energy resolution of approximately 0.1 eV.

2.2.7. Fourier transform infrared spectroscopy

Fourier Transform Infrared (FTIR) spectroscopy is a powerful technique for identifying functional groups and types of chemical bonds. Vibration energy levels of functional groups give rise to characteristic absorption spectra in the infrared region. In FTIR spectroscopy, there are three frequency regions, which are attributed to different vibration modes: near ($10000\text{--}4000\text{ cm}^{-1}$), middle ($4000\text{--}200\text{ cm}^{-1}$) and far ($200\text{--}10\text{ cm}^{-1}$). In this work, we used FTIR spectroscopy to study hydrogen bonds formed by P4VP and HABA. Formation

of the hydrogen bond A–H...B can be concluded from the following vibration modes: A–H stretch, A–H in-plane and out-of-plane bends, hydrogen-bond stretch and hydrogen bond bend. Corresponding absorption spectra are in the middle and far frequency ranges. Upon hydrogen bonding A–H bending frequency shifts to higher frequencies, while A–H stretching frequency shifts to lower frequencies with accompanying increase of intensity and band width. There is correlation between strength of a hydrogen bond and the infrared frequency shift it induces.

Infrared spectra were recorded with Bruker IFS 66v FTIR spectrometer in the transmission mode.

2.2.8. Ultraviolet–visible spectroscopy

Ultraviolet–visible (UV-vis) spectroscopy is a characterization technique, which probes the electronic transitions of the molecule, as they absorb UV and/or visible light. [Per92] HABA used in our work as a low-molar-mass additive is intense dye. Even very small HABA concentrations are visible with in UV-vis spectra. Thus, UV-vis spectroscopy is applicable for detection of HABA in thin films.

UV-vis spectra were recorded with the dual-beam UV-vis spectrophotometer (Cary 100, Scan Varian, Inc.).

Chapter 3. Formation of PS-*b*-P4VP+HABA assembly

*In the first section we present results of FTIR study of H-bonding between pyridine groups of P4VP and acidic groups of HABA in different solutions. A molecule of HABA has a carboxylic group in the ortho-position and a phenolic group in the para-position. Both groups are capable to form relatively strong H-bonds with nitrogen of the pyridine. Furthermore, HABA molecules show a strong tendency to self-association in dimers, trimers and other linear or cyclic sequences. If we also take into account interactions with solvent, we obtain a complex picture of H-bonding in a system from PS-*b*-P4VP and HABA in solutions and in solid state. In the second section, investigate how such macromolecular assembling modifies the bulk morphology of PS-*b*-P4VP.*

3.1. Spectroscopic study of P4VP+HABA assembly formation

Infrared spectra

FTIR spectroscopy provides us with the valuable information on groups involved in formation of H-bonds. Infrared spectra of HABA solutions in 1,4-dioxane and chloroform (Figure 3.1) give evidence of self-association of HABA molecules (*i.e.* formation of dimers, trimers, *etc.*). This is apparent from the O-H stretching absorption band of phenolic and carboxylic groups of HABA. Non-H-bonded groups absorb in the region of about 3630–3500 cm^{-1} . The absorption band shifts towards the lower wavenumbers ($\sim 3300\text{--}2500 \text{ cm}^{-1}$) and significantly broadens upon H-bonding. [Jef97] In experiment, we observe the broad absorption bands centered at 3249 cm^{-1} and 3197 cm^{-1} in chloroform and 1,4-dioxane, respectively. As follows from the relative shifts of the O-H-stretching bands, H-bonds in 1,4-dioxane are stronger than in chloroform. Figure 3.1 also shows the absorption bands centered at 1740 and 1731 cm^{-1} in chloroform and 1,4-dioxane solutions, respectively, which are attributed to stretching vibrations of carbonyl fragment of carboxylic group. The band positions indicate that carbonyl, unlike the hydroxyl fragment of carboxylic groups, is weakly H-bonded. [Lee88, Ces93] Again, the relative shifts of the bands show that the carbonyl fragments are notably less bound in chloroform solution. These results show the significant effect of solvent on H-bonding in systems with several functional groups.

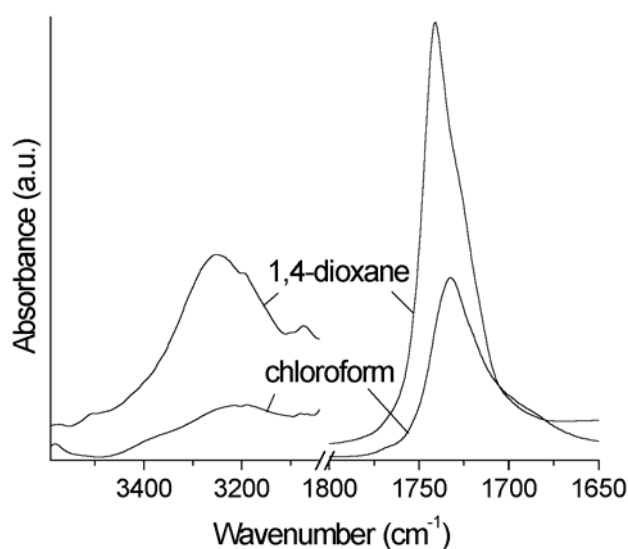


Figure 3.1. Infrared spectra of HABA in 1,4-dioxane and chloroform in the hydroxyl (left) and carbonyl (right) stretching regions.

The character of H-bonding is considerably changed, when HABA is added to solution of PS-*b*-P4VP. Infrared spectra of S36V4 and HABA in 1,4-dioxane and chloroform are shown in Figure 3.2a. Formation of H-bonds between HABA and pyridine groups of P4VP is apparent from the shifts (δ) of P4VP characteristic bands sensitive to the formation of H-bonds at 1415 cm⁻¹ ($\delta = +5$ cm⁻¹) and 993 cm⁻¹ ($\delta = +8$ cm⁻¹), as compared with S36V4 spectra. [Lee88] This result is very similar to reported in [Lee88, Ruo96] for H-bonds of P4VP with PDP and in a good agreement with general theory of influence of H-bonds on infrared spectra.

To explore the mechanism of the interaction between the P4VP block and HABA in different solvents, we recorded infrared spectra of the model system consisted of HABA and pyridine in 1,4-dioxane and chloroform solutions (Figure 3.2b, 2 and 3). As a reference, we used infrared spectra of HABA in 1,4-dioxane (Figure 3.2b, 1). We found very pronounced difference between the spectra in 1,4-dioxane and chloroform at the positions of the bands, which are attributed to C=O stretching vibrations of carbonyl fragments of carboxylic groups (centered at 1730–1740 cm⁻¹) and O–H bending vibrations of phenolic groups (1282 cm⁻¹) of HABA. New bands at 1720 cm⁻¹ in 1,4-dioxane and at 1275 cm⁻¹ in chloroform appear showing the formation of H-bonds with carbonyl and phenolic groups, respectively. Such a difference in H-bond formation in 1,4-dioxane and chloroform can be clarified from ¹H NMR spectra of HABA solutions. The spectra (not presented here) show that the peak of carboxylic group of HABA is significantly shifted ($\delta = -3$ ppm) as compared to the peak of reference 4-

(Phenylazo)benzoic acid located at 9.49 ppm. This shift is typical for the formation of intramolecular H-bond between the hydroxyl fragment of ortho-substituted carboxylic group and the nitrogen of the azo-benzene fragment of HABA. This allows us to assume, that carboxylic groups are not accessible for nitrogen of pyridine groups in chloroform solution. Therefore, the P4VP+HABA assembly is formed by only phenolic groups. In contrast, more polar 1,4-dioxane may diminish the intramolecular H-bonds. [Jef97] Then, carboxylic groups of HABA are accessible for formation of the P4VP+HABA assembly. Since carboxylic group is a stronger acid than phenolic group of HABA, it wins the competition for pyridine.

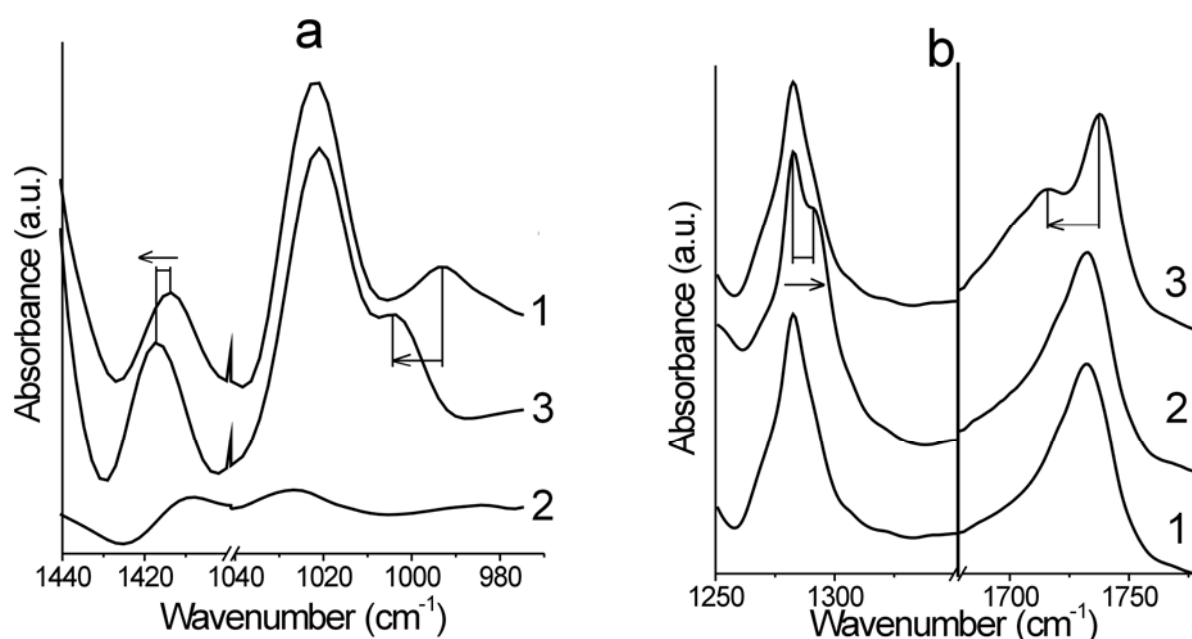


Figure 3.2. Infrared spectra of a) S36V4 (1), HABA (2) and S36V4+HABA (3), respectively, in the region of pyridine ring bands, b) a model system HABA+pyridine in 1,4-dioxane (3), chloroform (2) in the phenolic bending and carbonyl stretching regions compared with HABA without pyridine (1).

UV-vis study of S36V4+HABA assembly

HABA shows strong absorption in the UV/vis region due to $\pi \rightarrow \pi^*$ and $n \rightarrow \pi^*$ (n : nonbonding) transitions. The $\pi \rightarrow \pi^*$ band dominates the optical properties of HABA appearing in the UV/vis spectra (see Figure 3.3a) as the broad peak centered at 382.0 nm. The $n \rightarrow \pi^*$ transition results in the small shoulder in the visible region.

We found that the spectra of the S36V4+HABA films (deposited on quartz slides) reveal a blue shift of the main peak (367.4 nm), as compared to the spectra of HABA or S36V4+HABA in chloroform (Figure 3.3a-c). It indicates H-aggregation of HABA molecules

(head-to-head, according to the molecular exciton model). [McR58, Dan99] This specific structure may play an important role for the S36V4+HABA assembly morphology.

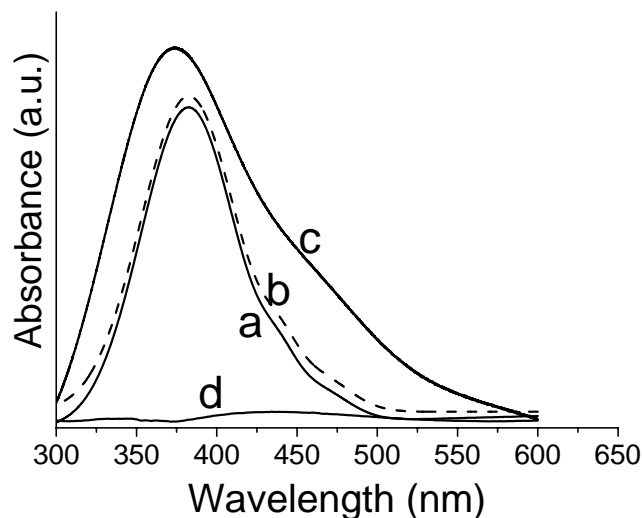


Figure 3.3. UV-vis spectra of a) HABA solution in chloroform ($1.8 \times 10^{-3} \text{ g} \times \text{l}^{-1}$), b) S36V4+HABA assembly solution in chloroform ($0.01 \text{ g} \times \text{l}^{-1}$), c) 110 nm thick S36V4+HABA assembly film, d) the same film after HABA extraction.

We use the characteristic absorption peak of HABA to examine S36V4+HABA assembly films after the rinsing with methanol. Methanol is a selective solvent for P4VP and HABA. It destroys H-bonds between the P4VP block and HABA and removes the latter from a film. Comparing the band intensities for the polymer film before (Fig. 3.3c) and after (Fig. 3.3d) the rinsing procedure one can see that HABA is completely washed out with methanol from the film.

3.2. SAXS/WAXS study of S36V4+HABA assembly

The effect of addition of HABA on the S36V4 morphology is studied in bulk with SAXS. Figure 3.4 shows the radially averaged SAXS profiles of S36V4 and S36V4+HABA assembly. The profiles clearly exhibit the first-peaks arising from the microdomain structures formed by microphase separated blocks. S36V4 shows the BCC *S* morphology (the P4VP volume fraction is 0.09) with the mean intersphere distance from the position of the first-order peak of $L_{\text{BCC}} = 2\pi\sqrt{2}/q_1 = 25.5 \text{ nm}$. We used the Gaussian distribution function to fit the SAXS profile of the S36V4+HABA assembly. The peak positions obtained from the fit relate as $1:\sqrt{3}:\sqrt{7}$, which indicates the formation of the hexagonal *C* phase. The mean intercylinder

distance determined from the first-order peak position is $L_{\text{hex}} = (4\pi/\sqrt{3})/q_1 = 26.5$ nm. The obtained results show that addition of HABA significantly increases the volume fraction of the minor P4VP block and changes the S36V4 symmetry from spherical to cylindrical.

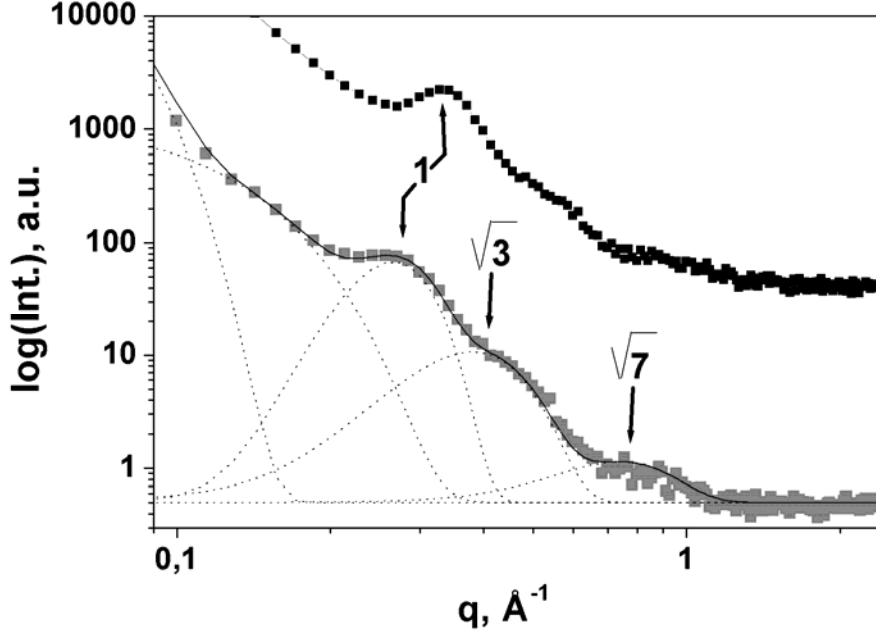


Figure 3.4. SAXS profiles of S36V4 (black) and S36V4+HABA assembly (gray). The curves are shifted for clarity. The arrows show the peak positions. The solid line shows the Gaussian fit of the profile.

Knowledge of the value of the mean intercylinder distance L_{hex} allows us to evaluate the degree of microphase separation (χN) of S36V4+HABA assembly. C morphology was approximated as a collection of cylindrical micelles with P4VP+HABA core and PS corona.[Liu94] The free energy of such a structure can be written as [Sem92]

$$F = Q \left[(1.645 - \ln f) \frac{x^2}{16} + 2 \frac{\alpha^{0.5}}{x} \right], \quad (3.1)$$

$$\alpha = \chi N_2 \quad \text{and} \quad x = 0.5 L_{\text{cyl}} f^{1/dim-1/2} / R_g$$

where Q is the number of copolymer chains in a micelle (for cylindrical micelles Q is independent on x), f is the *diBC* composition (we used the volume fraction of P4VP+HABA block $f = 0.243$, see Table 2.3), L_{cyl} is the diameter of *C* micelle (L_{cyl} is equal to the distance L_{hex} between hexagonally packed *C* microdomains), *dim* is the dimensionality (for cylindrical micelles $dim = 2$). The radius of gyration of *diBC* chain (assuming Gaussian statistics) is

$$R_g^2 = R_{g,1}^2 + R_{g,2}^2, \quad (3.2)$$

$$R_{g,i} = a_i \left(\frac{N_i}{6} \right)^{1/2}. \quad (3.3)$$

The statistical segment length a_i of i -block was evaluated from the following relation:

$$a_i = \left(\frac{6}{\pi} \frac{N_{w,i}}{\rho_i M_{w,i} N_A} \right)^{1/3}, \quad (3.4)$$

where $N_{w,i}$ is the weight-averaged molar mass of i -block (for S36V4+HABA assembly: PS block $N_{w,1} = 35500 \text{ g}\times\text{mol}^{-1}$, P4VP+HABA block $N_{w,2} = 3.3 \cdot N_{w,P4VP} = 12160 \text{ g}\times\text{mol}^{-1}$), ρ_i is the density of a phase formed by i -block ($\rho_1 = 1.05 \text{ g}\times\text{cm}^3$, $\rho_2 = 1.10 \text{ g}\times\text{cm}^3$), $M_{w,i}$ is the molecular weight of the monomeric unit of i -block ($M_{w,1} = 104.2 \text{ g}\times\text{mol}^{-1}$, $M_{w,2} = 105.1 + 242.2 = 347.3 \text{ g}\times\text{mol}^{-1}$). $N_i = N_{w,i}/M_{w,i}$ is the degree of polymerization of i -block ($N_1 = 341$, $N_2 = 35$). The equilibrium diameter of C micelle L_{cyl} for a given χ can be obtained by minimization of the function (3.1) for the free energy with respect to x . Our calculations show that $\chi = 0.168$ corresponds to $L_{\text{cyl}} = 26.5 \text{ nm}$, which coincides with the value of intercylinder distance L_{hex} measured with SAXS. The corresponding $\chi N = 63$ indicates that S36V4+HABA assembly is in the strong segregation regime. In this regime the $diBC$ chains are significantly stretched, $L_{\text{hex}} = 4.67R_g$.

We also performed WAXS measurements of S36V4+HABA assembly films to explore the internal structure of the P4VP+HABA microdomains. However, we found no difference in the scattering profiles of S36V4 and S36V4+HABA assembly in the wide-angle range. Therefore, we can conclude that P4VP+HABA block itself does not organize into an ordered structure, as it was found for PS-*b*-P4VP+PDP assembly. [Ruo98, Ruo99, Mäk2001]

Chapter 4. PS-*b*-P4VP+HABA assembly in thin films

*In this chapter we present the results on characterization of PS-*b*-PVP+HABA assemblies of the cylindrical and lamellar symmetry in thin films. The films with the thickness ranging from 20 to 100 nm were deposited by dip- or spin-coating on substrates of different chemical compositions. They show no signs of HABA phase separation, such as crystals or stains. Depending on solvent used the PS-*b*-P4VP+HABA films demonstrate ordering microdomains in either perpendicular or parallel orientation without an influence of additional external stimuli. The orientation is insensitive to the chemical nature of substrate. We show that HABA can be effectively extracted from the films resulting in regular arrays of nanoscale channels or grooves.*

4.1. S36V4+HABA films deposited from in 1,4-dioxane

Characterization of morphology

We used AFM to visualize the surface morphology of the S36V4+HABA films deposited from 1,4-dioxane solution. The films are very smooth with rms roughness of about 0.15 nm for $1 \times 1 \mu\text{m}^2$ lateral scale. We observed no sign of a microdomain structure from the microphase separated blocks in topography and phase images, which can be explained by the slight dissimilarity in mechanical properties of PS and P4VP+HABA. However, the film appearance is changed after rinsing in methanol, which destroys H-bonds between P4VP and HABA and extracts HABA from the film. AFM images (Figure 4.1) demonstrate hexagonal ordered caves of about 8 nm in diameter, independently on the film thickness (within the above mentioned range) and the chemical nature of substrate. We used various materials of different polarity as substrate such as: Si wafers, ITO and quartz glass, PS and P2VP brushes, cross-linked PBd, gold, chromium, nickel. We found that the hexagonal pattern and periodicity are insensitive to the chemical nature of the substrates. The mean distance between the neighbor caves is 22–23 nm (PSD plot), which is smaller than the periodicity found with SAXS in the bulk. The caves obviously appear as a result of extraction of HABA molecules from the P4VP+HABA microdomains. It is worth noting that the microphase separation into well resolved structure occurs within seconds, while solvent evaporates from a freshly deposited film. We attribute the observed morphology to perpendicular oriented cylinders

(C \perp) of the minor block, *i.e.* HABA, which are transformed into the channels by the rinsing procedure.

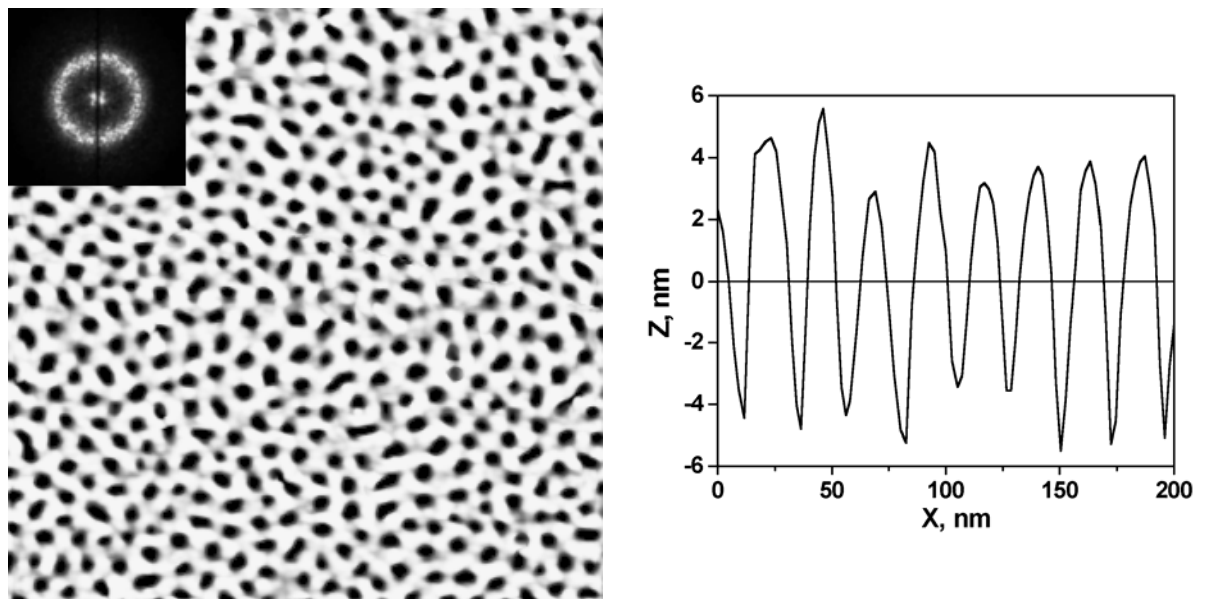


Figure 4.1. AFM image and corresponding cross-section of 40 nm thick S36V4+HABA film dip-coated from 1,4-dioxane solution and rinsed with methanol, lateral scale 500 \times 500 nm². The image was flattened.

AFM visualizes a surface morphology only locally. To obtain the statistically averaged information over a large film surface, we performed GISAXS measurements of the films. The vertical ($q_y = 0$) and horizontal ($\Phi = 1.54^\circ$) profiles of the 2D intensity distribution plot of the 33 nm thick film after rinsing with methanol are shown in Figure 4.2. Two Yoneda peaks attributed to the Si substrate (1) and the assemble film (2) are clearly seen in the vertical profile. However, the horizontal profile reveals no an out-of-plane peak indicative for the in-plane structure observed with AFM. This is explained by the lack of the contrast between the microdomain-forming blocks for X-rays. We should also note the rather low scattering from the unwashed film which is because of the low interface roughness. The scattering intensity is considerably increased after rinsing the film in methanol. The extraction of HABA from the microdomains introduces the contrast necessary to visualize the film morphology, as evident from the appearance of two pronounced peaks in the horizontal profile. The out-of-plane peaks relate in positions as $1:\sqrt{3}$, what is consistent with the hexagonal in-plane arrangement of the caves. The position of the first-order peak corresponds to the mean interpore distance. The obtained value, 23 nm, is in good agreement with the AFM data. The standard deviation

(σ) of the peak position is 15.5% (obtained from the Gaussian fit), which indicates on a relatively narrow distribution of the interpore distances.

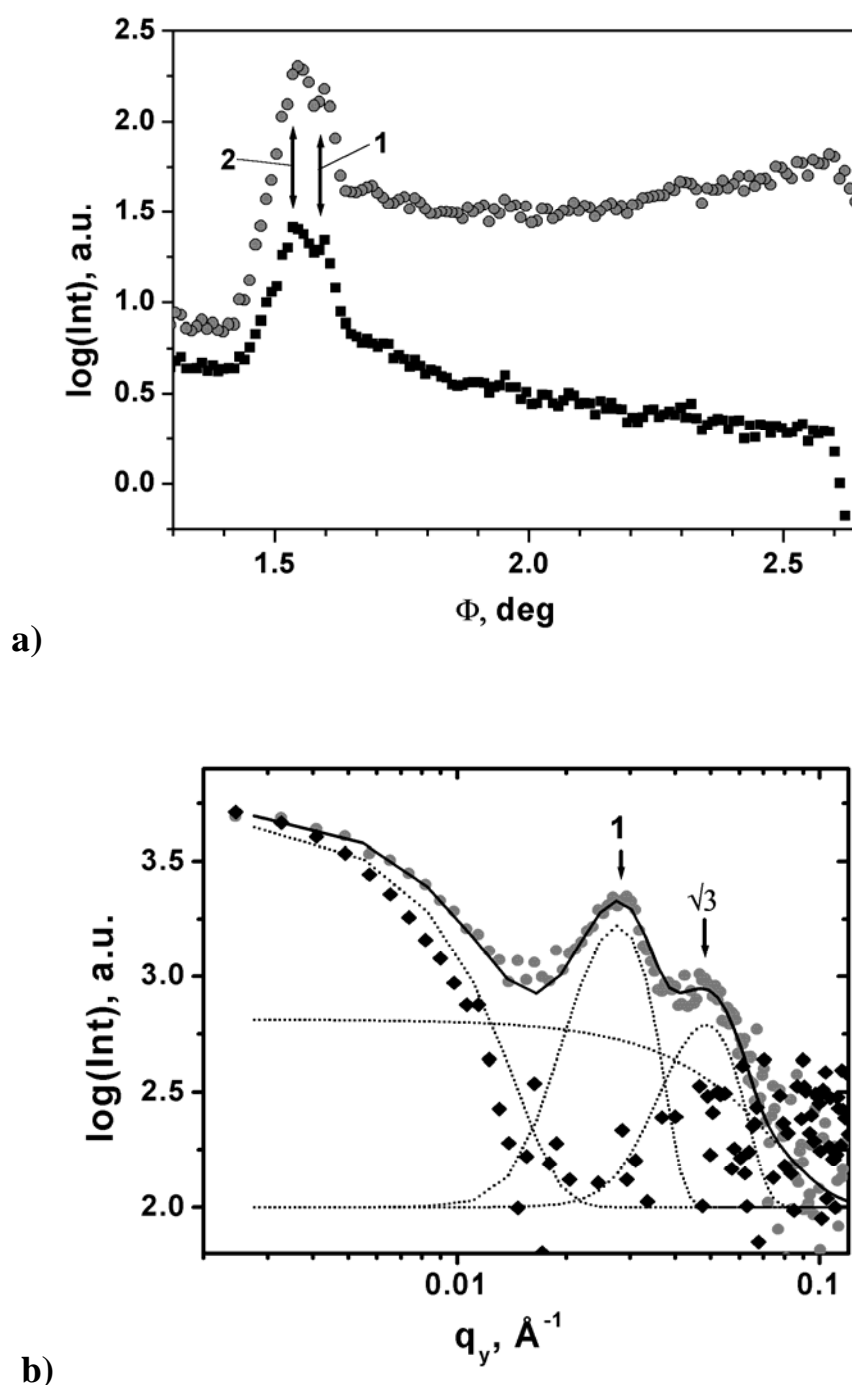


Figure 4.2. Vertical (a) and horizontal (b) profiles of 2D scattered intensity distribution plot of 33 nm thick S36V4+HABA film as deposited from 1,4-dioxane solution (black) and after rinsing with methanol (gray). The vertical profile curves are shifted for clarity. The solid line is the Gaussian fit of the horizontal profile. The arrows show the peak positions. The measurements were performed at the beamline BW4. The angle of incidence $a_i = 1.395^\circ$.

Characterization of the film porosity

The detailed examination of the vertical profile exhibited in Figure 4.2 shows that the position of the Yoneda peak 2 is slightly shifted towards the lower angles after the rinsing procedure. This is obviously a result of decreasing of the mean electron density of the film due to the pore formation. Unfortunately, the poor vertical resolution of the GISAXS measurements in the given geometry does not allow locating the exact position of this peak. The quantitative information on the porosity of the washed film can be obtained from the ellipsometric measurements. The S36V4+HABA films were measured twice: as deposited and after the rinsing procedure. We applied a simple two-layer model ($\text{SiO}_2/di\text{BC}+\text{HABA}$) to determine the thickness (d) and the refractive index (n) of films from the measured ellipsometric angles. The S36V4+HABA films show $n=1.610\pm 0.005$. This is essentially higher than the refractive index of PS-*b*-P4VP (1.59). The difference arises from the high refractive index of HABA and gives evidence for the appreciable HABA content in the films. We observed the decrease of both n and d after rinsing the films with methanol. The decrease of the refractive index gives evidence of formation of pores in assembly films, while the drop in the film thickness in turn shows that some amount of HABA is located at the interfaces. We found that the decrease of the thickness was proportional to the film thickness. Such behavior can be explained assuming that some fraction of HABA molecules is unbound with P4VP block. The pore fraction is independent on the film thickness. We observed only small variation of the refractive index of the rinsed films on the range of 1.51–1.53. The corresponding pore fractions (f_{pore}) evaluated with Bruggeman's equation (0.099–0.132) are somewhat smaller than the value (0.168) calculated using assumption that all HABA is located into the pores.

We used X-ray reflectometry as an independent method for the verification of the results of the ellipsometric measurements. Unlike GISAXS, the X-ray reflectometry is sensitive to the vertical electron density distribution. The X-ray reflectivity curve of the 35 nm thick film after the rinsing procedure is shown in Figure 4.3. We obtained the reasonable fit of the curve by assuming a single layer with the reduced electron density of $8.39\cdot 10^{-6} \text{ \AA}^{-2}$. This value is appreciably less than the electron density of PS-*b*-P4VP ($9.5\cdot 10^{-6} \text{ \AA}^{-2}$; both blocks have the close electron densities). Therefore, X-ray reflectometry gives evidence for the formation of the empty channels, which cross the film from the top to the bottom. The relative decrease of the mean electron density of the porous layer is about 12%. Assuming the direct relation with the film porosity, we obtain well agreement with the results of the ellipsometric measurements.

Characterization of the chemical composition of the film interfaces

We found that the higher-quality fit of the reflectivity curve in Figure 4.3 requires inserting an additional ~ 2 nm thick layer at the substrate interface, which electron density is coincident with PS-*b*-P4VP. This is consistent with the results reported for PS-*b*-P2VP by M. Möller *et al.* [Spa97] and M. H. Rafailovich *et al.* [Liu94]. They observed strong adsorption of the P2VP block to polar surfaces such as silicon and mica, which resulted in formation of a bilayer P2VP-PS brush at the substrate interface. This allows us to assume that the $C\perp$ channels terminate with an ultrathin P4VP layer on a Si substrate.

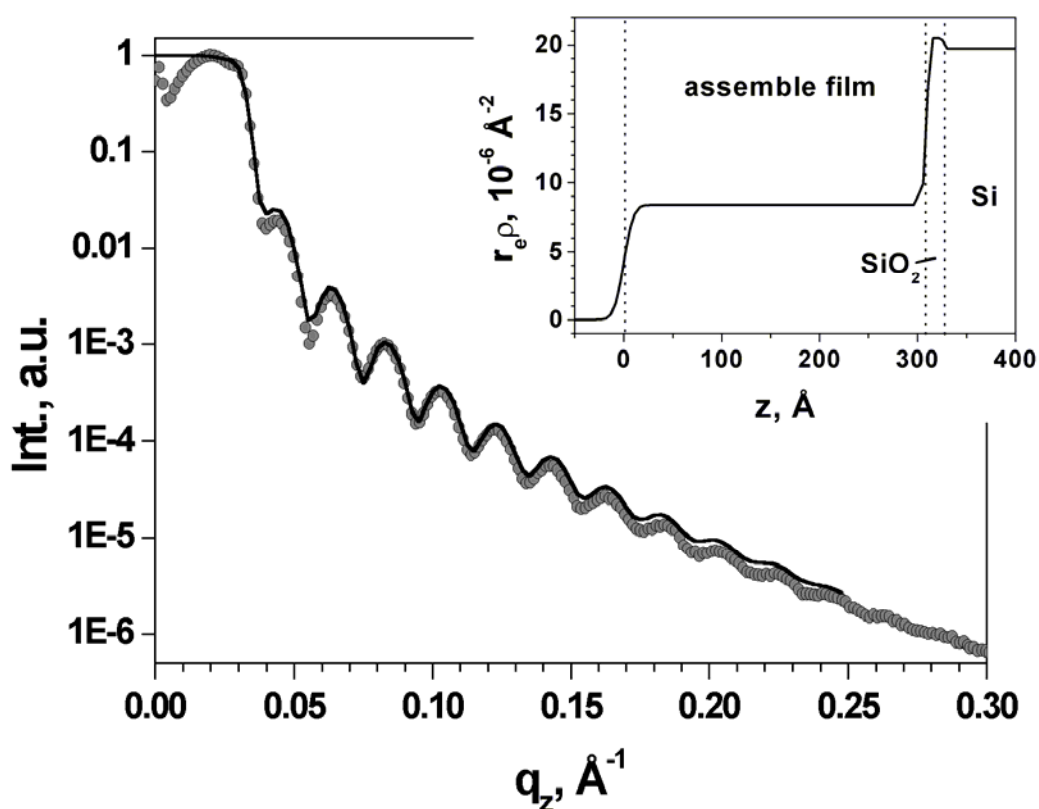


Figure 4.3. X-ray reflectivity curve with fit (solid line) and corresponding depth profile of the electron density (in inset) of 35 nm thick S36V4+HABA film dip-coated from 1,4-dioxane solution and rinsed with methanol.

We also performed XPS measurements to analyze the near-surface chemical composition of the S36V4+HABA films. The representative survey XPS spectrum is shown in Figure 4.4a, where we can distinguish the peaks of carbon, nitrogen, oxygen and silicon. The C 1s and N 1s peaks originate from the S36V4+HABA film only. Meanwhile, both HABA component of the film and native oxide of Si substrate contribute to the O 1s peak.

Therefore, we used only the former both peaks for the quantitative analysis of the XPS

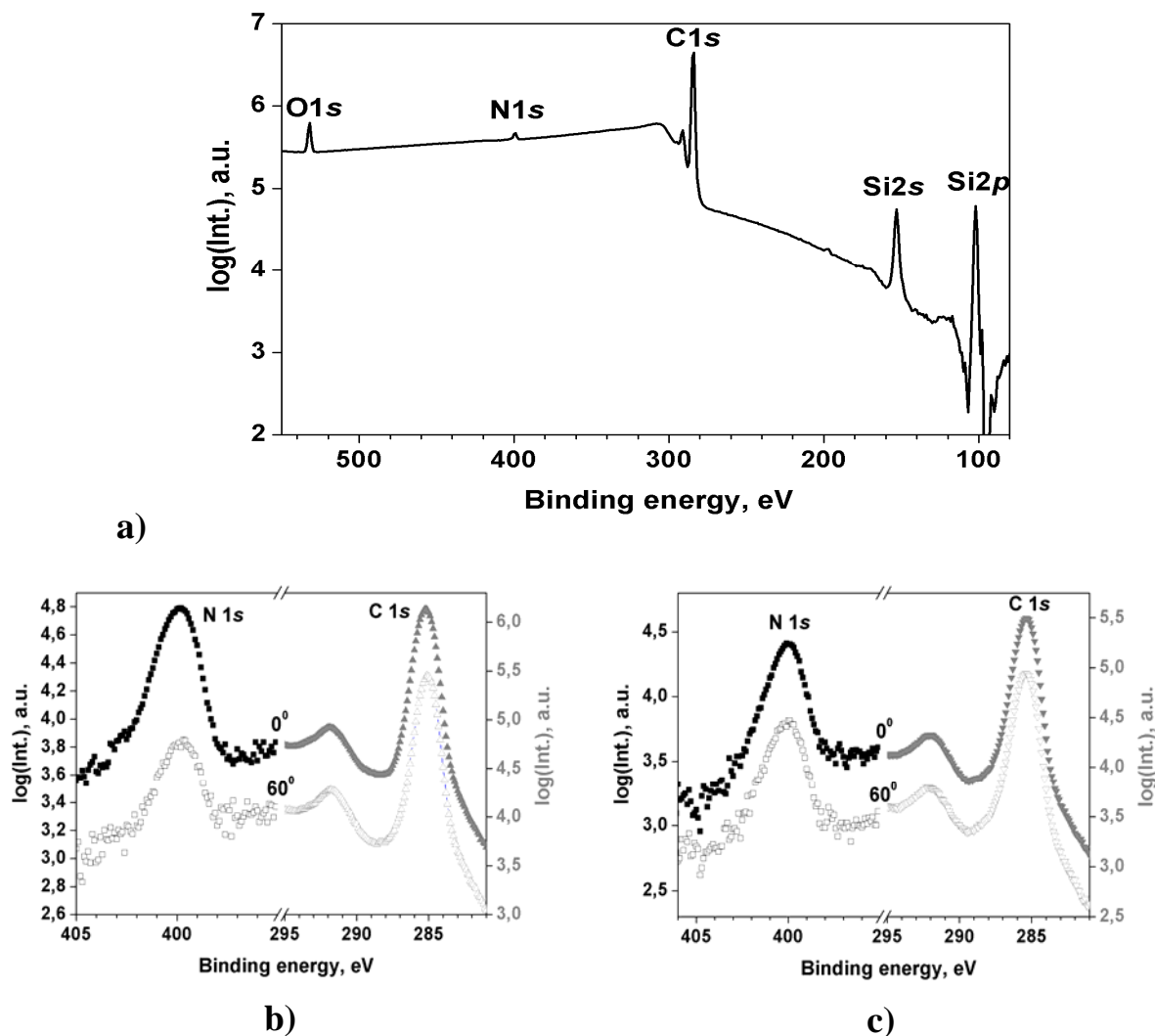


Figure 4.4. XPS spectra of S36V4+HABA film as dip-coated from 1,4-dioxane solution (a, b) and after rinsing with methanol (c): a) survey spectrum at the detector angle of 0° ; b) and c) N 1s and C 1s spectra at the detector angles of 0° and at 60° .

spectra. We performed the subtraction of the background and calculated the areas of N 1s and C 1s peaks. The obtained values were corrected for the relative sensitivity factors of the elements. The chemical structure of components of S36V4+HABA assembly predetermines the following nitrogen/carbon ratios $r_{\text{N/C}}$ in the individual polymer blocks, HABA and their compositions:

$$r_{\text{N/C, PS}} = 0;$$

$$r_{\text{N/C, P4VP}} = 1(\text{N1s})/7(\text{C1s}) = 0.143;$$

$$r_{N/C, S36V4} = \frac{1(N1s)_{P4VP}}{7(C1s)_{P4VP} + \mu_{PS/P4VP} 8(C1s)_{PS}} = 0.0118,$$

where $\mu_{PS/P4VP} = 9.74$ is the molar ratio of PS and P4VP in the block copolymer;

$$r_{N/C, S36V4+HABA} = \frac{2(N1s)_{HABA} + 1(N1s)_{PVP}}{7(C1s)_{P4VP} + 13(C1s)_{HABA} + \mu_{PS/P4VP} 8(C1s)_{PS}} = 0.0306$$

taking into account the equimolar composition of P4VP and HABA in the assembly. The experimentally determined value $r_{N/C, S36V4+HABA}$ (0.0150) is about twice lower than the theoretical one expected in the case, when both PS and P4VP+HABA occupy the surface in the accordance with the assembly composition. Hence, the film surface is enriched with PS having the low surface tension. This is also confirmed by comparison of XPS spectra measured at the detector angles of 0° and 60° (Figure 4.4b). The effective escape depth of electrons varies roughly as cosine of the detector angle. Therefore, the probing depth is maximal at 0° decreasing twice at 60° . Comparison of $r_{N/C}$ at these angles shows decrease of the nitrogen content by 2.2 times when measured at 60° . Another important conclusion of the spectra analysis is that unbound HABA is not presented on the film surface probably locating at the lower interface.

After extraction of HABA by rinsing in methanol, the N 1s signal has to arise only from P4VP. Analysis of N 1s and C 1s spectra at 0° (Figure 4.4c) shows that the nitrogen content ($r_{N/C} = 0.146$) is very close to the nitrogen fraction in S36V4. This gives evidence of homogeneous distribution of P4VP in the near-surface region of the porous film independently on the detector angle. The results above can be explained as follows. P4VP+HABA cylinders terminated with thin PS layer on the film surface open during HABA extraction turning into the channels. Since the interior side of the channels is covered with P4VP block the opening of the channels leads to apparent increase of the N 1s signal on the XPS spectra.

Discussion

The results of XPS and X-ray reflectivity measurements show the interfacial behavior untypical for the perpendicular oriented cylinders. Indeed, as discussed in Chapter 1, preferential wetting of interfaces induces the parallel alignment of microdomains. Our results can be interpreted in the framework of the model proposed by M. H. Rafailovich *et al.* [Liu94] to explain the co-existence of perpendicular and parallel oriented cylinders in solvent cast PS-*b*-P2VP films. Similarly, the P2VP block was found to be adsorbed on Si substrate, while the

PS block having the low surface energy occupied the film surface. They demonstrated that the individual P2VP cylinders with the different orientations are located between these two wetting layers, as shown in Figure 4.5a. This model can be easily adapted to explain our

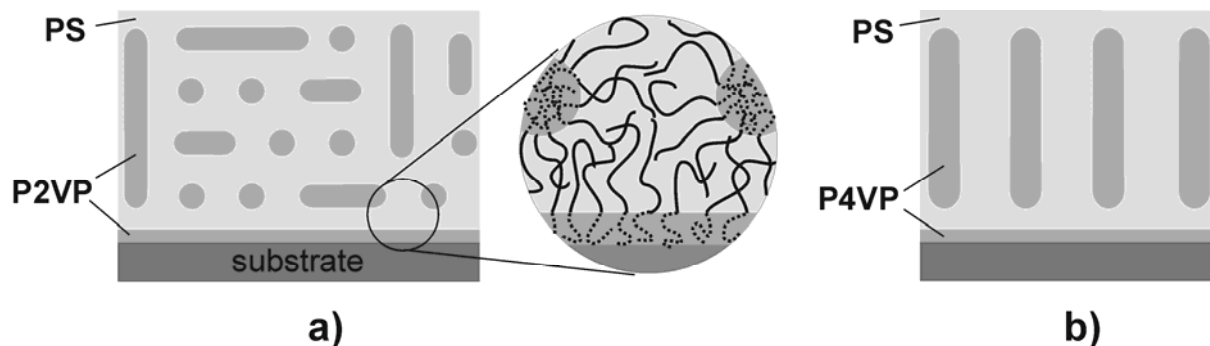


Figure 4.5. Schematic representation of a cross-sectional view of a) PS-*b*-P2VP film showing the co-existence of parallel and perpendicular cylinder and b) S36V4+HABA film dip-coated from 1,4-dioxane solution.

results. Figure 4.5b shows the supposed cross-sectional view of S36V4+HABA film. A layer of the $C\perp$ microdomains lies on a brush produced by the assembly chains strongly adsorbed on Si substrate by the P4VP+HABA block. The upper ends of cylinders are rounded and terminate with the PS block, which allows minimizing the air interface energy. Analogous structure was reported by P. Mansky *et al.* [Man95] in PS-*b*-PBd films cast on water surface. The \perp orientation of PBd cylinders preserved upon temperature annealing and, therefore, was suggested to be metastable. The reasons why the P4VP+HABA cylinders adopt the \perp orientation will be considered in the next Chapter within more complex model proposed to explain our further results.

4.2. S36V4+HABA films deposited from chloroform

Characterization of morphology

The large scale AFM images of the S36V4+HABA films deposited from chloroform solution demonstrate the terrace formation (Figure 4.6). The terrace height is about 16 nm. The films are very smooth inside of the terraces with rms roughness of about 0.3 nm for $1 \times 1 \mu\text{m}^2$ lateral scale. A fine structure of the unwashed films is not visible because of the poor contrast in mechanics between PS and P4VP+HABA microdomains. Rinsing the films with methanol develops the fine structure appearing in the AFM images (Figure 4.7) as a

fingerprint like pattern. We attribute it to in-plane P4VP+HABA cylinders ($C//$), which are transformed into the grooves by the rinsing procedure.

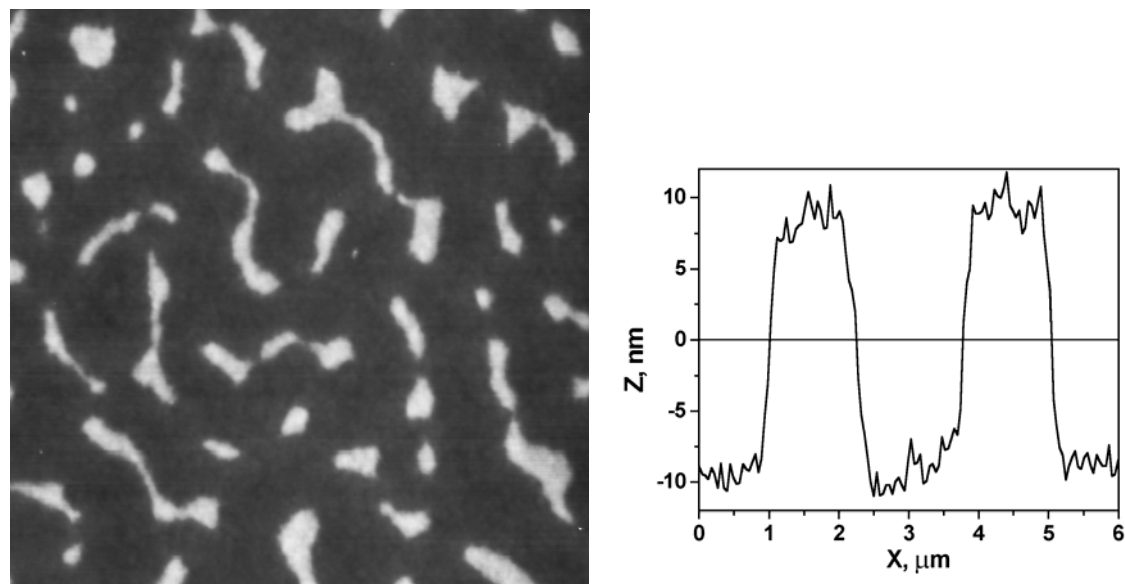


Figure 4.6. AFM image with corresponding cross-section of S36V4+HABA film dip-coated from chloroform solution, the average thickness 40 nm (ellipsometry), lateral scale $16 \times 16 \mu\text{m}^2$.

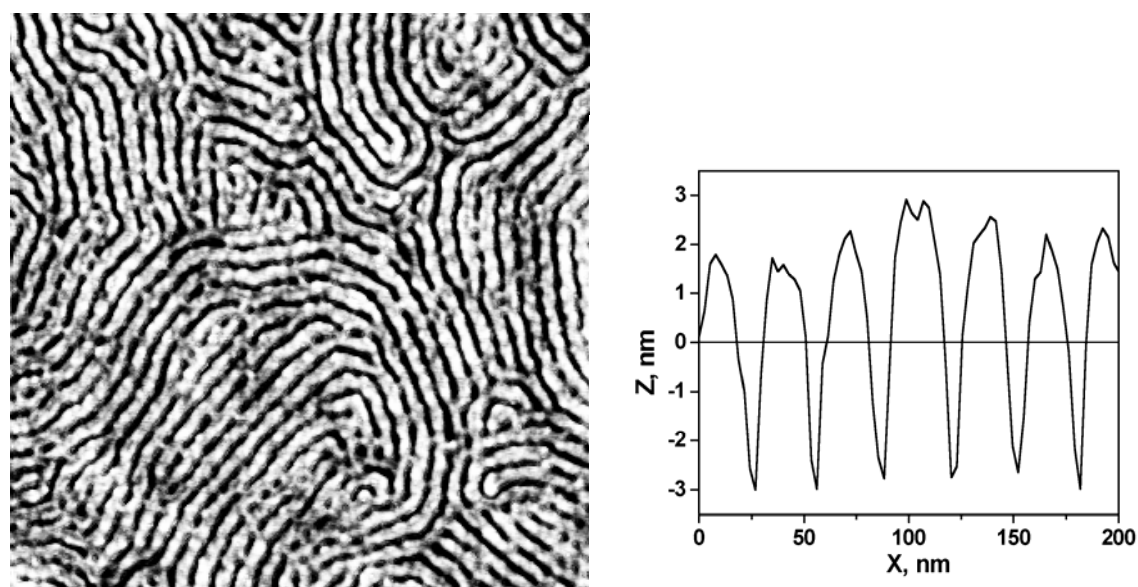


Figure 4.7. AFM image with corresponding cross-section of S36V4+HABA film dip-coated from chloroform solution and rinsed in methanol, the average thickness 40 nm (ellipsometry), lateral scale $1 \times 1 \mu\text{m}^2$.

The mean distance between the neighbor grooves is 30–31 nm (PSD plot). This is significantly higher than in the $C\perp$ films and in the bulk (22–23 nm). The in-plane

microdomain periodicity averaged over a large sample area is determined with GISAXS. The horizontal profile ($\Phi=1.54^\circ$) of the 2D intensity distribution plot of the 35 nm thick *C//* film after the rinsing procedure is shown in Figure 4.8. The film thickness implies a single layer of the in-plane P4VP+HABA cylinders transformed into grooves by rinsing with methanol. Scattering from the skin-deep in-plane grooves gives rise to the low-intensity out-of-plane peak, which position corresponds to the mean periodicity of 29 nm. Fitting of the profile curve with Gaussian distribution functions requires setting two extra peaks in the relative positions 2 and 3 regarding to the first-order peak.

The detailed examination of the AFM topography images shows that the rims are formed on both sides of the grooves, as it is seen in the zoom in Figure 4.9a. The appearance of the rims can be understood from the sketch presented in Figure 4.10. The P4VP+HABA cylinders are located beneath the PS layer occupying the surface of the unwashed films. Immersion in methanol, which is a selective solvent for P4VP and HABA, leads to significant swelling of the P4VP+HABA accompanied by washing HABA out from the cylinders. Therefore, the surface PS layer is ruptured resulting in the regular grooves. The groove walls appear much lighter on the phase image shown in Figure 4.9b indicating that they are covered by the polar P4VP block.

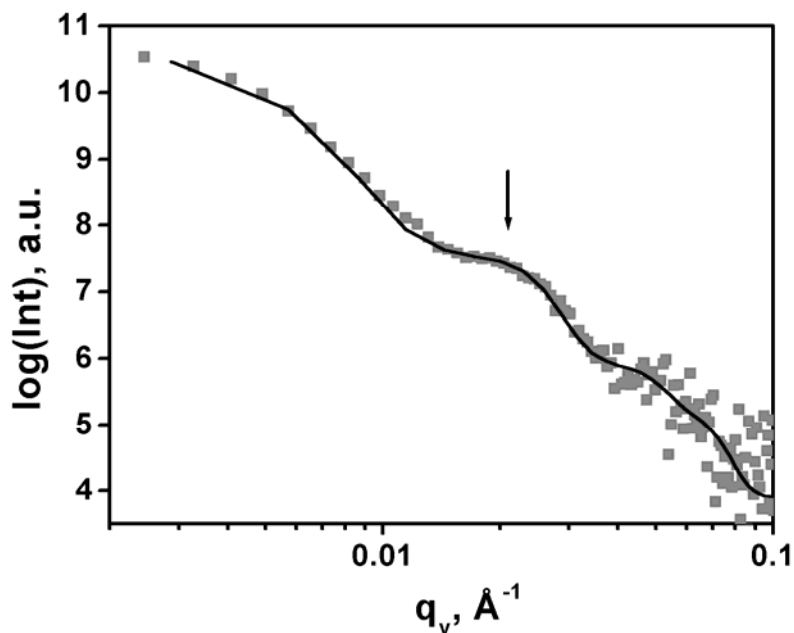


Figure 4.8. Horizontal profile of 2D scattered intensity distribution plot of 35 nm thick S36V4+HABA film switched in the *C//* alignment in chloroform vapors after rinsing with methanol. The solid line shows the Gaussian fit. The arrow indicates the position of the out-of-plane peak. The measurements were performed at the beamline BW4. The angle of incidence $\alpha_i = 1.395^\circ$.

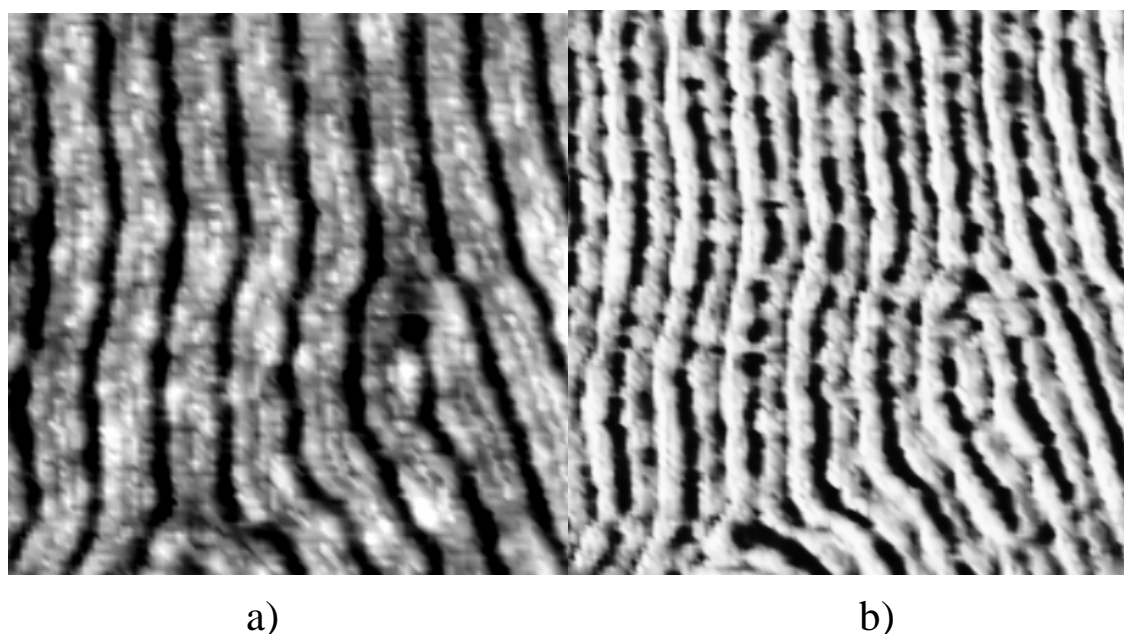


Figure 4.9. AFM topography (a) and phase (b) images of S36V4+HABA film dip-coated from chloroform solution and rinsed in methanol, 40 nm thick, lateral scale 300×300 nm².



Figure 4.10. Sketch showing the transformation of the parallel P4VP+HABA cylinders into the grooves.

Characterization of the surface chemical composition

The further evidence of the above presented model comes from the XPS spectra of the C// film. The survey and detailed N 1s and C 1s XPS spectra of the unwashed film are shown in Figure 4.11a,b. Analysis of the spectra demonstrates that the nitrogen content ($r_{N/C}=0.0077$) in the near-surface region is even smaller than for the S36V4+HABA films deposited from 1,4-dioxane, which clearly indicates the formation of a thin PS layer on the film surface. However, the nitrogen distribution is significantly changed after the rinsing procedure. N 1s and C 1s spectra presented in Figure 4.11c give the ratio $r_{N/C}$ (0.0176) which is notably higher than the theoretical value (0.0118) expected in the case, when both PS and P4VP occupy the surface in the accordance with the S36V4 composition. This excess of P4VP on the surface is

explained by rupture of the upper dense PS layer during rinsing procedure as shown in Figure 4.10.

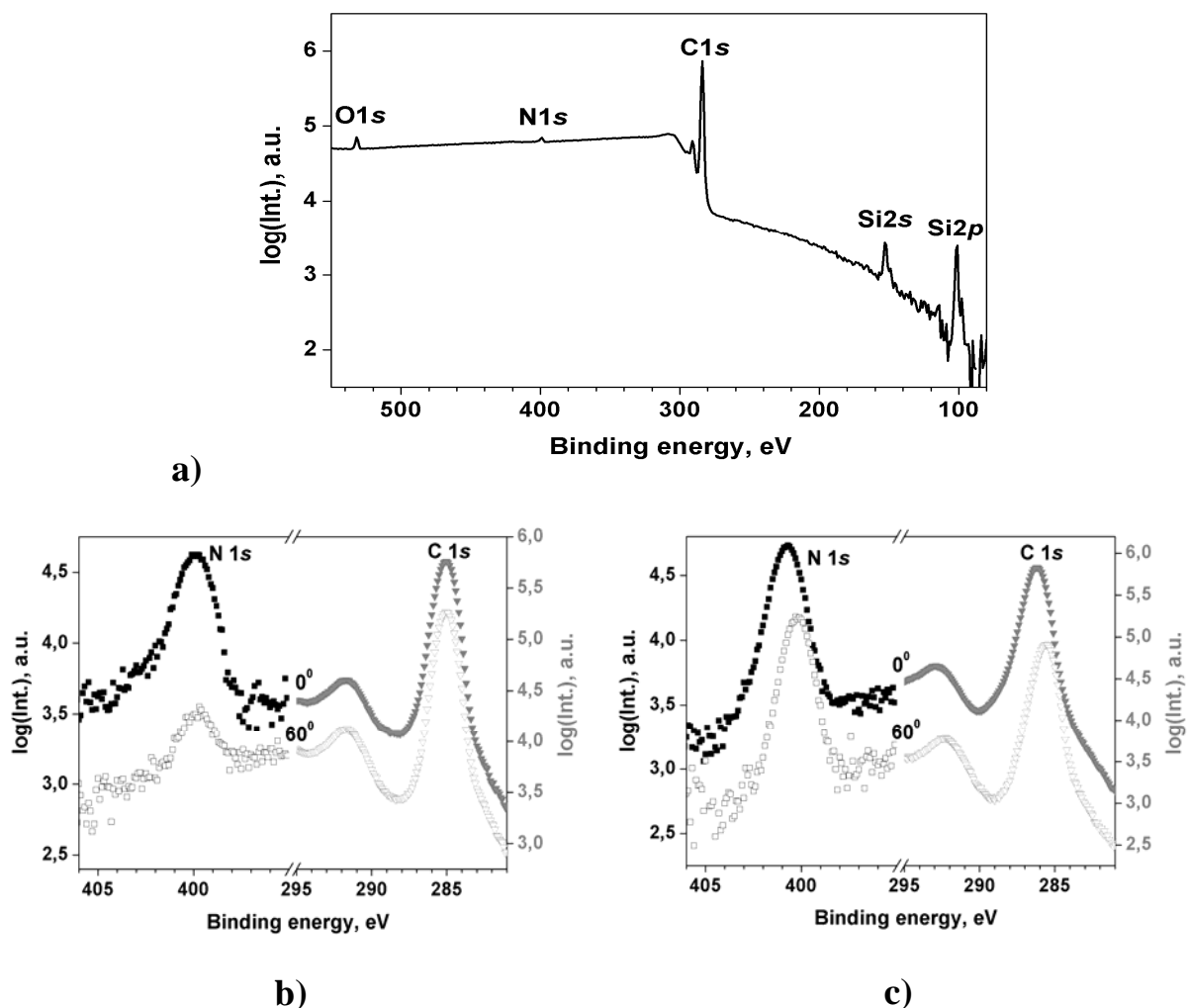


Figure 4.11. XPS spectra of S36V4+HABA film as switched into the in-plane alignment in chloroform vapors (a, b) and after rinsing with methanol (c): a) survey spectrum at the detector angle of 0° ; b) and c) N 1s and C 1s spectra at the detector angles of 0° and 60° .

Discussion

The periodicity discrepancy and the fact that the height of terraces is twice less than the spacing of the in-plane cylinders can be explained as follows. It is necessary to note that the measured repetition periods of the C_\perp and C_\parallel microdomains relate one another as $1:\sqrt{2}$. This suggests the square packing of the C_\parallel microdomains, as schematically shown in Figure 4.12. Indeed, the distance between the neighbor cylinders in the (1,1) plane of the square lattice is $\sqrt{2}$ of the lattice period L_o (22 nm). The height of the terraces shown in Figure 4.12

by a step is $L_0/\sqrt{2}$, *i.e.* ~ 16 nm. However, we found no other examples of such an arrangement of the in-plane cylinders in the literature.

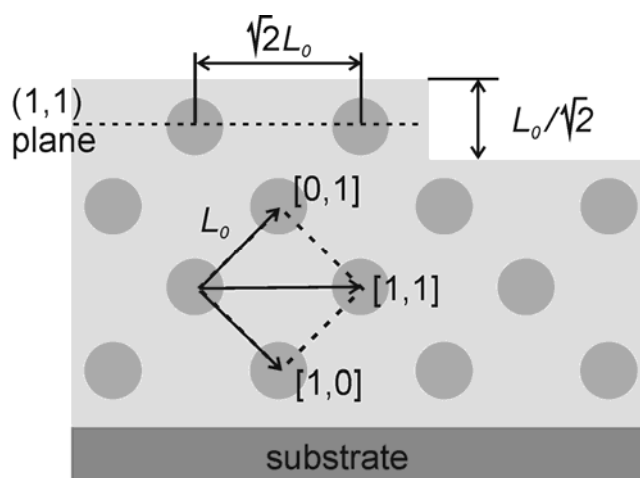


Figure 4.12. Schematic representation of the square arrangement of $C//$ microdomains.

Alternatively, the periodicity discrepancy can be explained considering the drying process of a freshly deposited film. Upon drying, the swollen assembly film experiences the microphase separation into the C morphology. The film interfaces induce the parallel alignment of the C microdomains. We assume that the vitrification of the P4VP+HABA microdomains occurs early than the PS matrix. The possible reason for this is the aggregation of HABA molecules as a result of the poor solubility in chloroform. The vitrified cylinders lose the ability for re-arrangement in the swollen PS matrix, hence, their in-plane periodicity becomes “frozen”. Further solvent evaporation leads only to shrinkage of the $C//$ structure in the direction normal to the film plane, as shown in Figure 4.13. In the dry state, the hexagonal lattice becomes significantly distorted. In the plane parallel to the film surface, the lattice period remains equal to that of the swollen structure L_0^{swollen} . This value corresponds to the repetition period of the grooves observed with AFM. The elevated in-plane period is compensated by decreasing the distance between the cylinder planes in the normal direction. This interplane spacing in the dry state becomes a little less than $\sqrt{3}/2 L_0$ (19 nm). Hence, the related height of the terraces is less than $\sqrt{3}/2 L_0$ too. Distortion of the hexagonal lattice in the direction perpendicular to the film plane was also observed by G. Kim and M. Libera [Kim98] for cast PS-*b*-PBd-*b*-PS *tri*BC films.

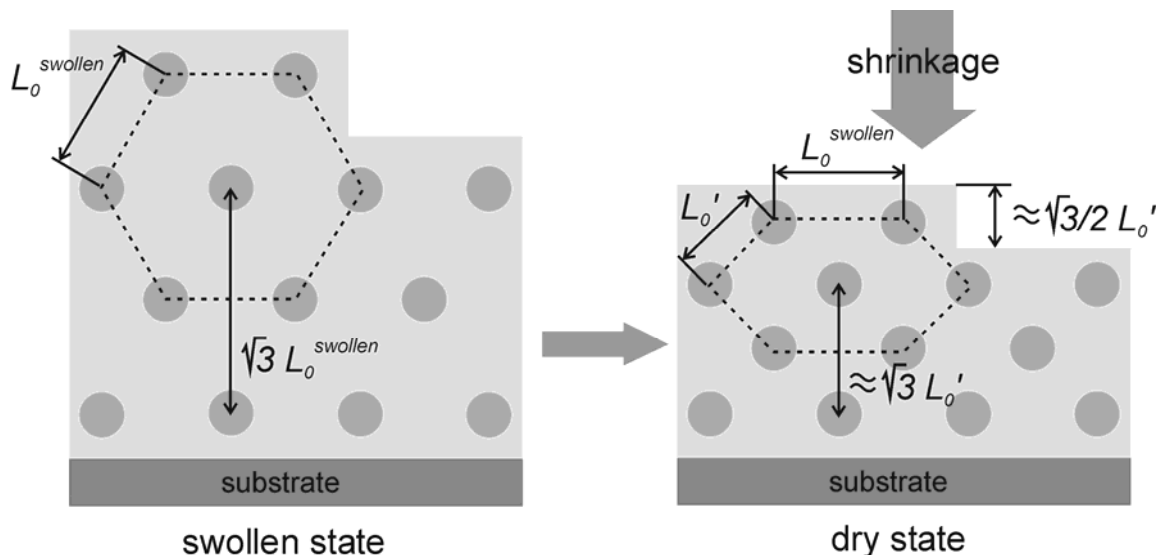


Figure 4.13. Schematic representation of formation of the distorted hexagonal $C//$ morphology.

4.3. S33V8+HABA films

The surface morphology of the S33V8+HABA films deposited from 1,4-dioxane and chloroform solutions is characterized with AFM. The unwashed films are smooth and featureless. However, rinsing in methanol develops the microdomain structure of the films. The representative AFM images of the films deposited from chloroform and 1,4-dioxane are shown in Figure 4.14. The images exhibit the similar patterns formed by the worm-like grooves. The principal difference is the mean distance between the neighbor grooves, which is 33 nm (PSD plot) for the films deposited from chloroform and 26 nm from 1,4-dioxane. The observed patterns can be attributed to $C//$ or $L\perp$ morphologies, because they have the similar appearance in AFM images.

To clarify the situation, we performed ellipsometric measurements. The unwashed films show the high refractive index (1.655 ± 0.005), which is attributed to the significant fraction of HABA in the films. After the rinsing procedure, we observed the considerable decrease of the refractive index. In particular, the refractive index of the films deposited from chloroform is ~ 1.41 , which corresponds to the pore fraction of 0.295 (Bruggeman). This value is close to the HABA fraction in the S33V8+HABA assembly of the equimolar composition (0.312). Therefore, the volume fraction of the P4VP+HABA microdomains in the films is 0.43, which gives strong evidence for the $L\perp$ morphology.

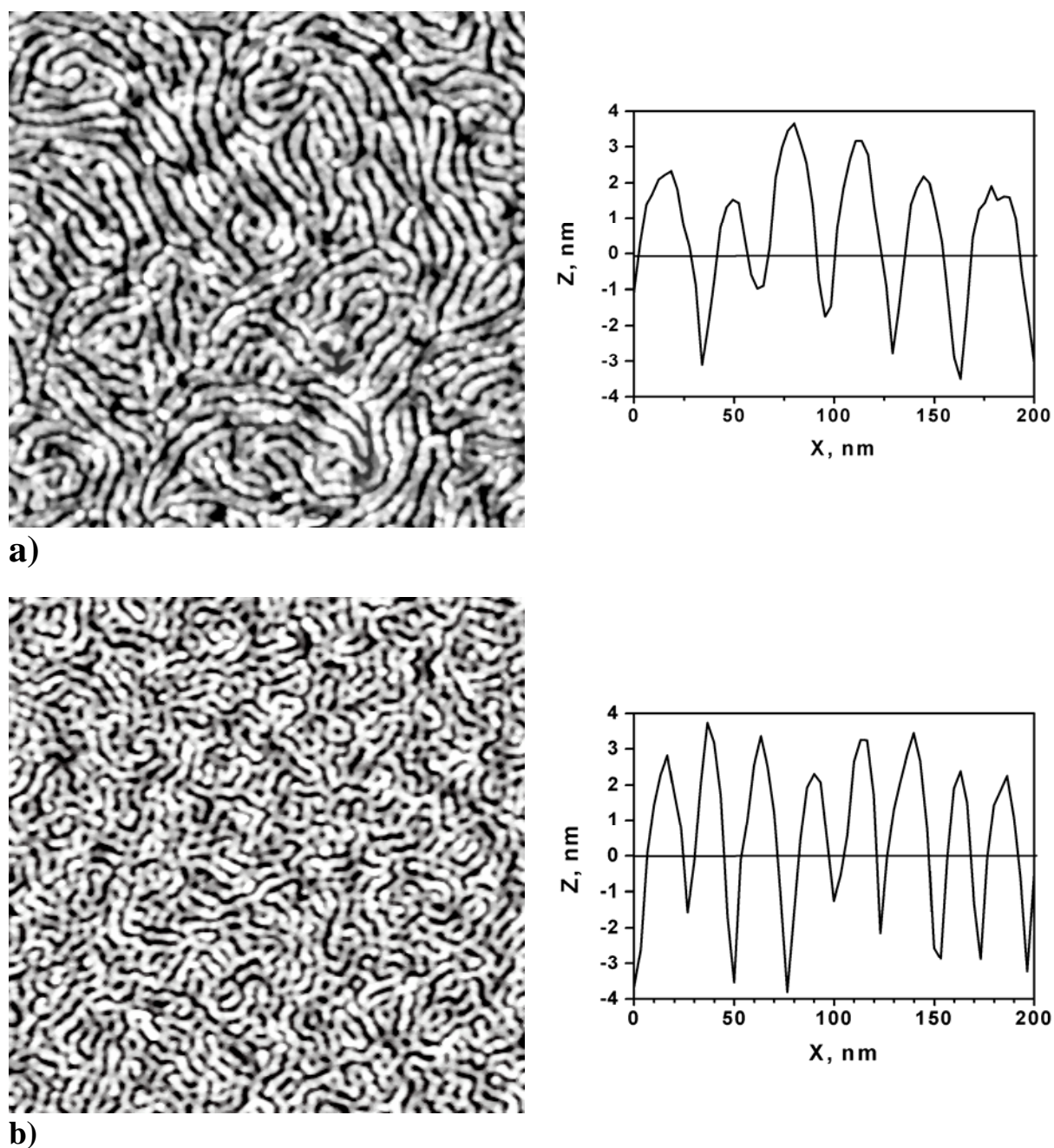


Figure 4.14. AFM images with corresponding cross-sections of S33V8+HABA films a) spin-coated from chloroform solution, 84 nm thick and b) dip-coated from 1,4-dioxane solution, 48 nm thick after rinsing with methanol, lateral scale $1.0 \times 1.0 \mu\text{m}^2$.

However, the ellipsometric measurements gives no definite answer on the morphology of the films deposited from 1,4-dioxane. The refractive index of the washed films is ~ 1.45 , which corresponds to the pore fraction of 0.228. The pore fraction indicates that only $\sim 65\%$ HABA is located in the P4VP+HABA microdomains. Remaining HABA occupies the film interfaces, what is apparent from the decrease of the film thickness after the rinsing procedure. The low effectiveness of assembling P4VP and HABA as compared to chloroform

can be explained as follows. The PS-*b*-P4VP forms micelles in 1,4-dioxane, as proved by the DLS measurements. The P4VP block is in the micelle core, which limits its accessibility for HABA molecules in solution. The film porosity corresponds to the volume fraction of the P4VP+HABA microdomains of ~ 0.38 . This value is appreciably higher as compare to the L/C transition boundary (0.32) found for the PS-*b*-P4VP+PDP assembly. [Rou99] The SCF theory predicts that the L/C boundary is 0.315 at $\chi N \rightarrow \infty$ and shifts to the higher values with decreasing χN . In particular, the P4VP+HABA fraction of 0.38 corresponds to $\chi N = 13$, which is close to ODT. [Mat2001] It is obviously not the case of the S33V8+HABA assembly demonstrating high capability to the self-organization. This suggests that the observed morphology is rather $L\perp$ than $C//$. The detailed examination of the AFM images allows also to assume the co-existence of the $L\perp$ and $C\perp$ morphologies.

Chapter 5. Ordering of PS-*b*-P4VP+HABA films by solvent vapor annealing

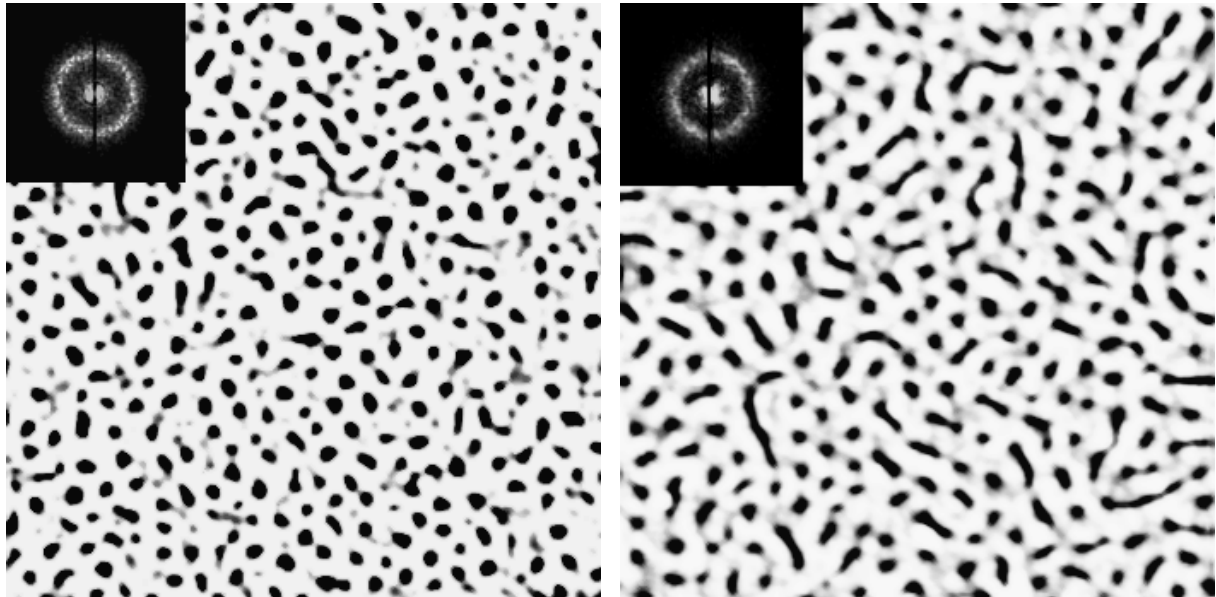
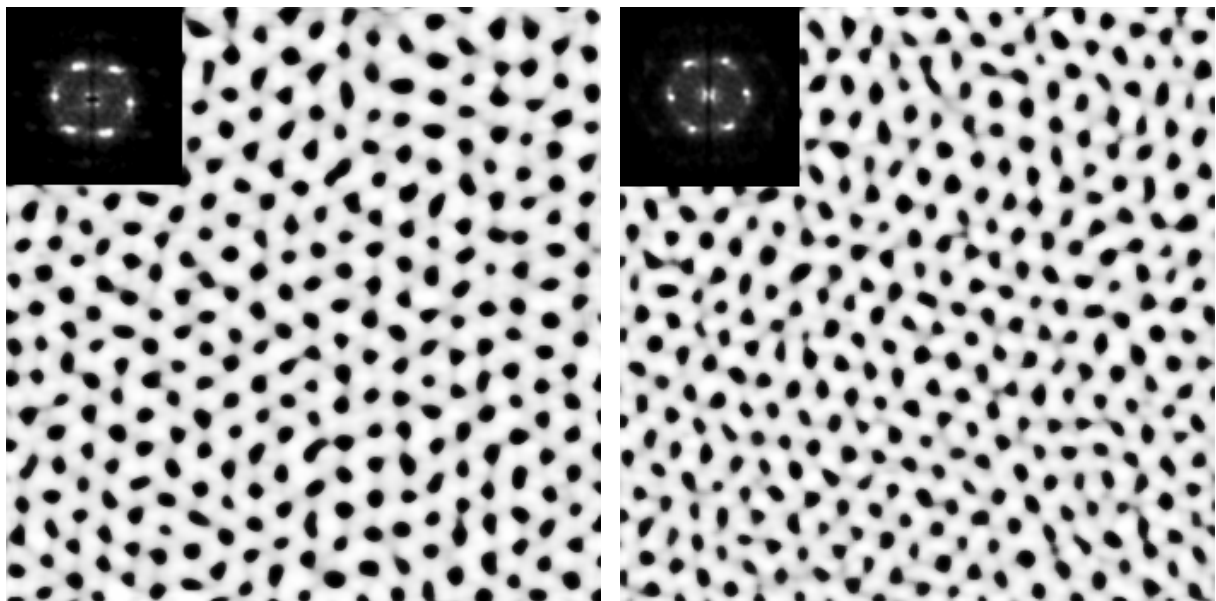
*Swelling of BC films in solvent vapors (solvent vapor annealing) is an elegant approach to promote BC ordering.[Elb2002] Furthermore, it appears to be a single possible way of order improvement for SMA of PS-*b*-P4VP+HABA. In this chapter, we characterize PS-*b*-P4VP+HABA films swollen in vapors of 1,4-dioxane and chloroform. We demonstrate the high potential of the PS-*b*-P4VP+HABA assembly to ordering.*

5.1. Dioxane vapor annealing of S36V4+HABA films

We found that swelling of S36V4+HABA films deposited from 1,4-dioxane solution in vapors of this solvent affects the order of the $C\perp$ microdomains. To investigate the influence of solvent vapor annealing time and the film swelling degree on the structural order we performed a comparative statistical analysis of AFM images (see Section 2.2.2). As a reference we used the AFM image of the “as deposited” film presented in Figure 4.1. The analysis of this image shows that nearly half of the pores has the number of neighbors different from 6 (*i.e.* defects). The orientational order is short-range with the correlation length (AF plot) not exceeding three interpore distances. This is also apparent from a smashed ring in the FFT plot (see Fig. 4.1). This indicates a liquid-like order of microdomains. The interpore distance distribution parameterized by the standard deviation (σ) is 19%. This is comparable with the values reported for an optimized $C\perp$ PS-*b*-PMMA film obtained by the “neutral surface” approach. [Gua2002] The film reveals quite broad pore size distribution with σ of 33% and the significant ellipticity of pore shape ($e = 0.69$). We observed the similar ordering degree for the various film thicknesses ranging from 20 to 100 nm.

We swelled “as deposited” films to different swelling ratios (r_{sw}) defined as the ratio of the film thickness in the swelled and dry states. The desired swelling ratio was reached for 5–40 min. Afterwards, the films were removed from 1,4-dioxane vapors and allowed to dry. The AFM images of the films after rinsing with methanol are presented in Figure 5.1. The defect fraction and the standard deviation of the interpore distances obtained from analysis of the images are plotted vs. the swelling ratio in Figure 5.2. Comparison of the AFM images shows that the fraction of elongated pores increases on an early stage of swelling. As a result,

the mean pore ellipticity increases reaching the maximum (0.73) at $r_{\text{sw}} = 2$. This is accompanied by the noticeable rise of the defect fraction (59%) and the mean interpore distance (27 nm). However, the situation is drastically changed upon further swelling the films. We observed considerable improvement of the hexagonal order at the swelling ratios of 2.5–3. The AF plots suggest the quasi-long-range order of microdomains with the correlation length above nine interpore distances. The $500 \times 500 \text{ nm}^2$ AFM images in Figure 5.1 exhibit

 $r_{\text{sw}} = 1.5$ $r_{\text{sw}} = 2.0$  $r_{\text{sw}} = 2.5$ $r_{\text{sw}} = 3.0$

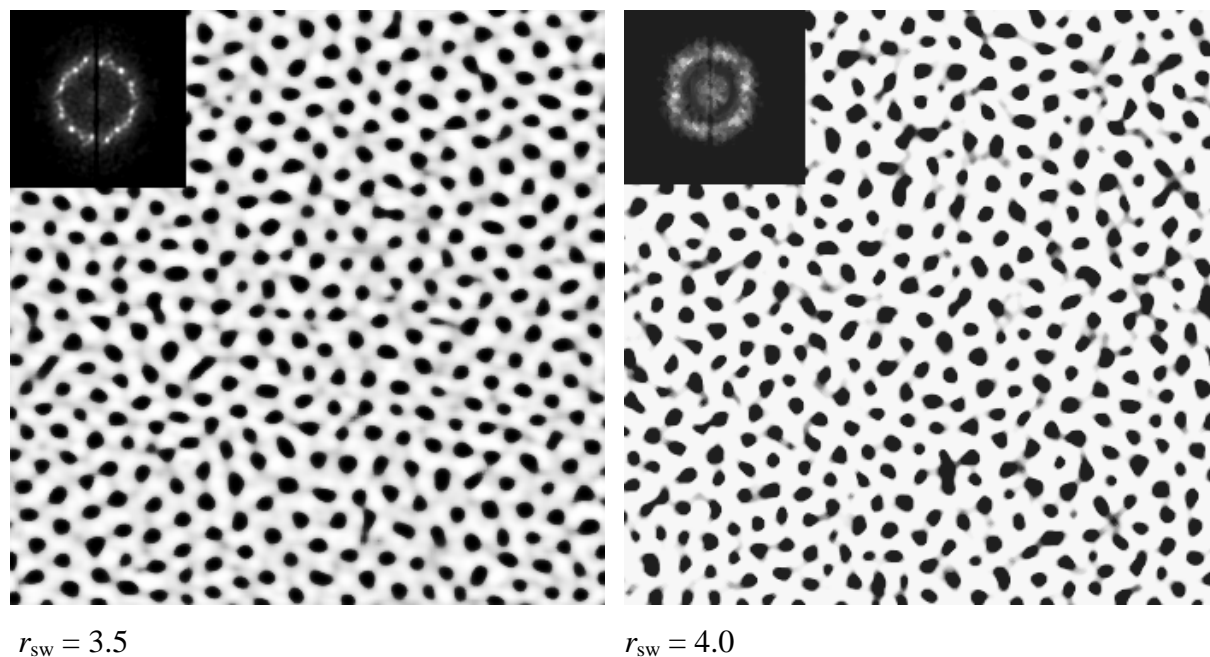


Figure 5.1. AFM images with corresponding 2D FFT plots in the insets of S36V4+HABA films after 1,4-dioxane vapor annealing (the numbers below the images show the swelling ratio) rinsing with methanol, 61–68 nm thick, lateral scale $500 \times 500 \text{ nm}^2$. The images are flattened for presentation.

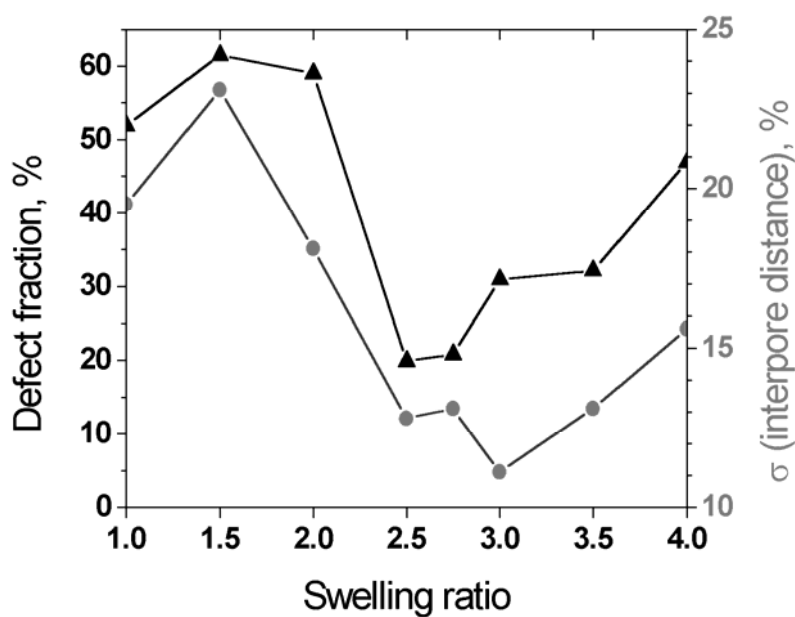


Figure 5.2. Dependence of the defect fraction (black) and the standard deviation (σ) of the intercore distance distribution (gray) on the swelling ratio of S36V4+HABA films swollen in 1,4-dioxane vapors.

single grains, as follows from the “six-point” FFT plots given in the insets. The distributions of the interpore distances and the pore size become relatively narrow with σ of 11–13% and 16–20%, respectively. The pore shape is also improved ($e = 0.57$ – 62). As a result, the defect number is significantly reduced ranging from 20% to 30%. The interpore distance decreases to 25 nm (PSD plot). All the order parameters remain unchanged or slightly increase with the further swelling. The exceptions are the orientational order and the interpore distance distribution. We observed the gradual decay of the orientational order at $r_{sw} > 3$. In particular, the correlation length lowers from seven to four interpore distances when the swelling ratio increasing from 3.5 to 4. The interpore pore distance distribution also gradually broadens showing the standard deviation of 16% at $r_{sw} = 4$. Therefore, the orientational and translational orders become comparable to the “as deposited” film. Assuming that the order degree of the swollen state is preserved by rapid drying a film, we can conclude that the transition to the *dis* micellar state occurs at the swelling ratios of ~ 4 – 5 . The close swelling ratios for ODT were obtained by M. Shibayama *et al.* [Shi83] and K. Mori *et al.* [Mor90] for PS-*b*-PI films. We should also note that swelling of S36V4+HABA films to the swelling ratio ≥ 2.5 resulted in formation of terraces with the height of ~ 6 nm and the lateral dimensions ranging from hundreds nanometer to microns.

As it is seen from the analysis above, S36V4+HABA films reveal the optimal structural order and the pore uniformity in the relatively narrow range of the swelling ratios (2.5–3). We compared the results of the AFM image analysis and the GISAXS measurements of the S36V4+HABA film swollen to $r_{sw} = 2.75$, which is in the middle of the optimal swelling range. The horizontal profile of the 2D scattered intensity distribution plot ($\Phi = 1.54^\circ$) of the film after rinsing with methanol is shown in Figure 5.3. Two pronounced peaks and the shoulder can be easily seen in the profile. Fitting of the profile curve with Gaussian distribution functions results in the relative peak positions of $1:\sqrt{3}:\sqrt{7}$, which is indicative of the hexagonal in-plane order. The mean interpore distance deduced from the position of the first-order peak is 26 nm, which is close to the AFM data. The ratio between the variance of the Gaussian curve describing the first-order peak and the peak position ($\approx 13\%$) characterizes the interpore distance distribution. This value excellently agrees with the results of the analysis of the AFM images (see Figure 5.2).

In the next experiment, we studied the effect of the swelling duration on the structural order. The 40 nm S36V4+HABA film was swollen in 1,4-dioxane vapors to $r_{sw} = 2.75$ for about 8 hours and then dried for several minutes. The $1 \times 1 \mu\text{m}^2$ AFM image of the film surface is shown in Figure 5.4. Six sharp first-order peaks and the presence of the higher order

reflections are clearly seen in the FFT plot (see the inset) demonstrating the almost perfect hexagonal order which spreads over area of $2 \mu\text{m}^2$. The defect analysis exhibits the impressive decrease of the number of defects in the structure (3%). The distributions of the interpore distances and the pore size are very narrow with σ of $\sim 10\%$. This experiment clearly shows that although the microphase separation of the blocks in “as deposited” films runs on a time scale of seconds, the re-arrangement of the formed microdomains in a high-order structure requires much longer times.

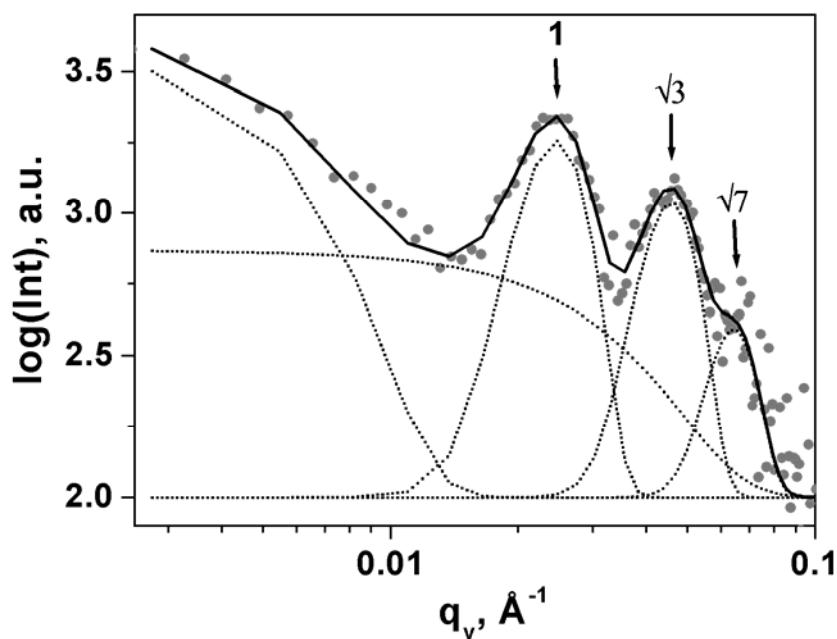


Figure 5.3. Horizontal profile ($\Phi = 1.54^\circ$) of 2D scattered intensity distribution plot of 33 nm thick S36V4+HABA film ordered by 1,4-dioxane vapor annealing ($r_{\text{sw}} = 2.75$) after the rinsing procedure. The fit curve (solid line) is the sum of the Gaussian curves (dot lines). The arrows show the positions of the out-of-plane peaks.

The ellipsometric measurements show that the 1,4-dioxane vapor annealing does not affect the film porosity as compared to the “as deposited” films. This is confirmed by the X-ray reflectivity measurements. Figure 5.5. shows the X-ray reflectivity curve of the 33 nm thick film after 1,4-dioxane vapor annealing ($r_{\text{sw}} = 2.75$) and rinsing with methanol. We obtained the reasonable fit of the reflectivity curve using the model similar to that proposed in Section 4.1 for the “as prepared” film. As it is seen from the depth profile of the electron density (the inset in Figure 5.5), the pores cross the film from the top to the bottom except ~ 2 nm thick dense layer (presumably P4VP) on Si substrate. The electron density of the porous

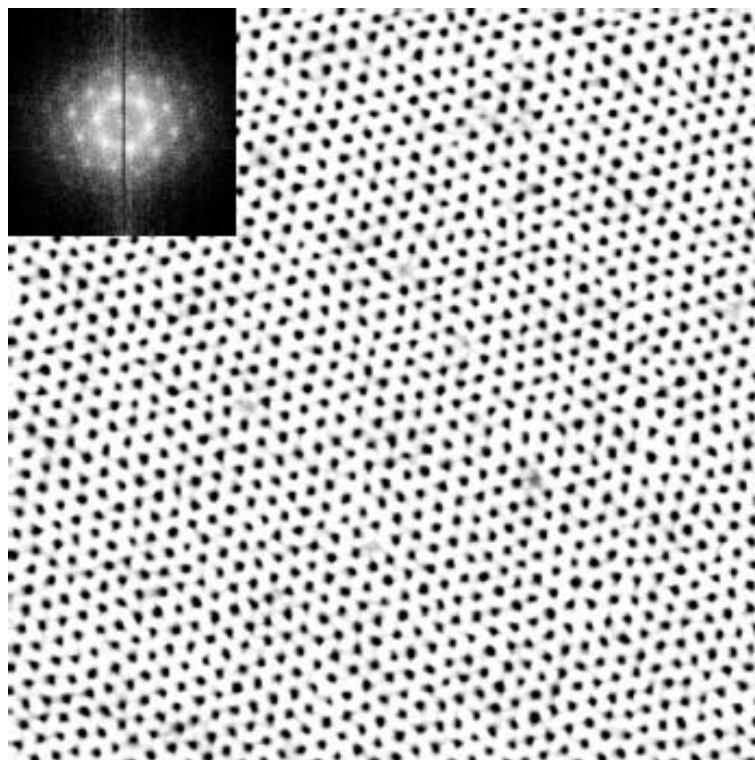


Figure 5.4. AFM image with corresponding 2D FFT plot in the inset of 40 nm thick S36V4+HABA film after 1,4-dioxane vapor annealing (slow swelling to $r_{sw} = 2.75$) and rinsing with methanol, lateral scale $1 \times 1 \mu\text{m}^2$.

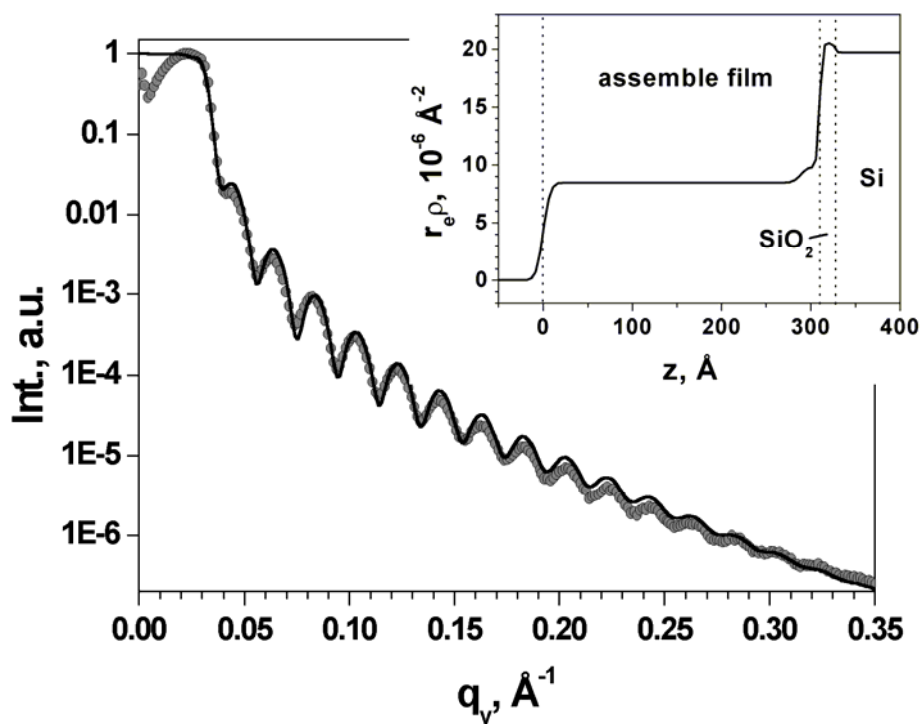


Figure 5.5. X-ray reflectivity curve and fit (solid line) with corresponding depth profile of the electron density in the inset of 33 nm thick S36V4+HABA film after 1,4-dioxane vapor annealing ($r_{sw} = 2.75$) and rinsing with methanol.

layer ($8.45 \cdot 10^{-6} \text{ \AA}^{-2}$) corresponds to the pore fraction of about 11%, what is close to the porosity of “as prepared” films. The XPS spectra are also similar to “as prepared” films, indicating that a thin PS layer covers the film surface.

5.2. Chloroform vapor annealing of S36V4+HABA films

We found that the swelling ratios of 2.5–3 were also optimal in terms of the structural order for S36V4+HABA films annealed in chloroform vapors. The representative $1 \times 1 \text{ \mu m}^2$ AFM image of the film deposited from chloroform and swelled in vapors of this solvent to $r_{\text{sw}} = 2.75$ is shown in Figure 5.6. As compared to the AFM image of the “as deposited” film

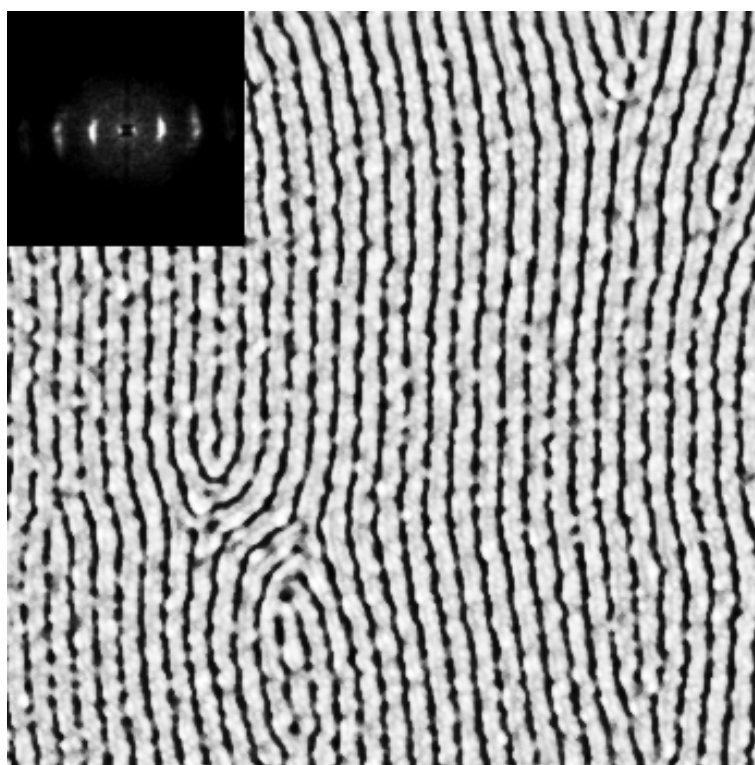


Figure 5.6. AFM image with corresponding 2D FFT plot in the inset of 79 nm thick S36V4+HABA film after chloroform vapor annealing ($r_{\text{sw}} = 2.75$) and rinsing with methanol, lateral scale $1 \times 1 \text{ \mu m}^2$.

(Figure 4.7), we note the significant improvement of the order after chloroform vapor annealing. The AFM image acquired within a terrace reveals a single grain with the small number of topological defects (dislocations and disclinations). [Hah2001] This is also apparent from the characteristic two-point pattern of the first-order peaks in the FFT plot (see the inset in Figure 5.6). The first-order peaks are azimuthally broadened indicating slight

variations in the orientation of the in-plane cylinders. The mean spacing between the grooves and the terrace height remain unchanged after the chloroform vapor treatment.

5.3. Dioxane vapor annealing of S33V8+HABA films

We obtain similar results after 1,4-dioxane vapor annealing of S33V8+HABA films deposited from chloroform solution. We attribute the observed surface pattern of the “as deposited” films to the perpendicular oriented lamellae. The representative AFM image of a film swollen in 1,4-dioxane vapors to the swelling ratio of 2.75 is shown in Figure 5.7. We can see that swelling of the films in 1,4-dioxane does not change the \perp orientation of microdomains. The orientational and translational orders are considerably improved, as compared to the “as deposited” film (Figure 4.14a). The mean spacing between the grooves is preserved after the vapor annealing. We observed no formation of terraces for films of various thicknesses, which gives additional evidence of the $L\perp$ morphology.

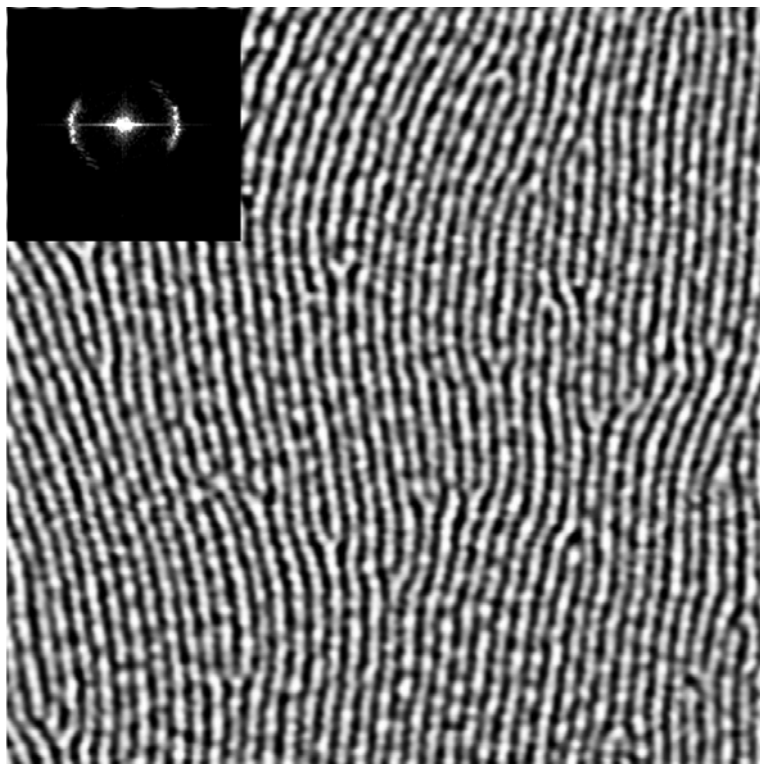


Figure 5.7. AFM image with corresponding 2D FFT plot in the inset of 48 nm thick S33V8+HABA film ordered by swelling in 1,4-dioxane ($r_{sw} = 2.75$) and rinsed with methanol, lateral scale $1.5 \times 1.5 \mu\text{m}^2$.

5.4. Discussion

We suppose that solvent selectivity is a key factor, which determines the orientation of *C* microdomains in S36V4+HABA films. The solubility of the blocks and the DLS data (see Section 2.1) indicate that chloroform is nonselective solvent for S36V4+HABA, *i.e.* it swells similar both blocks. 1,4-dioxane is selective solvent, which swells preferentially the PS block. Here, we propose the scenario allowing explaining the different *C* orientation of the “as deposited” film as well as the evolution of the morphology during solvent vapor annealing. For the discussion bellow, we use the phase diagram shown in Figure 5.8, where χ^* is the measure of incompatibility of the swollen blocks and f^* is the volume fraction of the swollen P4VP+HABA block. Unlike the Flory-Huggins segmental interaction parameter, χ^* is a function of two parameters: the temperature and the solvent concentration. Since S36V4+HABA films are deposited and swollen in solvent vapors at RT, we consider only the concentration dependence of χ^* . In films, instead of the solvent concentration, we can also use the swelling ratio r_{sw} . It is worth noting that the presented phase diagram is similar to the theoretical phase diagram of *di*BCs in melt (see Chapter 1) with the only difference that the direct transition from the disordered (*dis*) state to the *C* morphology is allowed. The direct *dis*→*C* transition was experimentally observed by K. J. Hanley, T. P. Lodge *et al.* [Han2000, Lod2003a] in PS-*b*-PI *di*BC with addition of neutral or selective solvent.

Straight after deposition, a film is highly swollen and the S36V4+HABA assembly is in the *dis* state 1 (Figure 5.8a,b). As the film dries, the swelling of the blocks decreases, consequently, their incompatibility χ^* grows. In the case of nonselective solvent, *i.e.* chloroform, this corresponds to the vertical trajectory 1→3 (f^* is constant) on the phase diagram (Figure 5.8a). At the certain swelling ratio (~4–5), the incompatibility of the blocks induces the direct *dis*→*C* transition. The preferential wetting of the air and substrate interfaces with the PS and P4VP+HABA blocks results in the in-plane alignment of the cylinders. This is accompanied by the terrace formation, as observed with AFM in the dry state 3. Since the drying of the film occurs within seconds, the assembly has no time for the microdomain re-arrangement necessary to minimize the total free energy. The better ordering can be achieved by the subsequent chloroform vapor annealing of the film. The swelling of the film in chloroform vapors corresponds to the reverse trajectory 3→2 on the phase diagram. The final swelling ratio of 2.75 corresponding to the state 2 is above the ODT boundary. The incompatibility and the mobility of the blocks in this state are high enough for rapid improvement of the spatial distribution of the *C* microdomains and their orientational

ordering due to releasing of the topological defects. After removal from vapors, the film rapidly dries and the in-plane ordering of the $C//$ microdomains, which corresponds to the swollen state, becomes “frozen”. As discussed in Chapter 4.1, this leads to the distortion of the hexagonal lattice in the direction perpendicular to the film plane.

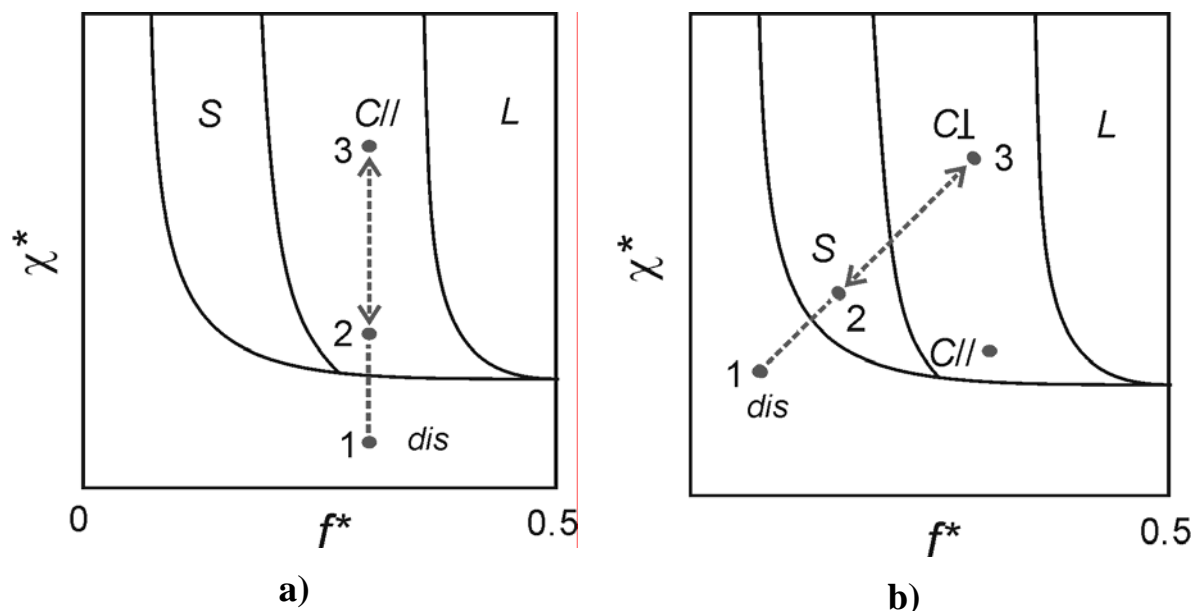


Figure 5.8. Schematic representation of a phase diagram for the S36V4+HABA assembly. Vectors show the transposition directions on the phase diagram for the S36V4+HABA films a) deposited from chloroform solution and ordered by chloroform vapor annealing and b) deposited from 1,4-dioxane solution and ordered by 1,4-dioxane vapor annealing. 1 is the disordered state, 2 is the dry state, 3 is the swollen state.

Considering the films deposited from 1,4-dioxane, we should take into account that the S36V4+HABA assembly gives micelles in solution. After transfer on substrate, the micelles form a *dis* film, which corresponds to the state 1 on the phase diagram (Figure 5.8b). Since 1,4-dioxane is selective solvent for PS, the ratio f^* is shifted towards lower values reflecting preferential swelling of the PS matrix. As the film dries, both χ^* and f^* increase, what corresponds to the diagonal trajectory 1→3 on the phase diagram. When the swelling ratio approaches ~4–5, the incompatibility of the blocks becomes high enough to induce the transition from the disordered micellar state into the ordered BCC S morphology with the (111) plane coincident with the film plane. The further shift in the assembly composition f^* dictates the second transition into the $C\perp$ morphology. The S transitional state 2 is a key point, which allows to explain the perpendicular orientation of the cylindrical microdomains. We suppose that the fast shrinkage of the BCC packed spheres normal to the film plane

results in their coalescence into the \perp aligned cylinders, as illustrated by the sketch in Figure 5.9. The cylinder axes are coincident with the [111] direction of the BCC lattice. The $S \leftrightarrow C$

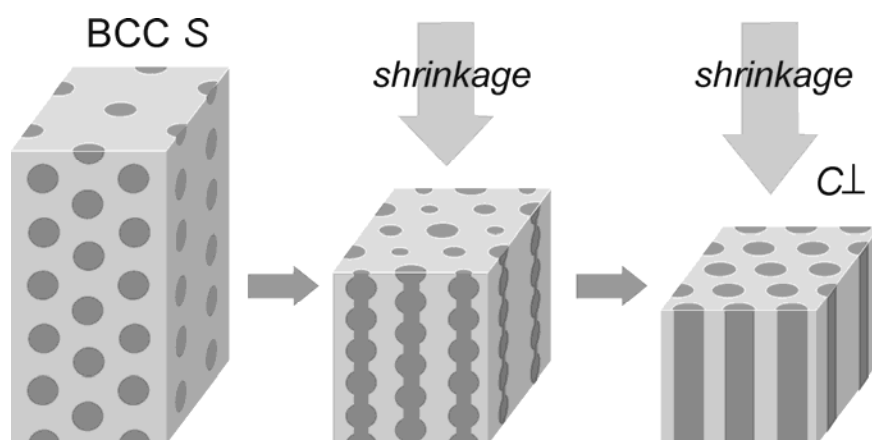


Figure 5.9. Sketch explaining the $S \rightarrow C\perp$ transition in a S36V4+HABA film.

transition through coalescence of S microdomains was reported in several papers [Kop94, Sän97] The subsequent vitrification of the blocks preserves the \perp orientation, which is observed with AFM in the dry state 3. The time of the transition $1 \rightarrow 3$ is too short for the re-arrangement of the $C\perp$ microdomains in the high-ordered structure. Therefore, the following 1,4-dioxane vapor annealing of the film is necessary to allow the ordering. The preferential swelling of the PS matrix results in the reverse diagonal trajectory $3 \rightarrow 2$ on the phase diagram. Analysis of the AFM images (see Figure 5.1) shows the noticeable change in the film structure occurring when the film reaches $r_{sw} \approx 2$. This indicates that the assembly blocks are no longer in the glassy state at this swelling ratio. G. Krausch *et al.* used the same swelling ratio for solvent vapor annealing of *PS-b-P2VP* films. [Elb2002] This swelling ratio corresponds to the state with the C symmetry on the phase diagram. Therefore, free to move, the assembly blocks start to re-arrange to approach the minimum free energy. The film interfaces induce more thermodynamically stable in-plane alignment of the C microdomains. This process of the $C\perp \rightarrow C//$ re-orientation is kinetically slow because of the relatively low mobility of the blocks at this swelling ratio. Therefore, interrupting the swelling, we trap the system in the early stage of the re-orientation. As demonstrated, the swelling of the films to $r_{sw} = 2.5$ results in the sudden order improvement of the $C\perp$ morphology. We attribute this result to the transition of the assembly into the intermediate state with the BCC S morphology. The strong argument in favor of this state is small terraces, which are observed for the samples swollen to $r_{sw} \geq 2.5$. As discussed, the fast drying of the film leads to the shrinkage of

the S structure with the formation of the $C\perp$ morphology. Therefore, the observed good structural order is a result of the fast re-arrangement of the S microdomains in the swollen PS matrix. In experiment, $r_{sw} = 2.5$ was achieved for about 10 minutes. As it is seen in Figure 5.1, the good ordering is maintained to the swelling ratio 3 and with the further swelling decays. We explain it by decrease of the incompatibility χ^* of the significantly swollen assembly blocks. At $r_{sw} > 4$, the orientational order is liquid-like, indicating ODT.

The above discussed model can be also adapted to explain the orientation of the $L\perp$ morphology. However, this requires some additional assumptions, *e.g.* the following transition route: $dis \rightarrow C// \rightarrow L\perp$. Since, the L morphology is not thoroughly characterized; we omit the discussion of the obtained results.

Chapter 6. Re-orientation of microdomains in PS-*b*-P4VP+HABA films by solvent vapor annealing

*In this chapter we investigate the phenomenon of re-orientation of cylindrical and lamellar microdomains in PS-*b*-P4VP+HABA films. We demonstrate that orientation from the perpendicular to parallel state and vice versa can be rapidly switched by swelling in vapors of appropriate solvent. Afterwards, in discussion we propose the model, which allows to explain the experimental results .*

6.1. S36V4+HABA films

We found that alignment of the cylindrical domains in S36V4+HABA films can be easily changed with an appropriate solvent. We used 40–50 nm thick S36V4+HABA films deposited from 1,4-dioxane and chloroform solutions. The obtained samples were broken into two fragments. One fragment was rinsed with methanol and the film structure was characterized with AFM. The second fragment was placed into a closed container with solvent vapors. The film prepared from 1,4-dioxane was swollen in chloroform vapors and, oppositely, the film prepared from chloroform was swollen in 1,4-dioxane vapors. The swelling ratio of 2.75 was found to be optimal in terms of the structural order and reached in 10–20 min. Afterwards, the films was rinsed with methanol and characterized with AFM.

The AFM images of the films deposited from 1,4-dioxane (Figure 6.1a) show the characteristic $C\perp$ pattern. However, chloroform vapor annealing of this film entirely re-orientes the C microdomains into the in-plane alignment, as it is seen in Figure 6.1b. The structural order is comparable to the film deposited from chloroform (see Figure 4.7). The orientational order persists only in a distance of ~ 100 nm and the pattern reveals a lot of topological defects. The situation is significantly improved by the slight increase of the swelling ratio to 3.

Figure 6.2a shows the representative $C//$ pattern of the film deposited from chloroform. The in-plane cylinders are completely switched to the \perp orientation after swelling of the film in 1,4-dioxane vapors, as it is seen in Figure 6.2b. We should note the good level of the structural order, which is only a little worse as compared to the films swelled in 1,4-dioxane vapors to r_{sw} of 2.5–3. We found that such re-alignment occurring in S36V4+HABA films is reversible and can be repeated several times for non-rinsed films.

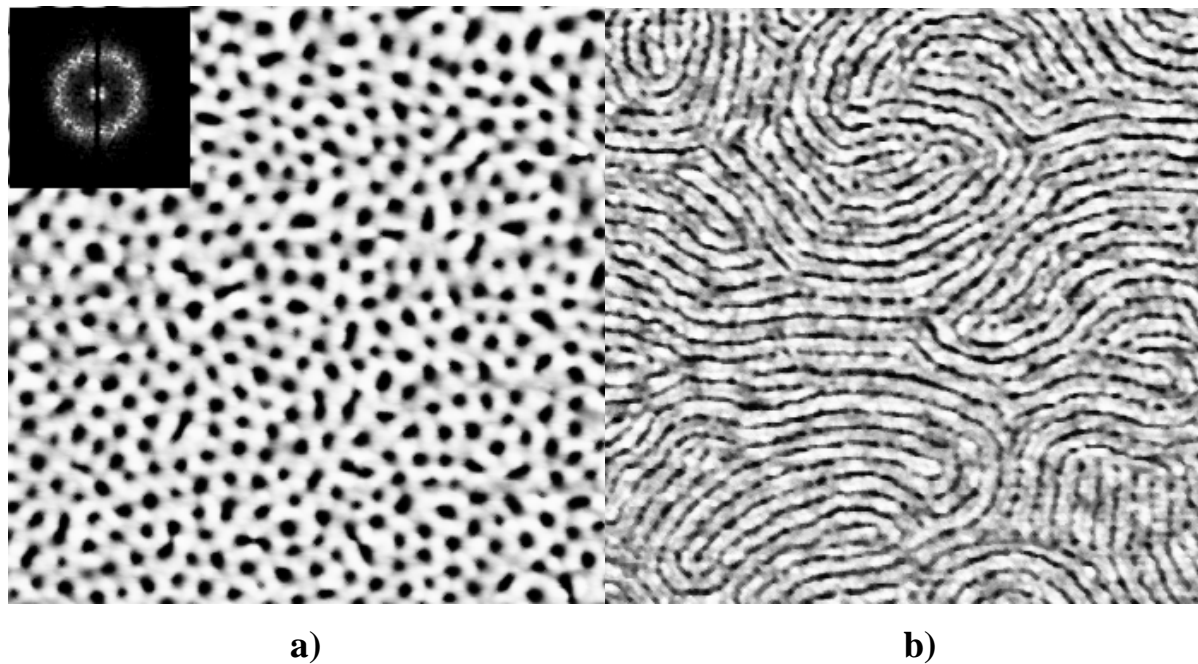


Figure 6.1. AFM images of 40 nm thick S36V4+HABA film a) as deposited from 1,4-dioxane (lateral scale $500 \times 500 \text{ nm}^2$) and b) re-oriented by swelling in chloroform vapors to $r_{\text{sw}} = 2.75$ (lateral scale $1 \times 1 \text{ } \mu\text{m}^2$) after the rinsing procedure.

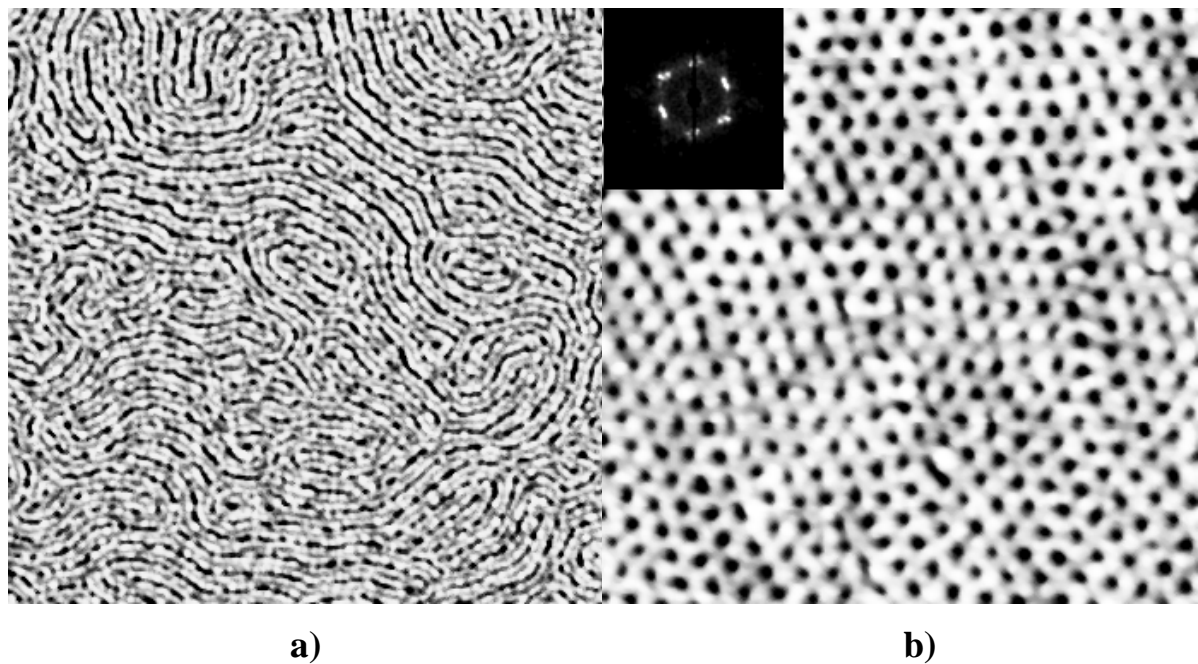


Figure 6.2. AFM images of 50 nm thick S36V4+HABA film a) as deposited from chloroform (lateral scale $1 \times 1 \text{ } \mu\text{m}^2$) and b) re-oriented by swelling in 1,4-dioxane vapors to $r_{\text{sw}} = 2.75$ (lateral scale $500 \times 500 \text{ nm}^2$) after the rinsing procedure.

Kinetics of the re-alignment was monitored by analysis of morphology of the films as a function of time and swelling degree (evaluated *in-situ* with ellipsometry). The $C\perp\leftrightarrow C//$ re-alignment began upon exposure to solvent vapors when the swelling ratio approached 2.0–2.5. Figure 6.3 shows the representative image of the partially re-oriented film, where the co-existence of $C//$ and $C\perp$ morphologies can be seen.

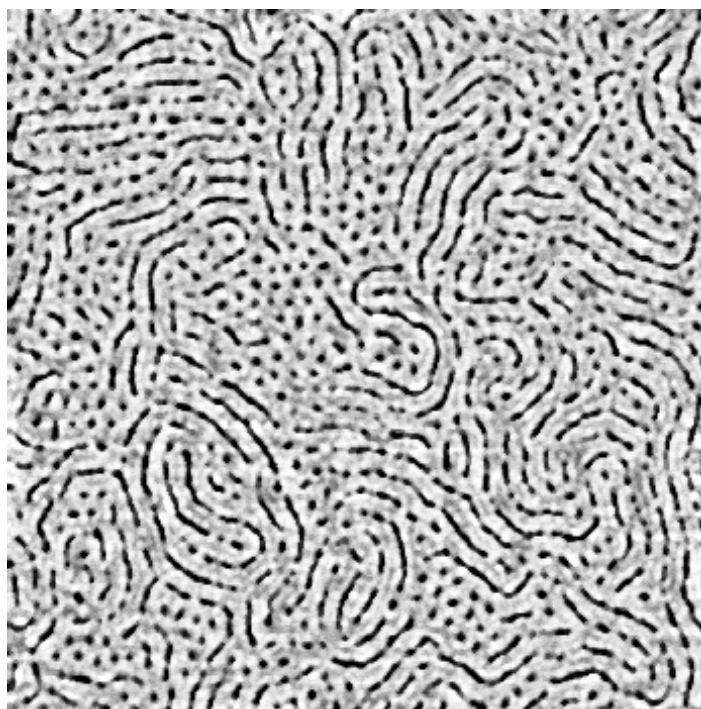


Figure 6.3. AFM image of the 40 nm thick S36V4+HABA film deposited from 1,4-dioxane and partially re-oriented by swelling in chloroform vapors to $r_{sw} \approx 2.5$ after rinsing procedure, lateral scale $1 \times 1 \mu\text{m}^2$.

We should again emphasize that the same switching behavior was found for substrates of *different chemical composition*.

6.2. S33V8+HABA films

We also found the similar switching behavior in S36V4+HABA films. Figure 6.4 shows the $1.5 \times 1.5 \mu\text{m}^2$ AFM image of the film deposited from 1,4-dioxane solution ($L\perp$, Figure 4.14b) and swelled in chloroform vapors to the swelling ratio of 2.75. The washed film displays formation of islands, which have the height of ~ 20 nm. It is featureless within the terraces evidencing the re-orientation of the lamellae into the in-plane alignment. The terrace

height is smaller than it is expected to be from the repetition period of the $L\perp$ microdomains (33 nm). This together with the small size of the terraces clearly indicates that we “froze” the system in the early stage of the terrace formation.

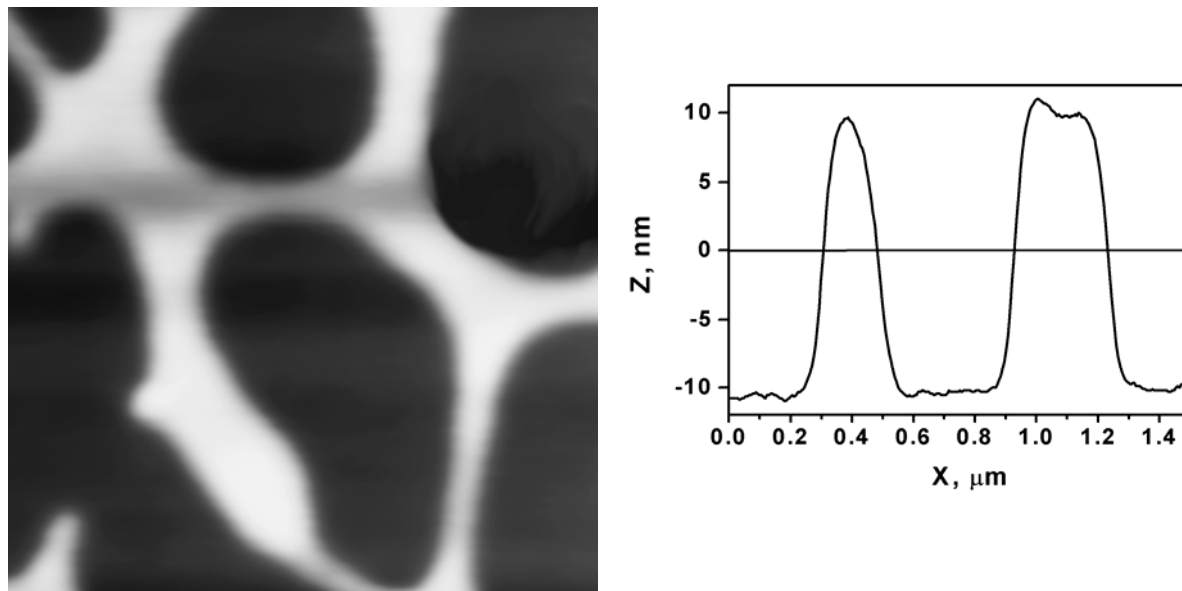


Figure 6.4. AFM image with corresponding cross-section of the 84 nm thick S33V8+HABA film re-oriented by swelling in chloroform solution to $r_{sw} \approx 2.75$, lateral scale $1.5 \times 1.5 \mu\text{m}^2$.

6.3. Discussion

We explain the re-orientation of microdomains occurring upon solvent vapor annealing within the model presented in the Section 5.4. Figure 6.5 shows the transposition routes of the S36V4+HABA assembly on the phase diagram. The assembly film prepared from chloroform solution follows the bottom-up trajectory 1→2 on the phase diagram (Figure 6.5a). This allows the direct $dis \rightarrow C$ transition resulting in surface-induced in-plane alignment of the C microdomains. This preferable orientation can be changed by 1,4-dioxane vapor annealing. Preferential swelling of the PS matrix in 1,4-dioxane leads to the diagonal trajectory 2→3 on the phase diagram. Therefore, at $r_{sw} \approx 2.5$, the C symmetry is broken and the transition into the intermediate S phase occurs. Since the spheres have relatively high mobility in the swelled PS matrix, they rapidly re-arrange in the ordered BCC lattice with the (111) plane parallel to the film surface. The final swelling state with $r_{sw} = 2.75$ corresponds to the state 3. The subsequent fast drying of the film leads to the shrinkage of the formed S structure vertically to the film plane with its transformation to the $C\perp$ morphology through the

coalescence of the *S* microdomains (see Figure 5.9). The in-plane ordering of the *S* structure is preserved upon the fast drying.

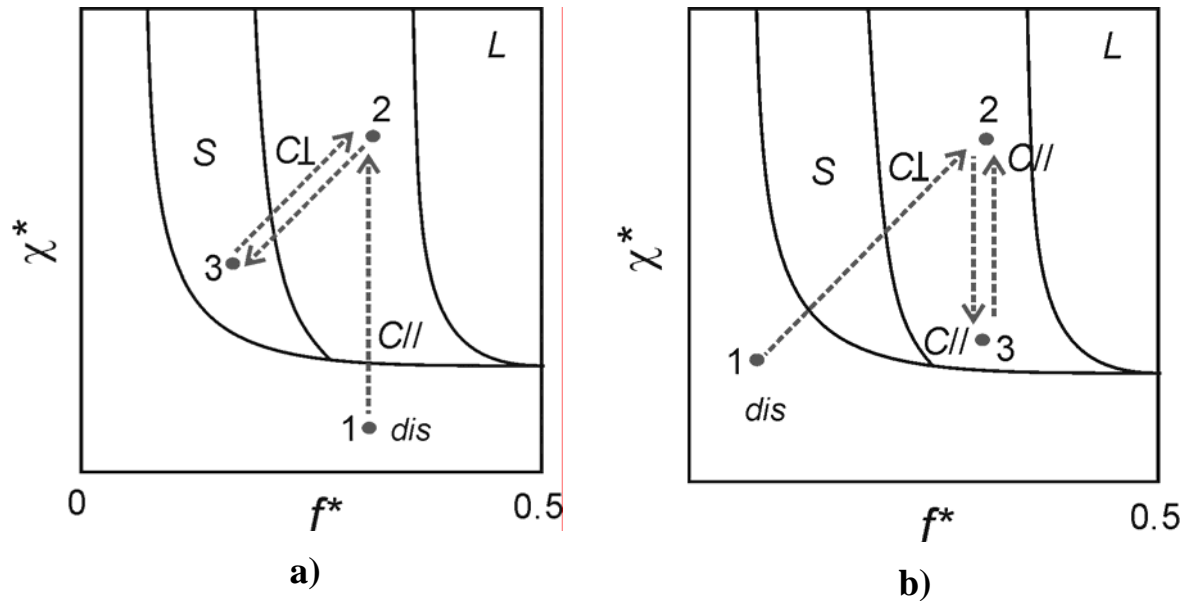


Figure 6.5. Schematic representation of the phase diagram for S36V4+HABA assembly. Vectors show the direction of movement of states for S36V4+HABA film a) deposited from chloroform solution and re-oriented by swelling in 1,4-dioxane vapors and b) deposited from 1,4-dioxane solution and re-oriented by swelling in chloroform vapors on the phase diagram. 1 is the disordered state, 2 is the dry state, 3 is the swollen state.

The assembly film deposited from 1,4-dioxane has the diagonal trajectory 1→2 on the phase diagram (Figure 6.5b), i.e. proceeds from the initial *dis* micellar state 1 to the resulted *C* morphology in the dry state 2 through the intermediate BCC *C* phase. The fast drying results in the perpendicular orientation of the *C* microdomains. Therefore, the perpendicular orientation is metastable and can be easily changed by annealing in vapors of nonselective solvent, i.e. chloroform. Swelling in chloroform corresponds to the vertical trajectory 2→3, which does not change the *C* symmetry of the assembly. At $r_{sw} \approx 2-2.5$, the mobility of the assembly blocks becomes relatively high for their re-arrangement to minimize the total free energy of the system. The film interfaces induce the re-orientation of the *C* microdomains into the in-plane alignment with the simultaneous development of terraces. The AFM image of the film trapped in the intermediate stage of the $C_{\perp} \rightarrow C_{//}$ re-orientation is shown in Figure 6.3. We can see the large number of short cylinders appearing in the image as two interconnected caves. Arising at the very beginning of the re-orientation, they serve as nuclei for the

following growth of the $C//$ microdomains. The growth proceeds in the opposite directions through joining of the adjacent microdomains. We can see that the $C//$ microdomains have different length indicating that nuclei arise non-simultaneously. Initially, the density of the nuclei is relatively low and their orientation is random. As the density of the $C//$ microdomains significantly increases, the newly-arising nuclei are no longer free to orient, hence aligning parallel with respect to the already formed neighboring $C//$ microdomains. At $r_{sw} = 2.75$, we observe the entire re-orientation of the cylinders (see Figure 6.3). However, the resulted $C//$ structure has a poor orientational order and reveals many topological defects. The structural ordering can be considerably improved by allowing the longer swelling duration.

We should emphasize that the system under study is multi-component and it is necessary to take into account many parameters, when the orientation/re-orientation of microdomains is considered. Unfortunately, we know only a little about the role of HABA in the orientation/re-orientation of microdomains. In particular, it is unclear whether there is a connection between the kind of a group (carboxylic or phenolic) forming hydrogen bonds with the nitrogen of pyridine and the microdomain orientation. Can unbound HABA molecules accumulating at the substrate interface reduce the interfacial energy and, hence, assist the perpendicular alignment?

Chapter 7. Study of PS-*b*-P4VP+PDP assembly in thin films

*In this Chapter we demonstrate influence of chemical nature of an additive on PS-*b*-P4VP morphology in thin films. As an additive we used 3-*n*-pentadecylphenol (PDP). This is a good choice for several reasons. The PS-*b*-P4VP+PDP assembly was recently studied in detail by O. Ikkala *et al.* in bulk (description and references are given in Chapter 1). Unlike HABA, PDP is a surfactant and its molecules have only one group capable to form hydrogen bonds.*

The S36V4+PDP films deposited on the top of various substrates had the thickness ranged from 10 to 100 nm, as determined by ellipsometry and an AFM scratch test. The visualization of the film surface with AFM showed that the unwashed films are smooth and featureless with the rms roughness of about 0.3 nm for $1 \times 1 \mu\text{m}^2$ lateral scale. We rinsed the films in methanol to extract selectively PDP. Unlike S36V4+HABA, the washed films revealed no microdomain structure. We observed only a slight rise of the film roughness. The following solvent vapor annealing had no effect on a film structure. We swelled the films in vapors of toluene, chloroform or 1,4-dioxane to the swelling ratios of 2.5–3 and observed no noticeable changes, as compared to the “as deposited” films.

The ellipsometric and AFM scratch measurements showed the appreciable decrease of the “as deposited” film thickness after the rinsing procedure by 15–16%. These results give evidence that the great part of PDP molecules was not hydrogen bonded to the P4VP block in solution. Thus, after the film deposition, “free” PDP escaped in a separate phase. As a surfactant, it probably accumulated at the air interface. We assume that the dimerization of PDP molecules in solution is the main reason for the low effectiveness of assembling between the P4VP block and PDP. *Prima facie*, this is in a contradiction with the results of infrared spectra measurements reported by O. Ikkala *et al.* [Ruo99] They showed that most of PDP molecules are hydrogen bonded to the P4VP block in bulk at the temperatures $<150^\circ \text{C}$. However, we should emphasize that the infrared spectra were obtained for *bulk samples*, where PDP could not easily escape at the interfaces, and *after the temperature annealing*, when the PDP dimers were dissociated and the stronger hydrogen bonds between the P4VP block and PDP were formed.

Contrary, we observed the formation of a surface structure after the temperature annealing of the “as deposited” films. Following O. Ikkala *et al.* [Ruo99], we annealed the film at the temperature of 120°C . The large scale AFM images showed no terracing of the

film surface after the annealing. After the rinsing procedure, we observed variety of surface structures depending on the film thickness. However, we found that these structures were independent on the chemical composition of substrate. As substrates, we used Si wafers as well as Si wafers modified with a silane (GPS) monolayer, random and binary PS-PVP brushes of different composition. We discriminated three thickness regions having the characteristic surface structures: 1) $d < 15$ nm; 2) $d = 15\text{--}30$ nm; 3) $d > 30$ nm.

1) The surface of the thinnest studied films ($d < 15$ nm) was featureless after the rinsing procedure.

2) The surface of the films with $d = 15\text{--}30$ nm revealed the microdomain structure consisted of the close packed round caves of ~ 8 nm in the diameter. The representative AFM image of the film pattern after four days of annealing is shown in Figure 7.1. The mean spacing between the caves from PSD plot is 21–22 nm. We should note the similarity in appearance between the annealed S36V4+PDP and “as deposited” S36V4+HABA films (see Figure 4.1). The film shows no long-range ordering, as it is apparent from a “halo” in 2D FFT plot (see the inset in Figure 7.1). We found no further improving of the film order with the increase of the annealing time.

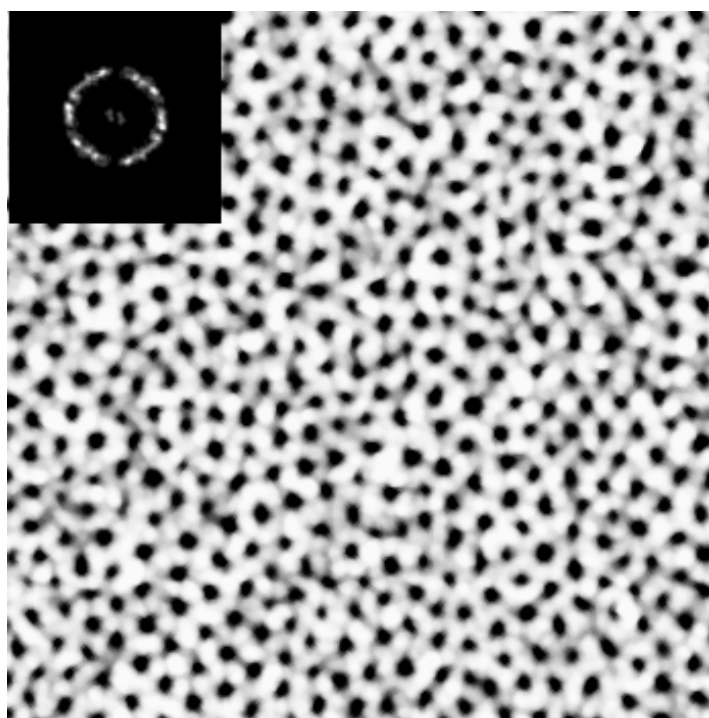


Figure 7.1. AFM image with corresponding FFT of 29 nm thick S36V4+PDP film annealed at 120° C for 4 days and rinsed in methanol, lateral scale 500×500 nm².

We also characterized the film structure with GISAXS. The horizontal profiles of 2D scattered intensity distribution plot of the annealed film ($d=27$ nm) before and after the rinsing procedure is shown in Figure 7.2. We can see that the unwashed film shows no out-of-plane peaks expected from the hexagonal pattern observed with AFM. This is explained by the low contrast between PS and PVP+PDP microdomains. [Mäk2001] However, the extraction of PDP from the film introduces the contrast necessary to visualize the structure. We see the single first-order peak at $q_y = 0.0301 \text{ \AA}^{-1}$ appearing due to scattering from the caves. The peak position corresponds to the mean periodicity of the caves of 21 nm, which is in good agreement with the AFM data. We should note the relatively small intensity of the peak indicating that the caves visible with AFM (see Figure 7.1) have the limited penetration depth.

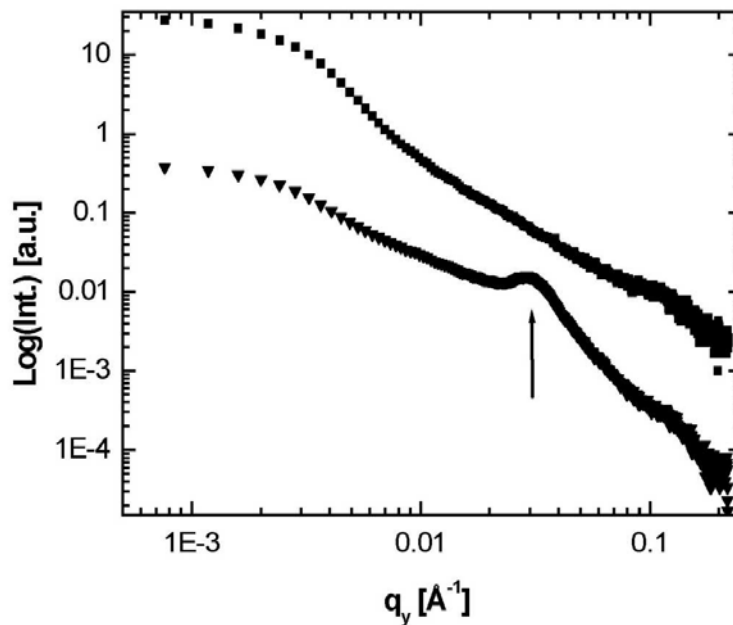


Figure 7.2. Horizontal profiles of 2D scattered intensity distribution plot of 27 nm thick S36V4+PDP film annealed at 120° C for 4 days before (squares) and after (triangles) rinsing with methanol. The curves are shifted for clarity. The array shows the out-of-plane peak position. The measurements were performed at the beamline A2. The angle of incidence $\alpha_i = 1.20^\circ$.

It remains unclear whether the caves are formed by the S or $C\perp$ microdomains. To clarify this, we performed the oxygen plasma etching of the 29 nm thick annealed film at the different depths to explore the internal film structure. The investigation of a structure by successive etching and imaging of BC films was firstly reported by C. Harrison *et al.* [Har98b] After successive local etching of the film, we obtained three regions with the residual thicknesses of 23, 15 and 6 nm. Figure. 7.3 shows the results of the AFM

visualization of the etched regions after the rinsing procedure. The caves are clearly seen in the etched regions with the residual thicknesses of 23 and 15 nm, while they completely disappear in the 6 nm thick region. That shows that the P4VP+PDP microdomains penetrate at least 15 nm in the film depth. Therefore, we believe that the hexagonal structure obtained on the film surface is formed by the short vertical standing cylinders.

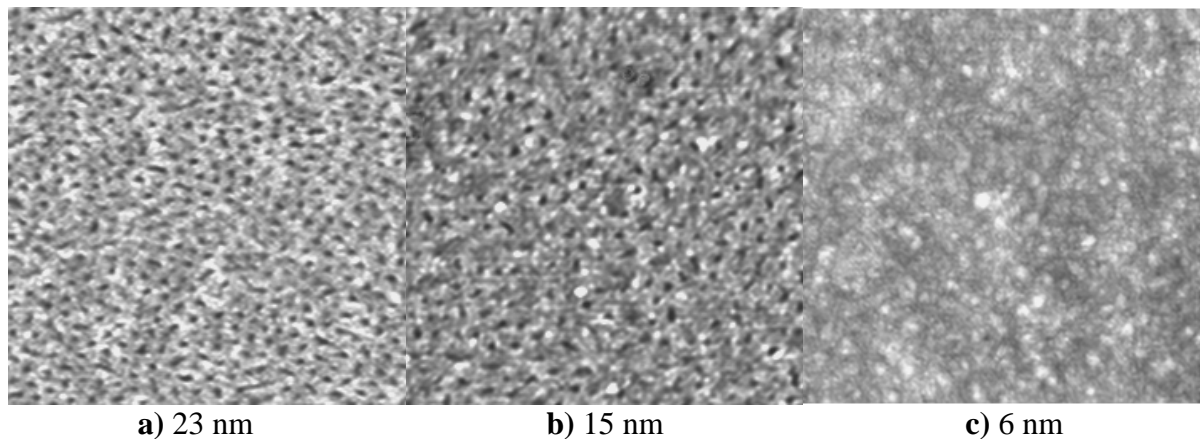


Figure 7.3. AFM images of 29 nm thick S36V4+PDP film etched at the different depths and rinsed in methanol, lateral scale $500 \times 500 \text{ nm}^2$. The values below the images show the residual thickness.

3) The representative AFM image of the surface in the films with $d > 30 \text{ nm}$ is presented in Figure 7.4. The film surface reveals the round caves of the different size scattered over the surface. 2D FFT plot (see the inset in Figure 7.4) exhibits the decaying intensity distribution with the hardly distinguishable broad peak reflecting the broad distribution of the dominating lengths. However, the detail examination of the AFM image shows that the closest caves have the spacing of $\sim 22 \text{ nm}$. Therefore, the apparently random pattern from the caves is explained by the absence of the large number of the regular feature elements. The cave fraction varied with the film thickness being minimal for $d \approx (n+1/2) \cdot L_0$, where $L_0 = 22 \text{ nm}$ is the smallest observed distance between the caves and $n = 1, 2, 3, \dots$

The in-plane microdomain structure of the annealed films was also characterized with GISAXS. Unlike AFM which visualizes the surface topography, GISAXS is sensitive to structures buried in the film depth. Figure 7.5 shows the horizontal profile of the 2D scattered intensity distribution plot of the 91 nm thick film (deposited on Si wafer with a layer of binary PS-P2VP (70:30) brush) after the rinsing procedure. Two low-intensity peaks can be seen in the profile. We fitted the curve with the Gaussian distribution functions to determine the exact

positions of the peaks. The first peak was found at $q_y \cong 0.028 \text{ \AA}^{-1}$, which corresponds to the periodicity of 22 nm. This clearly shows that the microdomain structure is hidden under the film surface and, hence, is not visible with AFM. The weak scattering from this structure gives evidence of the low porosity of the film. The second peak at $q_y \cong 0.015 \text{ \AA}^{-1}$ can be attributed to the in-plane structure formed due to the phase separation in the underlying PS-P2VP brush. [Min2002] The peak position corresponds to the structure periodicity of 42 nm.

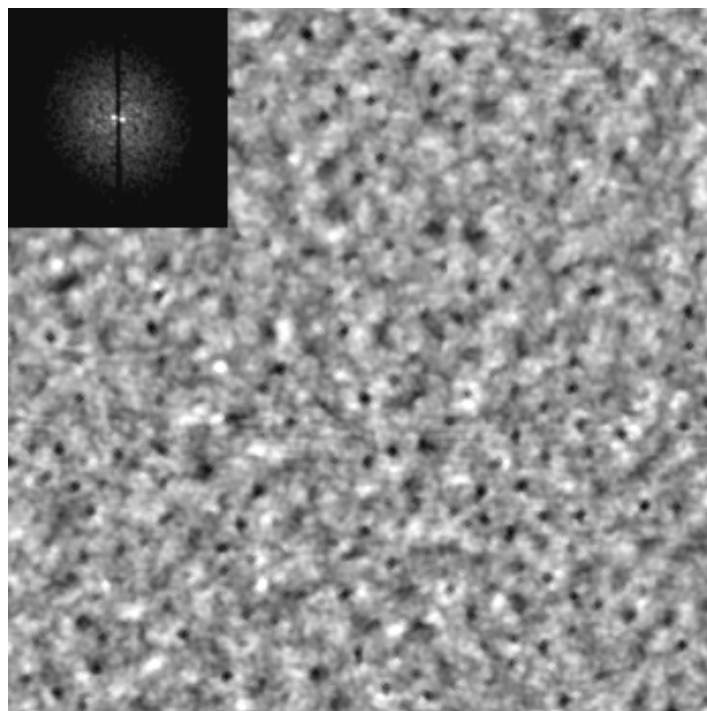


Figure 7.4. AFM image with corresponding FFT of 70 nm thick S36V4+PDP film annealed at 120° C for 5 days and rinsed in methanol, lateral scale 500×500 nm².

The ellipsometric measurements of the films showed the appreciable decrease of the film thickness after the temperature annealing. In particular, the film thickness decreased by ~15% after 8 h and only slightly reduced with the further annealing. It is worth to note the similar drop in the thickness of the “as deposited” films after the rinsing procedure, which was explained by washing out of the unbound PDP molecules forming a layer at the air interface. Therefore, we attribute the change in the thickness during annealing to the rapid sublimation of the unbound PDP molecules from the film surface. Assuming the equimolar composition of “as deposited” films, we can estimate the residual amount of PDP in the annealed films. The drop in the thickness of 16% shows that ~ 75% PDP sublimates during the annealing. Since the remaining 25% PDP molecules were strongly bounded to the P4VP

block, they withstood the annealing procedure. Indeed, the following rinsing of the films with methanol did not change the film thickness but led to the small reduction of the refractive index.

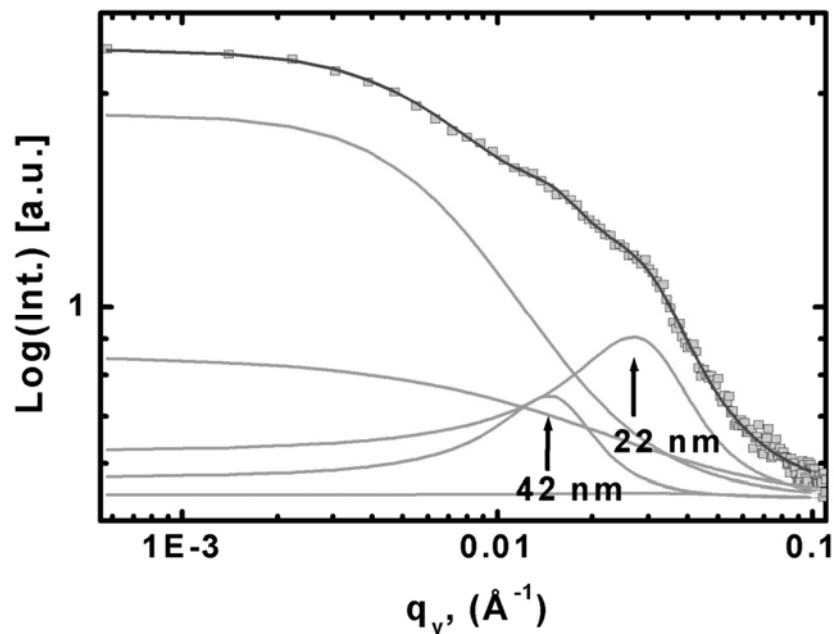


Figure 7.5. Horizontal profile ($\Phi = 0.562^\circ$) of 2D scattered intensity distribution plot of the 91 nm thick S36V4+PDP film annealed at 120°C for 4 days after rinsing with methanol. The arrows show the out-of-plane peak positions obtained from the Gaussian fit of the curve. The measurements were performed at the beamline BW4. The angle of incidence $a_i = 1.20^\circ$.

To explore the internal structure we performed plasma etching of the 70 nm thick annealed film. After the successive local etching, we produced 25 regions with the stepwise increasing of the etch depth (the etch step was ~ 3 nm). Then, the etched film was rinsed with methanol and the regions with the different etch depth were characterized with AFM. The scheme in Figure 7.6 shows that optimizing the etching step, we can easily distinguish between the different morphologies, for example the S and $C\perp$ morphologies and the $C//$ and $L\perp$ morphologies. The AFM images of the regions of the different etch depth are shown in Figure 7.7 (not all the images are presented). The image (a) corresponds to the initial film surface. Removal of the 6.5 nm thick layer from the top of the film reveals the microdomain pattern (c) consisted of holes and grooves of the different length. The mean periodicity of the pattern (PSD plot) is 26 nm. Such a pattern is also clearly observed on the images (h) and (m), which correspond to the thicknesses of the etched regions of 43.2 and 21.6 nm, respectively. On the images corresponding to the intermediate thicknesses, it appears hazy or vanishes

completely. In accordance with Figure 7.6, we attribute the observed patterns to a structure formed by *C*// and *S* microdomains. Figure 7.8 represents schematically the cross-section of the studied film. The P4VP+PDP microdomains form three isolated layers with the interlayer spacing of ~ 22 nm. The interlayer spacing and the mean periodicity of the microdomains (26 nm) relate as $1:\sqrt{3}/2$ characteristic for a hexagonal order. The first layer of the P4VP+PDP microdomains is separated from substrate by a disordered layer typical for *C*// and *S* morphologies.

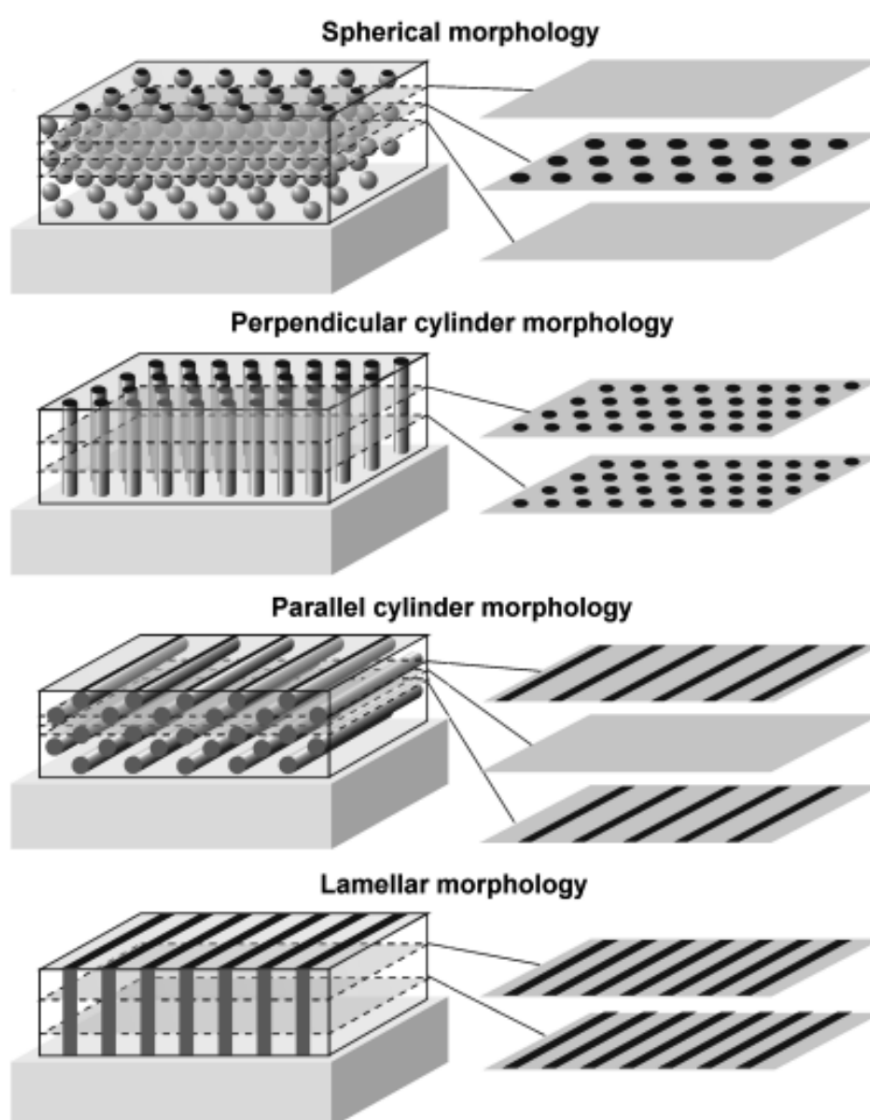
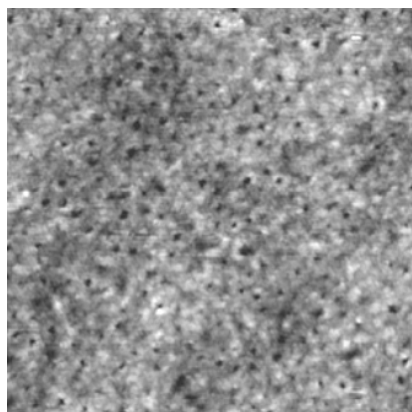


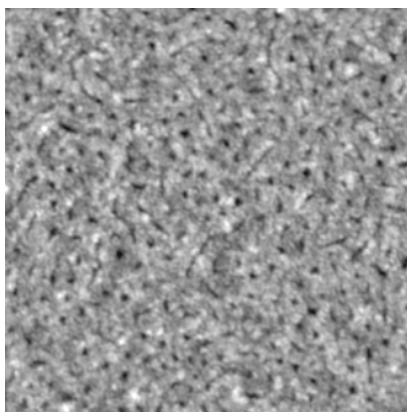
Figure 7.6. Recognition of film morphologies by step-by-step etching and imaging of the etched regions.

The co-existence of the *S* and *C*// microdomains indicates that the composition of the S36V4+PDP assembly films corresponds to the boundary between the *S* and *C* morphologies.

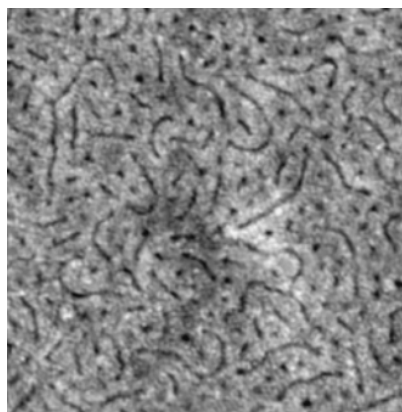
We evaluated the volume fraction of the P4VP+PDP microdomains taking into account that only 25 % of HABA added is H-bonded with the P4VP block. The obtained value (15%) is consistent with the *S/C* phase boundary reported by O. Ikkala *et al.* for PS-*b*-P4VP+PDP assembly in bulk. [Rou99]



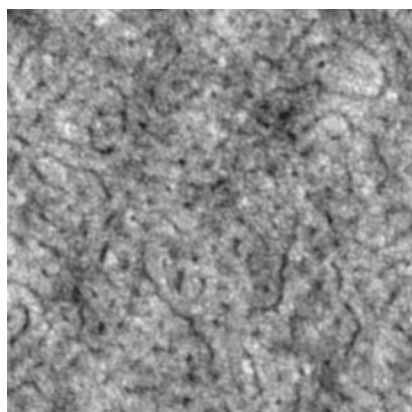
a) 69.8 nm



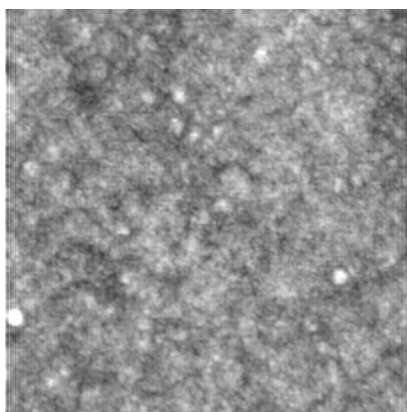
b) 66.5 nm



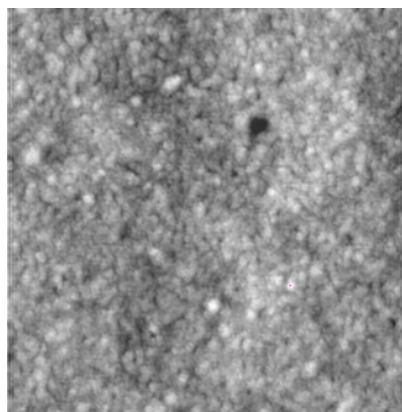
c) 63.4 nm



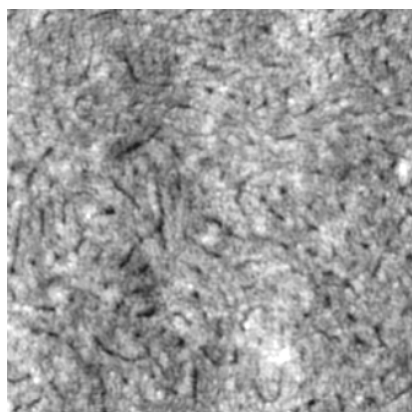
d) 60.1 nm



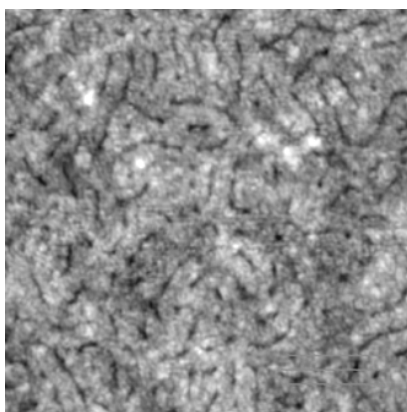
e) 57.2 nm



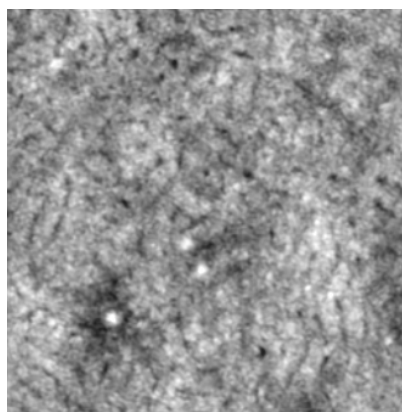
f) 48.5 nm



g) 46.5 nm



h) 43.2 nm



i) 39.8 nm

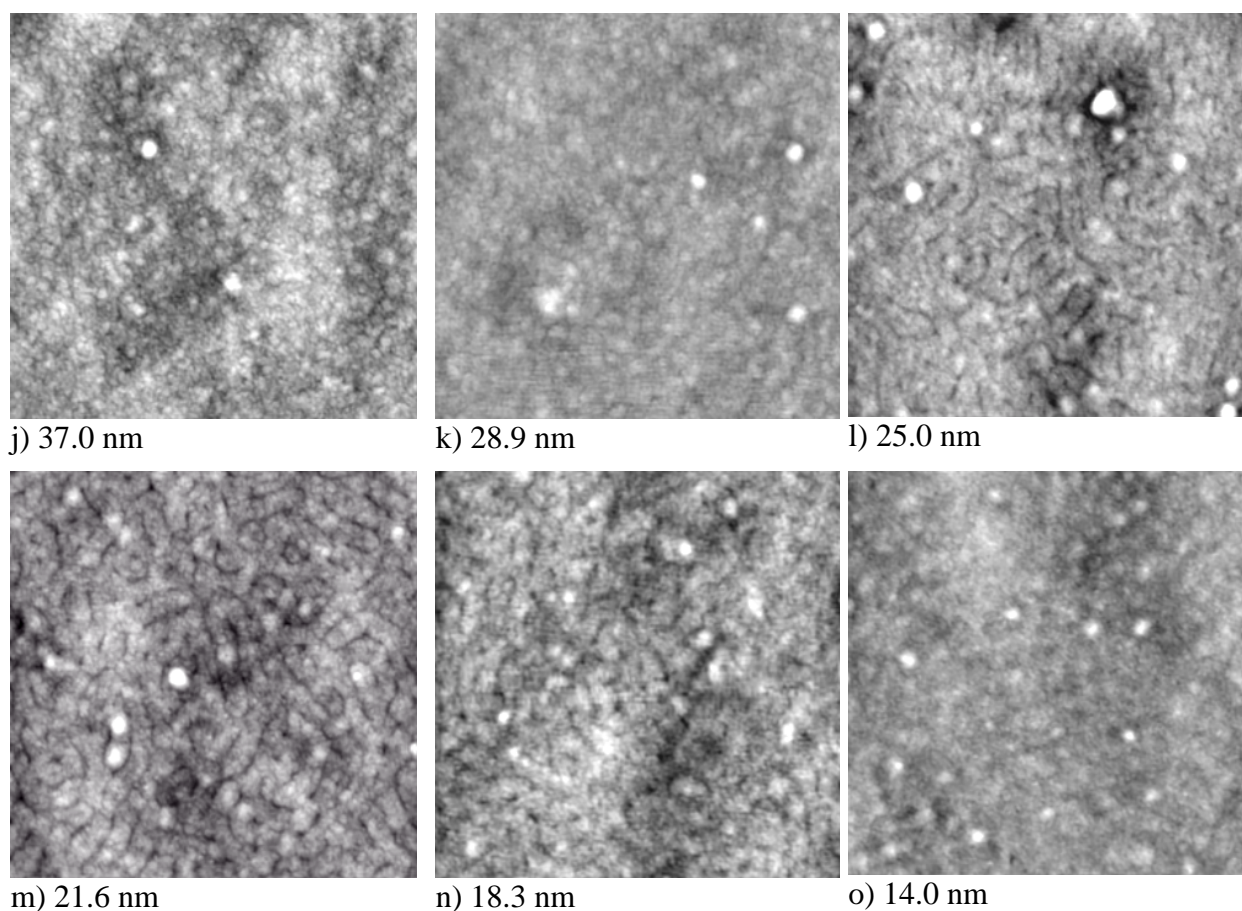


Figure 7.7. AFM images of 70 nm thick S36V4+PDP film etched at the different depths and rinsed in methanol, lateral scale $500 \times 500 \text{ nm}^2$. The values below the images show the residual thickness.

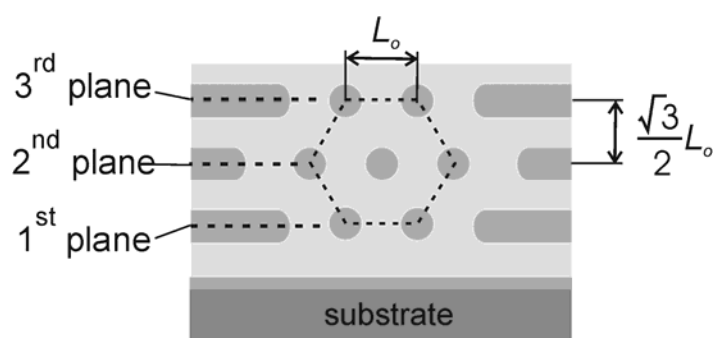


Figure 7.8. Schematic representation of cross-section of 70 nm thick S36V4+PDP film with three planes of *S* and *C*// microdomains.

Chapter 8. Applications of templates from PS-*b*-P4VP+additive assembly films

*In this Chapter we give some examples of the application of the thin films of PS-*b*-P4VP+additive assembly as a template for the transfer of the patterns on the substrate and for the deposition of various materials into the template. The main advantage of our approach is that the template fabrication is very simple and does not require external stimuli to obtain the preferable perpendicular orientation of microdomains. The high ordering of the template can be achieved within minutes by solvent vapor annealing. The porous template is easily produced by washing out of an additive from the microdomains. Furthermore, the pore walls are formed by the reactive P4VP brush which can be used for chemical synthesis of nanoparticles in the template pores.*

8.1. Pattern transfer

Microdomain patterns of BCs in thin films can be transferred into underlying substrates by plasma etching. [Par97] For this, the microdomain-forming blocks must show the sufficiently high difference in etch rates.[Che2001] Alternatively, a BC pattern must have the significant topographical relief, as shown in the sketch in Figure 8.1. The relief is typically introduced through the selective elimination of one of the microdomain-forming blocks.

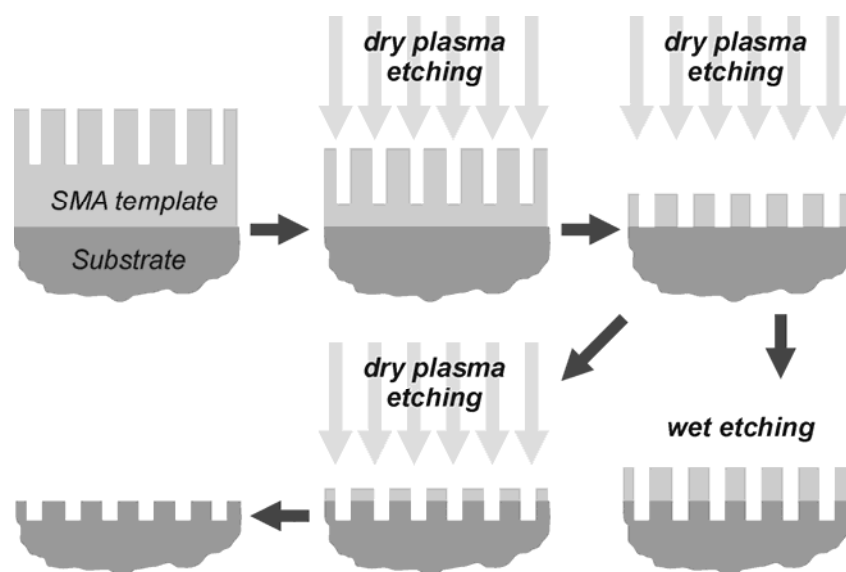


Figure 8.1. Schematic representation of the concept of pattern transfer.

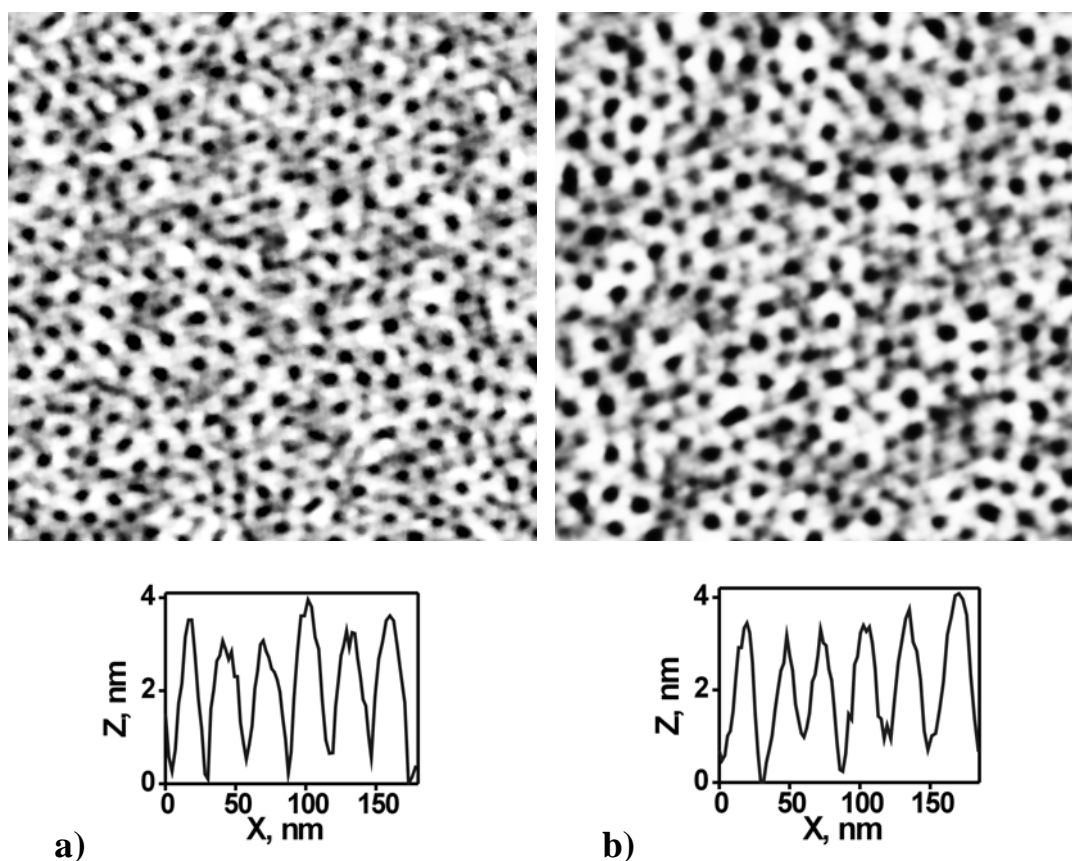


Figure 8.2. AFM images of etched fields of 21 thick S36V4+PDP film annealed at 120 °C for 4 days and rinsed with methanol, lateral scale 500×500 nm². The residual film thickness a) 10 nm and b) 4 nm.

In the PS-*b*-P4VP+additive assembly films, the required topographical relief is easily formed by washing out of a low molar mass additive from the P4VP+additive microdomains. For the experiment, we used the 21 nm thick S36V4+PDP film annealed at 120°C for 4 days. After rinsing with methanol, the film reveals a structure from close packed $C\perp$ channels with the periodicity of 22 nm (see Figure 7.1). As demonstrated in Chapter 7, the channels terminate with the about 10–15 nm thick disordered layer. We applied oxygen plasma etching to transfer the $C\perp$ channel pattern down to Si substrate. After repeated local etching, we obtained two fields with the residual thicknesses of 10 and 4 nm (ellipsometry). The AFM images of the etched fields shown in Figure 8.2 exhibit the characteristic pattern of the film surface. Examination of the images shows that the spacing between the channels is unaffected by the plasma etching, while the channel size visibly enlarges. Assuming the parallel transfer of the pattern, we expect that the channels terminate on Si substrate in the etched field with

the residual thickness of 4 nm. Thus, the porous template can be used as a mask for following dry plasma or wet chemical etching of the substrate.

8.2. Ordered arrays of metal nanoparticles by sputter deposition

A simple route for the fabrication of ordered metal dot arrays is evaporation/sputtering of metals onto a porous template. [Kyu2003] We prepared the ordered porous $C\perp$ and $C//$ templates by solvent vapor annealing of S36V4+HABA films and their following rinsing with methanol. Chromium or gold were then sputtered on the top of the templates.

Sputter deposition of chromium

To study the filling capacity of $C\perp$ templates we sputtered different amounts of chromium at the different locations of a 30 nm thick template. Four fields with Cr amounts of 0.3, 0.85 and 1.70 $\mu\text{g}/\text{cm}^2$ were obtained. We denote them as 1, 2 and 3, respectively. If we assume that deposited chromium forms continuous layers, the values for the Cr amounts above will be equivalent to the layer thicknesses of 4, 12 and 24 nm, respectively. The part of the film surface was left unexposed and used as a reference. We recorded $2p$ Cr NEXAFS spectra of the deposition fields to explore the presence of chromium on the surface. The spectra are presented in Figure 8.3 after the background subtraction. We can see that the Cr

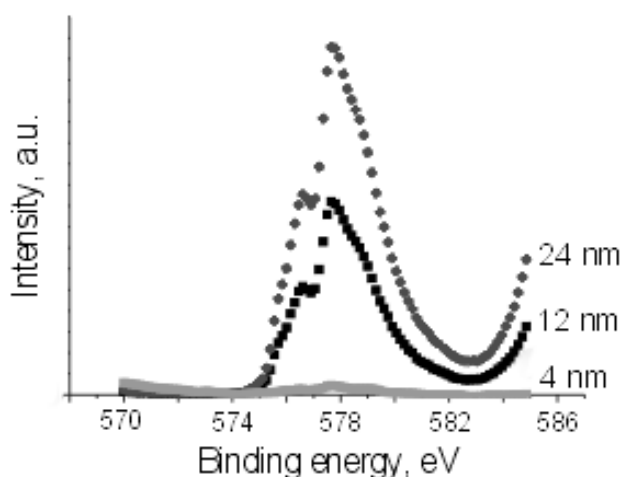


Figure 8.3. $2p$ Cr NEXAFS spectra of the different Cr deposition fields on 30 nm thick $C\perp$ template (S36V4+HABA).

peak intensity in the deposition field 1 is very low as compared to the deposition fields 2 and 3. Taking in account that for polymers the NEXAFS sampling depth is $\sim 5\text{--}10$ nm, we can

conclude that almost all chromium is buried into the template channels in the deposition field 1. At the higher deposited amounts, chromium fills the channels and accumulates on the template surface. The boundaries between the deposition fields were visualized with XPEEM. The result of subtraction of the XPEEM image before the $2p$ Cr peak (573 eV) from that at the peak position (577.6 eV) is demonstrated in Figure 8.4. Afterwards, the former image was subtracted from the latter. The deposition field 1 appears dark in the image, which corresponds to the low Cr signal.

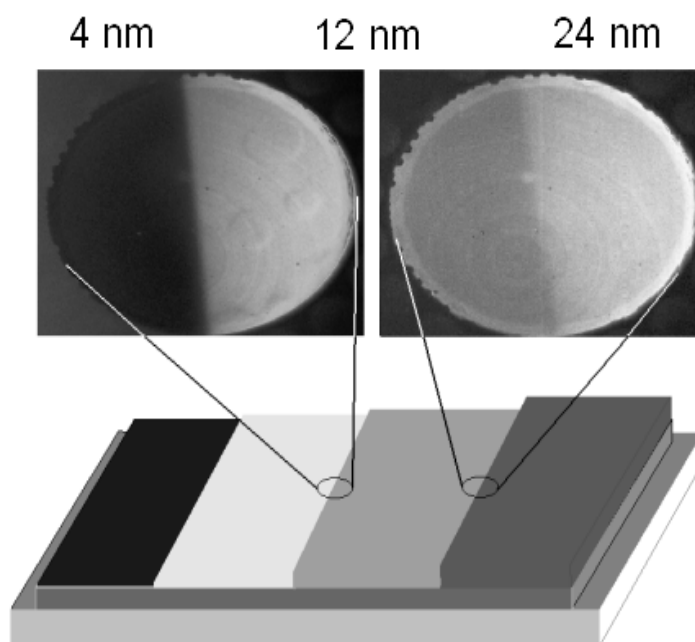


Figure 8.4. XPEEM images of the boundaries between the fields with different deposited Cr amounts, observation field size $120 \mu\text{m}^2$.

We visualized the surface of the different deposition fields with AFM. In agreement with the NEXAFS measurements, we found no Cr clusters in the deposition field 1. However, the Cr excess is seen on the surface of the deposition fields 2 and 3. The representative AFM image of the fields 2 and 3 and the $200 \times 200 \text{ nm}^2$ zoom are shown in Figure 8.5. As one can see chromium in excess is deposited on the PS partition-wall between channels and forms clusters of nanometer size. The clusters “decorate” the channels preserving the initial template order.

Further evidence of the filling of the $C\perp$ template channels with chromium comes from X-ray measurements. We sputtered about $0.6 \mu\text{g}/\text{cm}^2$ ($\approx 8 \text{ nm}$) of chromium onto the $\sim 30 \text{ nm}$ thick S36V4+HABA template and characterized the in-plane distribution of Cr clusters

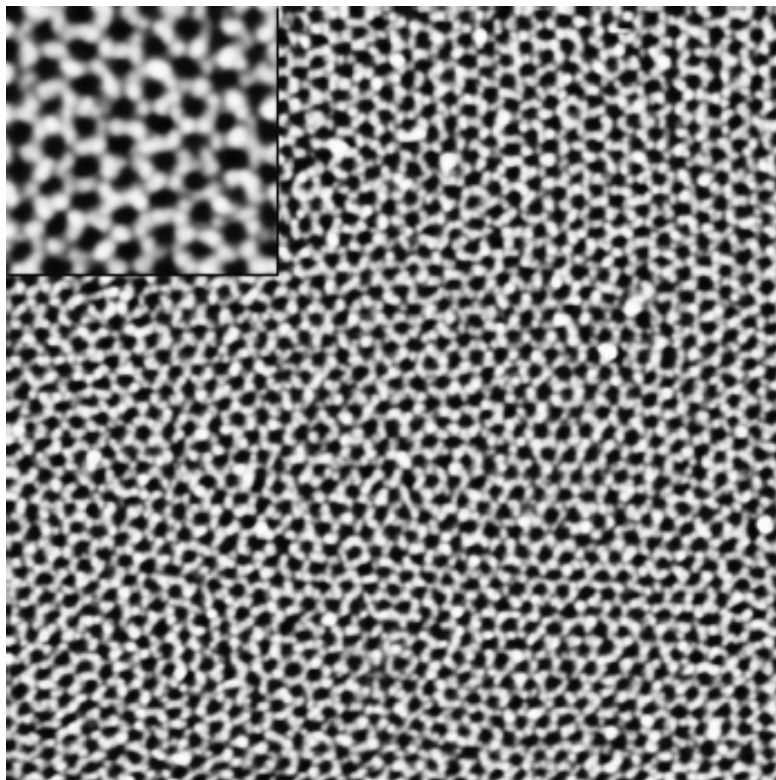


Figure 8.5. AFM image of 30 nm thick $C\perp$ S36V4+HABA template decorated with Cr clusters, lateral scale $1\times 1\ \mu\text{m}^2$ ($200\times 200\ \text{nm}^2$ zoom in inset).

into the channels with GISAXS. The vertical profiles of the 2D scattered intensity distribution plots prior to and after Cr sputtering are shown in Figure 8.6a. We can see the Yoneda peaks of Si and the PS-b-P4VP template in the vertical profile obtained prior to sputtering. After sputtering, these peaks are masked with the stronger Yoneda peak at $\Phi = 1.57^\circ$, which is attributed to the sputtered chromium. The electron density calculated from the Yoneda peak position is $17\cdot 10^{-6}\ \text{\AA}^{-2}$, *i.e.* is about one fourth of the value expected for a continuous Cr layer.

The horizontal profiles of the 2D scattered intensity distribution plots are presented in Figure 8.6b. The Cr deposition does not affect the character of out-of-plane scattering increasing considerably only the overall scattered intensity. This gives the strong evidence that the Cr clusters are located into the template channels. After Cr sputtering, we can even see the third-order ($\sqrt{7}$) peak appearing in the profile as a small shoulder.

To obtain the information on the vertical distribution of the Cr clusters into the template channels, we measured the X-ray reflectivity curve of the sample. It is shown in Figure 8.7 together with the fit and the corresponding depth profile of the electron density.

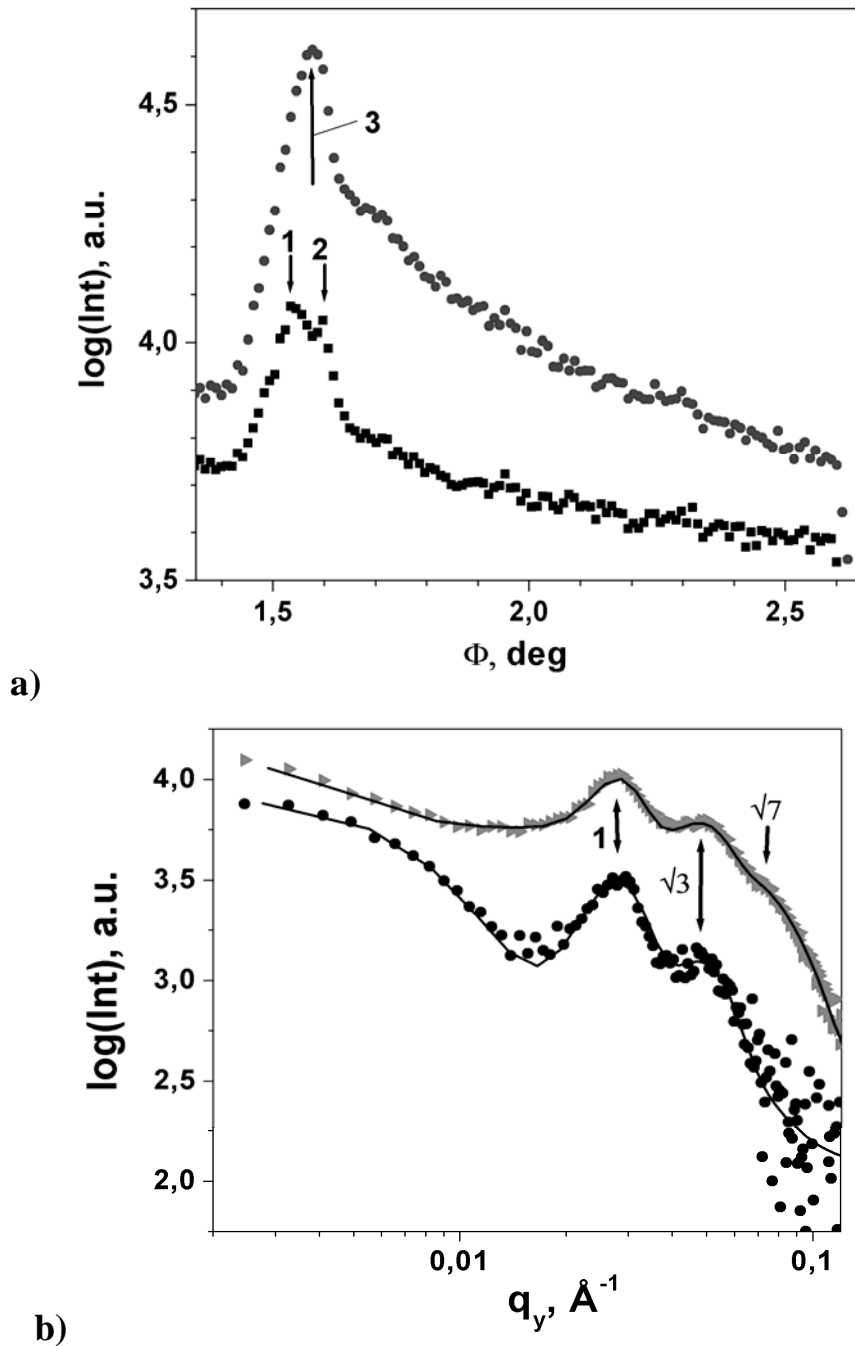


Figure 8.6. Vertical (a) and horizontal (b) profiles of 2D scattered intensity distribution plot of 30–32 nm thick $C\perp$ S36V4+HABA template before (black) and after (gray) Cr sputtering. The curves are shifted for clarity. The solid lines are the Gaussian fits of the horizontal profiles. The arrows in the vertical profiles show the Yoneda peak positions of Si (1), template (2) and Cr clusters into the template channels (3). The arrows in the horizontal profiles show the out-of-plane peak positions. The measurements were performed at the beamline BW4. The angle of incidence $a_i = 1.395^\circ$.

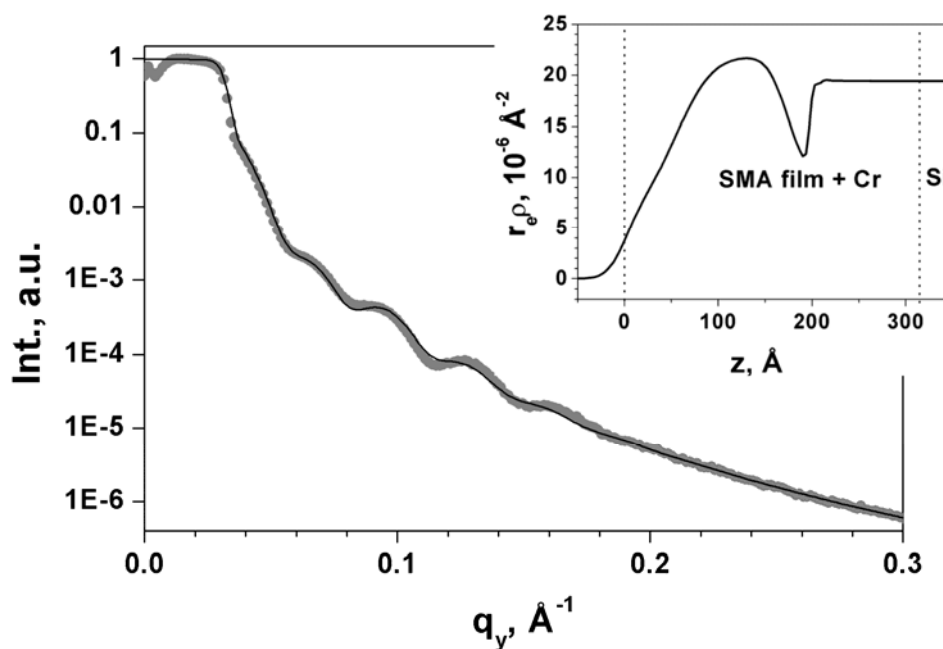


Figure 8.7. X-ray reflectivity curve with fit (solid line) and corresponding depth profile of the electron density (in inset) of 30–32 nm thick $C\perp$ S36V4+HABA template after chromium sputtering.

One can distinguish two regions, where the electron density is high as compared to that of the template before sputtering, which gives evidence of filling of the template channels with chromium. The first region adjacent to the Si substrate has the electron density close to silicon ($19.5 \cdot 10^{-6} \text{ \AA}^{-2}$). As a result, the template/substrate interface is invisible for X-rays. The thickness of the first region is 11 nm. The second region of the comparable electron density and thickness is centered at the distance of ~ 18 nm from the substrate. The depth profile can be explained by assuming that each pore of the template is filled with two individual Cr clusters of ~ 10 nm in size. The first layer of such clusters is formed directly on the Si substrate. It is worth noting that no chromium is present on the template surface. This can be also concluded from the AFM measurements.

An additional evidence for this model comes from the AFM scratch test. We made a scratch of the template and found that its depth was about 21 nm, while the initial template thickness was 30–32 nm. It shows that the first layer of Cr clusters withstood the scratching, what is explained by good adhesion of chromium to the Si substrate and the higher hardness of chromium as compared to a steel needle used to make the scratch.

For the next experiment we used the 33 nm thick $C//$ template with the regular skin-deep grooves. We sputtered $0.11 \mu\text{g}/\text{cm}^2$ ($\equiv 1.5$ nm) of chromium on the template and characterized the cluster distribution with GISAXS. The horizontal profiles of the 2D scattered intensity distribution plots prior to and after Cr sputtering are shown in Figure 8.8.

Cr deposition leads to the appreciable raise of the intensity of the first-order peak, which gives evidence of decoration of the grooves with Cr clusters. We can also see the low-intensity second-order peak. The peak positions determined from the Gaussian fit relate as 1:2, what is characteristic of a striped pattern.

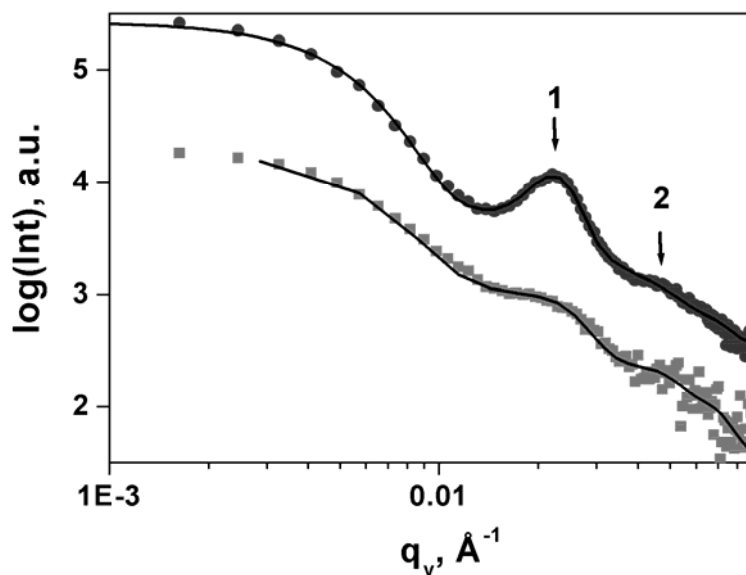


Figure 8.8. Horizontal profiles ($\Phi = 1.54^\circ$) of 2D scattered intensity distribution plot of 30–35 nm thick C// S36V4+HABA template before (gary) and after (black) Cr sputtering. The curves are shifted for clarity. The arrows show the positions of the out-of-plane peaks. The solid lines are the Gaussian fits of the profiles. The measurements were performed at the beamline BW4. The angle of incidence $a_i = 1.395^\circ$.

The AFM image of the template after sputtering (Figure 8.9) clearly shows few nanometer-size Cr clusters located on the PS stripes. The clusters hidden in the grooves, however, are not visible with AFM, because of the limited penetration depth of an AFM tip. The evidence of filling the grooves with chromium comes from the X-ray reflectivity characterization of the template. The reflectivity curve together with the fit and the corresponding depth profile of the electron density are shown in Figure 8.10. We can discern two steps in the depth profile of the electron density. The top step has the width of ~ 4.5 nm and is obviously attributed to the Cr layer visible in the AFM image of the template. The second step of the electron density arises from the grooves filled with the Cr clusters. We can see that the grooves terminate at the distance of ~ 24 nm from the substrate.

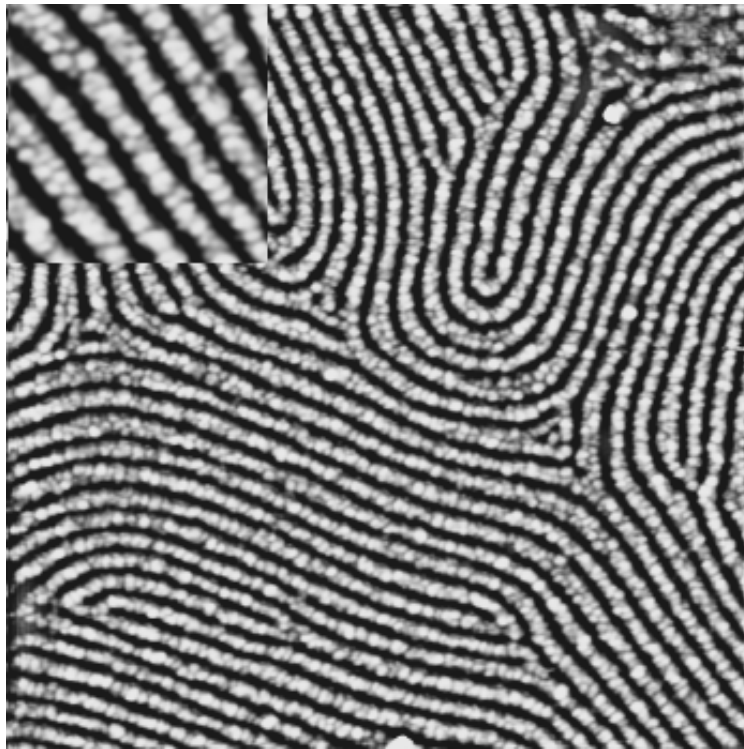


Figure 8.9. AFM image of 33 nm thick C// S36V4+HABA template decorated with chromium clusters, lateral scale $1 \times 1 \mu\text{m}^2$ ($200 \times 200 \text{ nm}^2$ zoom in inset).

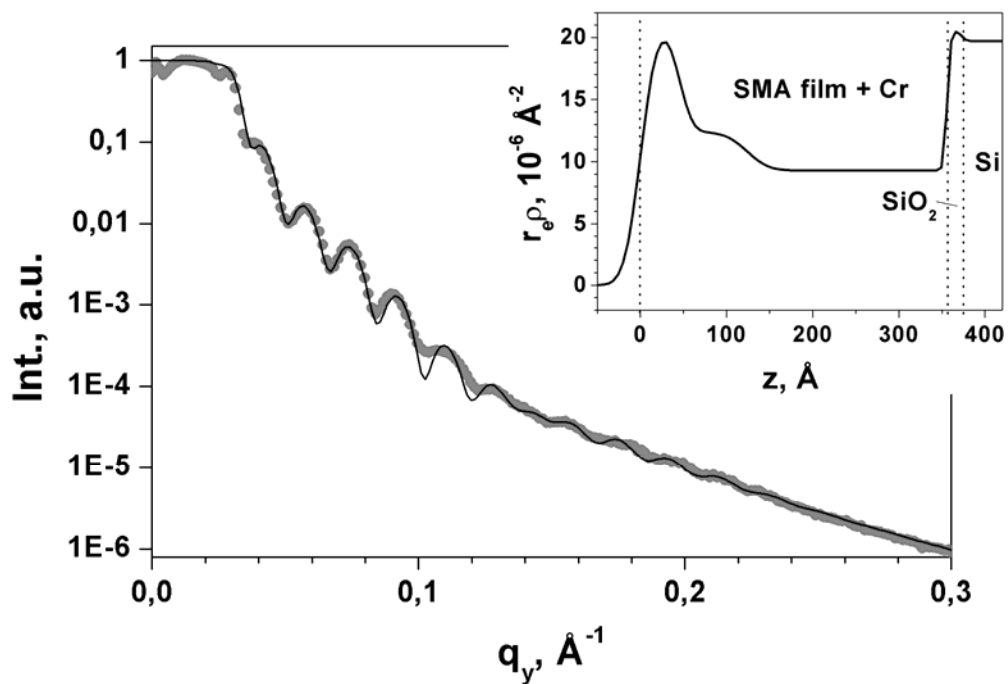


Figure 8.10. X-ray reflectivity curve with fit (solid line) and corresponding depth profile of the electron density (in inset) of 30–35 nm thick C// S36V4+HABA template after Cr sputtering,.

We found out that templates loaded with Cr or Au clusters are resistant to solvents. In particular, the templates prepared on Si wafers remained stable upon storage them in non-selective solvent (chloroform) for several days. Moreover, the pore structure of the templates was preserved as well, as proved with AFM. We suppose that the metal clusters interacting with P4VP brush on the channel walls act as a cross-linking agent providing the templates with resistance to solvents. The template is attached to the substrate surface with a P4VP adsorption layer, which prevents its lift-off.

Sputter deposition of gold

The particular case is the sputter deposition of gold. Unlike chromium, gold is not adherent to silicon oxide. Furthermore, it was shown by K. R. Shull *et al.* [Kun93] that gold particles strongly interact with P2VP. Therefore, we expected the different behavior of Au clusters into the template channels with the P4VP walls. Gold was sputtered onto the 30 nm thick template in the amount of $\sim 0.7 \text{ mg/cm}^2$ ($\equiv 3.5 \text{ nm}$). We performed GISAXS and X-ray reflectivity measurements to characterize the in-plane and vertical Au distributions in the template.

The vertical profiles of the 2D scattered intensity distribution plots prior to and after Au sputtering are shown in Figure 8.11a. We can see that the Au deposition gives rise to the Yoneda peak with the maximum at $\Phi = 1.71^\circ$ and the shoulder noticeably extended towards the lower angles. The peak maximum position corresponds to the electron density of $\sim 57 \cdot 10^{-6} \text{ \AA}^{-2}$, which is of about 44% of the electron density of gold in bulk. The extended shoulder evidences the significant variation of the Au density normal to the substrate.

The horizontal profiles of the 2D scattered intensity distribution are shown in Figure 8.11b. We should note that the overall scattered intensity considerably increases upon the Au deposition. As compared to the uncovered template, the intensity distribution extends to the higher q_y -values, which correspond to the smaller length scales. The presence of the substantial Au amount in the template channels becomes apparent from the intensive out-of-plane peaks.

The reason of the broad vertical and horizontal scattering intensity distributions is found from the X-ray reflectivity measurements of the Au covered template. The reflectivity curve together with the fit and the corresponding depth profile of the electron density are shown in Figure 8.12. The “fringe” pattern reveals superimposed oscillations with two different periods which indicate a two-layer system. We attribute them to the template (small-period oscillations) and a layer of Au clusters on the top (large-period oscillations).

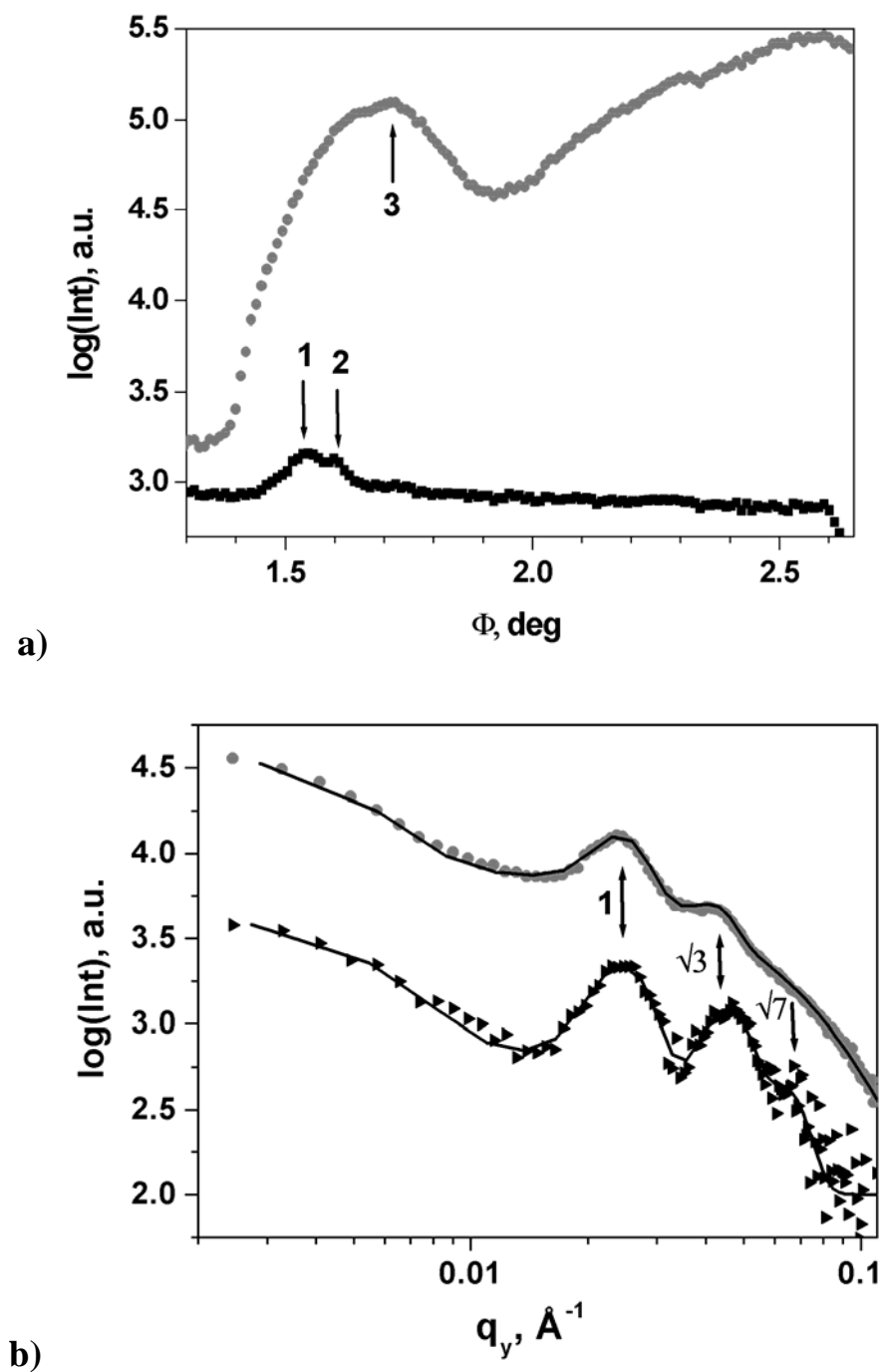


Figure 8.11. Vertical (a) and horizontal (b) profiles of 2D scattered intensity distribution plot of 30 nm thick $C\perp$ S36V4+HABA template before (black) and after (gray) Au sputtering. The curves are shifted for clarity. The solid lines are the Gaussian fits of the horizontal profiles. The arrows in the vertical profiles show the Yoneda peak positions of Si (1), the template (2) and a layer of Au clusters (3). The arrows in the horizontal profiles show the out-of-plane peak positions. The measurements were performed at the beamline BW4. The angle of incidence $\alpha_i = 1.395^\circ$.

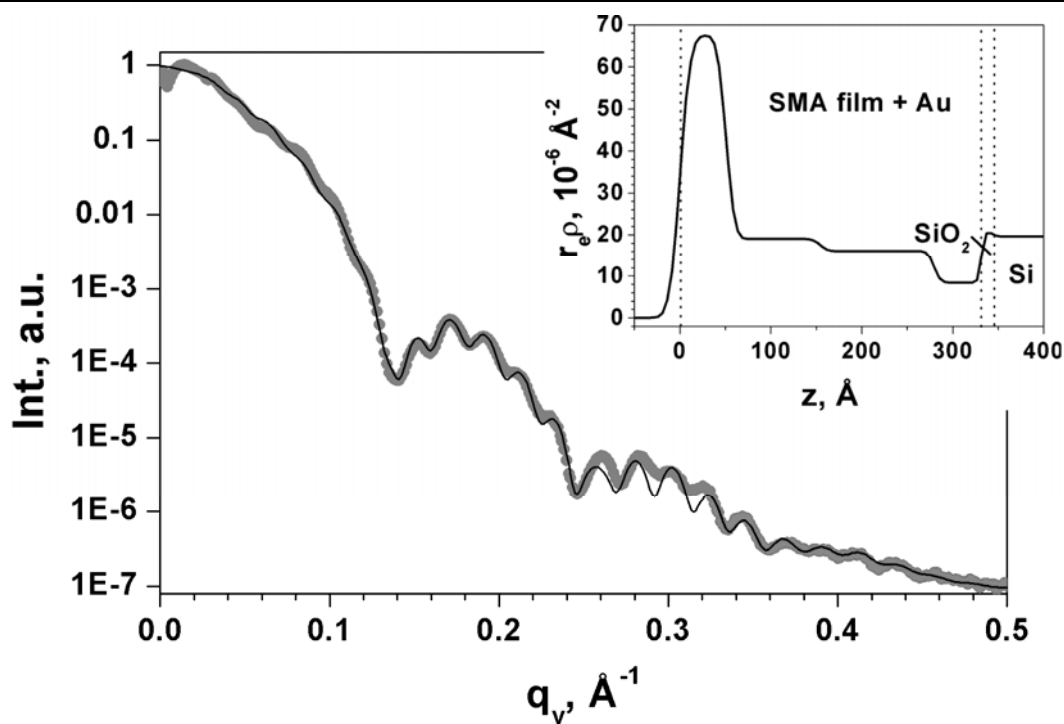


Figure 8.12. X-ray reflectivity curve with fit (solid line) and corresponding depth profile of the electron density (in inset) of 30 nm thick $C\perp$ S36V4+HABA template after gold sputtering.

After Au sputtering the mean electron density of the template significantly increases, which indicates loading the template channels with small Au clusters. We can see small decrease of the density of the Au clusters with depth. The exception is ~ 3 nm thick layer adjacent to Si substrate, which has the electron density of PS. This layer was observed in the depth profiles of the rinsed $C\perp$ S36V4+HABA films (see Figures 4.3 and 5.5) and attributed to the P4VP block adsorbed on the polar Si substrate. The mean electron density of the 5 nm thick layer of Au clusters on the top of the template is similar to found from the Yoneda peak position of the vertical profile (see Figure 8.11a).

The Au layer on the top of the template was visualized with AFM. The AFM image with the $180 \times 180 \text{ nm}^2$ zoom in the inset is shown in Figure 8.13. Similar to chromium, the Au clusters decorate the PS channel walls. The clusters appear larger in size, as a result of the widening effect of an AFM tip.[Ves93]

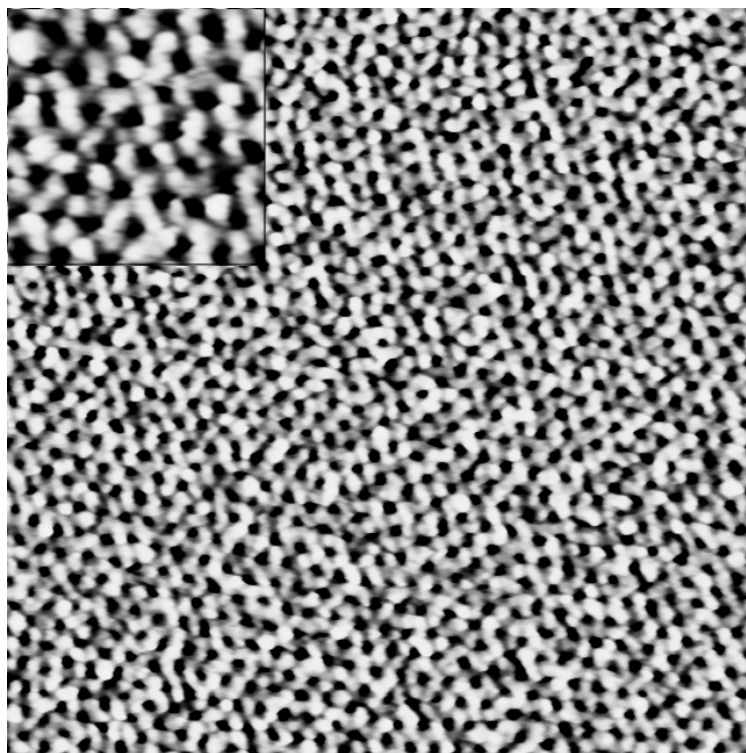
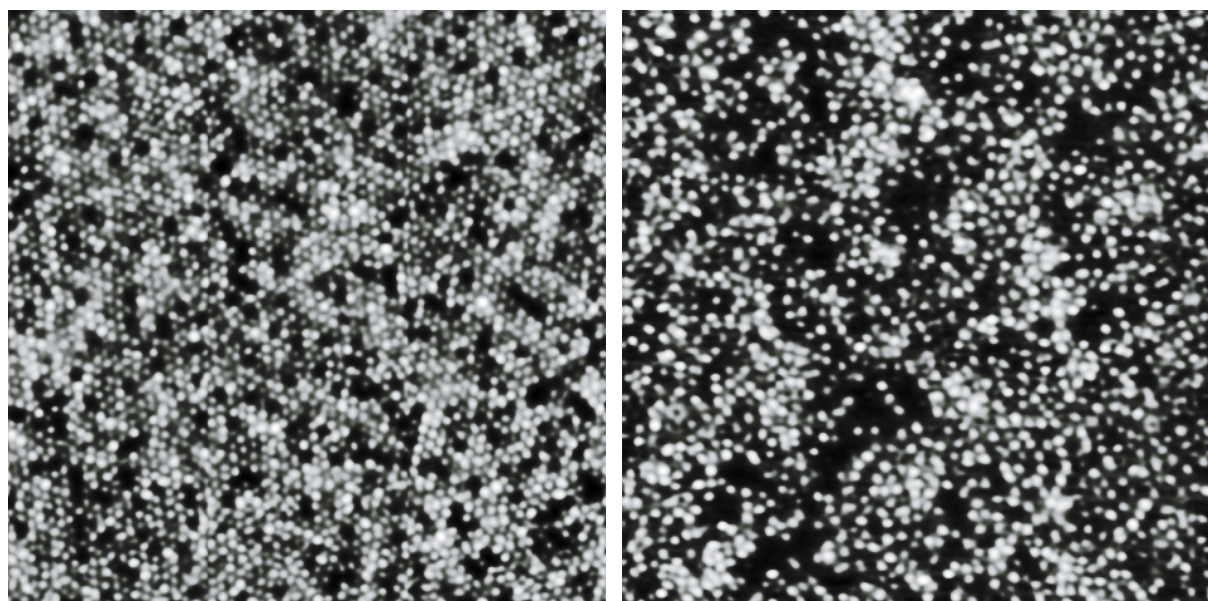


Figure 8.13. AFM image of ordered $C\perp$ template (S36V4+HABA) loaded with Au clusters, 30 nm thick, lateral scale $1\times 1\ \mu\text{m}^2$ ($180\times 180\ \text{nm}^2$ zoom in inset).

8.3. Electrochemical growth of ordered arrays of Ni nanorods

In this section we study aspects of the use of thin polymer templates for electrochemical deposition of metal nanodots/nanowires. We performed the series of experiments with the electrodeposition of Ni through the $C\perp$ S36V4+HABA templates prepared on different electrodes. First, we started with DC electrodeposition on the Ni electrodes covered with a SMA template. We optimized the conditions of electrodeposition in terms of current density and deposition time. Figure 8.14a shows the array of Ni nanorods obtained in galvanostatic regime at $0.3\ \text{mA}/\text{cm}^2$ current density for 1000 sec. The deposition potential reveals only minor changes during the electrodeposition in the range of -0.75V to -0.79V . Hexagonally arranged rods of 10-20 nm high are clearly seen as well as some fraction of lacunas. Analysis of the AFM images shows that the lacuna surface fraction is in the range of 5-20%. At the same time, the hundreds nm – micron size Ni clusters are scattered over the surface. The reason for this is non-simultaneous formation of Ni nucleation sites. We believe that the P4VP adsorption layer may play here a key role. The similar results were obtained on Cr electrodes covered with the $C\perp$ S36V4+HABA template. It is worth to note that increase

of deposition time or current density results in sufficient increase of large size Ni clusters on the top of the template.



a)

b)

Figure 8.14. AFM image of Ni nanorods electrodeposited through ordered $C\perp$ S36V4+HABA templates on a) Ni electrode and b) Si(111) electrode. The polymer template is removed. Lateral scale $1.5\times 1.5\ \mu\text{m}^2$, vertical scale 20 nm.

To study the effect of a barrier layer we performed the Ni electrodeposition through an ordered $C\perp$ template on a Si(111) electrode. The deposition potential varies during deposition on the range from $-1.0\ \text{V}$ to -1.05V at $0.3\ \text{mA}/\text{cm}^2$ current density applied in DC galvanostatic regime. We explain the overpotential increase as compared with the Ni electrode by the presence of the native SiO_2 layer which interferes the electrodeposition in the DC regime. This is the reason why electrodeposition in the DC regime results in a very rough covering consisted of Ni clusters of micron size. Indeed, the nucleation rate is much lower than the growth rate and the overpotential value is higher in the case of the insulating thin layer on the top of the electrode. It results in fast growth of rare clusters and in overload of the separated template channels as described in details elsewhere [Mor2001].

To overcome the effect of insulating SiO_2 layer, we applied a pulsed galvanostatic regime as proposed by Gösele et. al. [Nie2000]. We modified the AC galvanostatic deposition parameters for thin templates and optimized the conditions. The PED was performed at the conditions as given in Table 2.3. (see Section 2.1). The resulting Ni nanostructure on Si(111) is shown on Figure 8.14b. Ni nanodots of 5-20 nm high are clearly seen as well as sufficient

surface lacunas. The estimation of lacuna surface with flooding procedure gives the lacuna fraction on the range of 40÷60%.

The comparison of Ni electrodeposition conditions and morphology of nanostructures obtained on Ni and Si(111) demonstrates the effect of thin insulating layer on the deposition process into thin templates where the nucleation time is a crucial parameter. In order to visualize the found effect, we performed the Ni electrodeposition onto the Cr electrode which was partially covered with a PBd insulating layer forming a micrometer size mosaic pattern. Figure 8.15a shows the large scale AFM image of the 60 nm thick cross-linked PBd. We deposited the 70 nm thick S36V4+ HABA film on the top of the Cr mosaic electrode and converted it into the template rinsing with methanol. Afterwards, we performed the Ni electrodeposition through the ordered $C\perp$ template (S36V4+HABA) in the galvanostatic DC regime and removed the polymer template in nonselective solvent (chloroform). The obtained samples were investigated with AFM and XPEEM. The AFM image is shown in Figure 8.15b. It demonstrates PBd film squares with space between them covered with Ni nanorods. Also, there are several clusters of Ni of micron size and lacunas rarely seen on the Ni covering.

The NEXAFS measurements of Ni deposition were performed prior the XPEEM measurements to find the exact $2p$ Ni bonding energy as well as the peak width. The result of subtraction of XPEEM images before (851.5 eV) and after (854.0 eV) $2p$ Ni peak from the image at the peak (853.0 eV) is shown on the Figure 8.15c. It clearly demonstrates distribution of nickel in the space between the PBd masked electrode surface. Thus, we obtained two-scale hierarchy patterning combining electrode photolithography with insulating layer and nanotemplating.

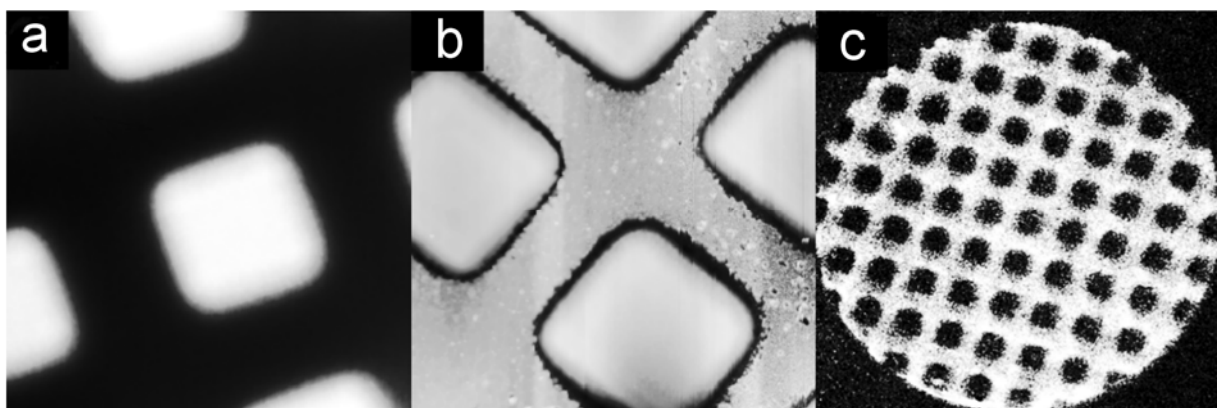


Figure 8.15. AFM images of PBd masked Cr electrode before (a) and after (b) Ni templated deposition, lateral size $25\times 25\ \mu\text{m}^2$, vertical scale 70 nm, and XPEEM image with Ni $2p$ contrast (c), $120\times 120\ \mu\text{m}^2$ lateral scale.

Summary

Self assembly in soft matter is of a great fundamental and practical interest. Novel self-assembled materials are based on competing intermolecular interactions and frequently reveal self-organization over many length scales. Theoretical descriptions of phase behavior and dynamics of such materials require creation of sophisticated theories. In this respect, verification of theoretical predictions with experiment is of essential importance. The ability of block copolymers to self-assemble into ordered periodic structures on nanoscale makes them also promising in many fields of nanoscience and technology.

We investigate thermodynamics and dynamics of microphase separation and ordering in novel supramolecular polymeric materials in thin films. The materials are based on assembly of block copolymers and low-molar mass additives selectively attached to one of the blocks by hydrogen bonds to form a comb-like macromolecule (hereafter block copolymer assembly or, shortly, BCA). We used diblock copolymers, polystyrene-block-poly(4-vinylpyridine), of two different ratios between blocks and similar molar masses. Without additive they demonstrate the following equilibrium morphologies formed by microphase-separated blocks: body-centered cubic (BCC) spherical morphology (the symmetry $\text{Im}\bar{3}\text{m}$) and hexagonal cylindrical morphology (the symmetry p6mm). We used two different low-molar mass additives, 2-(4'-hydroxybenzeneazo)benzoic acid (HABA) and 3-Pentadecyl phenol (PDP).

Selective attachment of low-molar mass additive to one block increases its volume fraction resulting in a change of the symmetry of equilibrium morphology formed by microphase-separated blocks. The symmetry of block copolymers used in this study changes from BCC spherical to hexagonal cylindrical and from hexagonal cylindrical to lamellar when the additives are assembled.

Comparison of theoretically calculated periodicity of microdomains (Semenov's strong segregation approximation) with the bulk periodicity found experimentally suggests that studied copolymer assemblies are in the strong segregation regime ($\chi N \approx 63$). The regime is characterized by considerable stretching of copolymer chains (approximately five times as compared to undisturbed Gaussian gyration radius) and narrow interfaces. The incompatibility of the blocks results in fast dynamics of microphase separation and ordering in BCA.

Properties of low-molar-mass additive and physical nature of bonds tethering it to assembly-forming block are crucial factors which determine the phase behavior of BCA in thin films. Amphiphilic low-molar mass additives are known to have a strong tendency to occupy phase interfaces to minimize the interface tension and hence the free surface energy of a polymer/additive system. In the case of BCA films, unbound amphiphile additive (*e.g.* PDP) phase separates at the free air interface during the film formation. Since this process is undesirable, the non-amphiphilic additives are to be used. Furthermore, the strength of noncovalent interactions between additive and assembly-forming blocks should be sufficiently high to ensure the effective bonding in solvent medium.

The alignment of the cylindrical and lamellar microdomains with respect to the film plane in thin BCA films depends on solvent used for deposition while is insensitive to film thickness and an energetic preference of substrate to either of copolymer blocks. In particular, if the deposition of BCA films with cylindrical morphology is performed from solution of nonselective solvent (*e.g.* chloroform), in-plane aligned cylinders are observed. Meanwhile, BCA films deposited from solution of solvent which is selective to cylinder-forming block (*e.g.* 1,4-dioxane) reveal cylinders aligned normal to the film plane. BCA films with lamellar morphology deposited from solutions of nonselective and selective solvents demonstrate perpendicular alignment of lamellae. This is apparently in contradiction with the theoretical statement that the in-plane alignment of microdomains has the lower total free energy than that with perpendicular orientation, when there is a notable preference of confining interfaces for either of the copolymer blocks. Indeed, the occurrence of both blocks at the film interfaces in the case of the perpendicular orientation results in a substantial penalty to the free surface energy of the system. However, our experiments show that perpendicular oriented cylinders can minimize unfavorable interfacial interactions by segregation of the block having the lower interfacial energy at the air or substrate film interfaces. The formed thin wetting layers assist the perpendicular orientation of microdomains.

Swelling (annealing) of BCA film in solvent vapor brings it to the fluid state allowing the mobility of copolymer segments. Therefore, solvent vapor annealing assists the ordering of microdomains which is accompanied by minimization of the total free energy of the system. On the other hand, solvation of copolymer blocks decreases their incompatibility which controls the dynamics of ordering and the degree of phase separation. Therefore, well-ordered microdomain structures (with respect to orientational and translational orders and microdomain size distribution) are formed within the narrow range of swelling degrees.

Furthermore, the orientation of microdomains with respect to the film plane switches upon annealing of BCA films in vapors of appropriate solvent. In particular, annealing of BCA films with “in-plane” cylinders in vapors of selective solvent results in the switching of their orientation into the perpendicular alignment. *Vice versa*, annealing of BCA films with perpendicular oriented cylinders in vapors of nonselective solvent switches their orientation to the in-plane alignment. The switching of orientation is reversible and fast (tens of minutes).

We believe the selectivity of solvent used for deposition or annealing is a key factor which determines the orientation of microdomains with respect to the substrate plane in BCA films. In the case of BCA films with cylindrical morphology, preferential swelling of BCA matrix in vapor of selective solvent results in the order-order transition (ODT) into spherical morphology. In the swollen state the spheres are able to rapid re-arrangement to form well-ordered BCC lattice with (111) plane coincident with the film plane. Fast drying of the films leads to shrinkage of microdomain structure in the direction along the film normal. Since the re-arrangement of the junctions between blocks necessary to change the in-plane intersphere spacing is a slow process as compared to the rate of solvent evaporation, the in-plane hexagonal order of spheres becomes “frozen”. Thus, upon the film shrinkage the spheres are approaching in the direction along the film normal and, finally, coalesce into perpendicular aligned cylinders. The formed cylindrical structure is non-equilibrium, which is reflected in the reduced intercylinder periodicity. Further swelling of the film matrix results in the order-disorder transition (ODT). In fact, the disordered state corresponds to the concentrated solution of spherical micelles, which is a starting point of formation of films deposited from selective solvent solution. In vapors of nonselective solvent, both blocks swells similar and the cylindrical symmetry of BCA films remains unchanged. Meanwhile, composition fluctuation in the swollen film results in re-orientation of perpendicular cylinders into the more thermodynamically stable in-plane alignment. The vertical shrinkage of the film upon drying leads to significant distortion of the hexagonal lattice which is apparent from the deviation of the in-plane periodicity of the cylinders from the bulk value.

Rinse of BCA films in selective for additive solvent (*i.e.* it should be nonsolvent for block copolymer matrix) extracts it from assembly-forming microdomains. The main requirement is high polarity solvent, since hydrogen bonds between additive and the block are effectively destroyed only in high dielectric constant medium. As a result of rinsing procedure, channels or grooves (depending on BCA symmetry and microdomain orientation) are formed in the copolymer matrix. The volume fraction of pores formed after rinse of films of assembly of

block copolymer and non-amphiphilic additive was close to the volume fraction of additive in BCA.

The rinsed BCA films demonstrating regular patterns from nanoscopic channels or grooves can be further used as membranes and templates for fabrication of nanostructures over large areas. The main advantages of our approach of fabrication of well-ordered nanoporous templates/membranes are that it is simple, fast and thus cheap. It is also compatible with well established techniques of nanofabrication. The pattern of the nanoporous template can be simply transferred in underlying polymer or inorganic substrate by physical or chemical etching. The channels of template can be also filled with various materials as demonstrated on the examples of electrodeposition of magnetic materials and sputter deposition of electroconducting materials. Since the template channels are covered with reactive P4VP brush, it can serve as active sites for chemical synthesis of nanoparticles. The resulted densely packed ordered nanoarrays are promising in a variety of applications, such as quantum dot lasers, single electron devices, high-capacity storage magnetic memory, DNA and protein electrophoresis, catalysts *etc.*

References

- [Abe77] Abe, K.; Koida, M.; Tsuchida, E. *Macromolecules* **1977**, *10*, 1259.
- [Als2001] Als-Nielsen, J.; McMorrow, D. *Elements of Modern X-ray Physics*; John Wiley & Sons: New-York, 2001.
- [Amu91] Amundson, K.; Helfand, E.; Patel, S. S.; Quann, X. *Macromolecules* **1991**, *24*, 6546.
- [Amu94] Amundson, K.; Helfand, E.; Quann, X.; Hudson, S.D.; Smith, S.D. *Macromolecules* **1994**, *27*, 6559.
- [Ana89] Anastasiadis, S. H.; Russell, T. P.; Satja, S. K.; Majkrzak, C. F. *Phys. Rev. Lett.* **1989**, *62*, 1852.
- [Asa2002] Asakawa, K.; Hiraoka, T.; Hieda, H.; Sakurai, M.; Kamata, Y.; Naito, K. *Photopolymer Sci. Techn.* **2002**, *15*, 465.
- [Azz97] Azzam, R. M. A.; Bashara, N. M. *Ellipsometry and Polarized Light*; North-Holland: New York, 1997.
- [Bal89] Balta-Calleja, F. J.; Vonk, C. G. *X-ray Scattering of Synthetic Polymers, Polymer Science Library* 8; Elsevier: Amsterdam, 1989.
- [Bat90] Bates, F. S.; Fredrickson, G. H. *Annu. Rev. Mater. Sci.* **1990**, *41*, 525.
- [Bat94] Bates, F. S.; Schulz, M. F.; Khandpur, A. K.; Förster, S.; Rosedale, J. H.; Almdal, K.; Mortensen, K. *Faraday Discuss. Chem. Soc.* **1994**, *98*, 7.
- [Bla2001] Black, C. T.; Guarini, K. W.; Black, C. T.; Milkove, K. R.; Baker, S. M.; Russell, T. P.; Tuominen, M. T. *Appl. Phys. Lett.* **2001**, *79*, 409.
- [Bra99] *Polymer Handbook*; Brandrup, J.; Immergut, E.H.; Grulke, E.A., Eds.; John Wiley & Sons, 1999.
- [Bru35] Bruggeman, D. A. G. *Ann. Phys.* **1935**, *24*, 636.
- [Car93] Carcano, G.; Ceriani, M.; and Soglio, F. *Hybrid Circuits*, **1993**, *32*, 12.
- [Ces93] Cesteros, L. C. ; Meaurio, E. ; Katime, I. *Macromolecules* **1993**, *26*, 2323.
- [Che2001] Cheng, J. Y.; Ross, C. A.; Chan, V. Z.-H.; Thomas, E. L.; Lammertink, R. G. H.; Vansko, G. J. *Adv. Mater.* **2001**, *13*, 1174.
- [Coh99] Cohen, R. E. *Curr. Opin. Solid state Mater. Sci.* **1999**, *4*, 587.
- [Coll95] Collaud, M.; Groening, P.; Nowak, S.; Schlapbach, L. In *Polymer Surface Modification: Relevance to Adhesion*; Mittal, K. L., Ed.; VSP, 1995; pp. 87–99.
- [Cou89] Coulon, G.; Russell, T. P.; Deline, V. R.; Green, P. F. *Macromolecules* **1989**, *22*, 2581.

- [Dan99] Dante, S.; Advincula, R.; Frank, C. W.; Stroeve, P. *Langmuir* **1999**, *15*, 193.
- [Elb2002] Elbs, H.; Drummer, C.; Abetz, V.; Krausch, G. *Macromolecules* **2002**, *35*, 5570.
- [Fas97] Fasolka, M. J.; Harris, D. J.; Mayes, A. M.; Yoon, M.; Mochrie, S. G. J. *Phys. Rev. Lett.* **1997**, *79*, 3018.
- [Fas2000] Fasolka, M. J.; Banerjee, P.; Mayes, A. M.; Pickett, G.; Balazs, A. *Macromolecules* **2000**, *33*, 5702.
- [För98] Förster, S. ; Antonietti, M. *Adv. Mater.* **1998**, *10*, 195.
- [För2002] Förster, S. ; Plantenberg, T. *Angew. Chem. Int. Edn.* **2002**, *41*, 688.
- [Fou51] Fournet, G. *Bull. Soc. Fr. Mineral. Crist.* **1951**, *74*, 37.
- [Fre87] Fredrickson, G. H. *Macromolecules* **1987**, *20*, 2859.
- [Fre87] Fredrickson, G. H.; Helfand, E. *J. Chem. Phys.* **1987**, *87*, 697.
- [Fre96] Fredrickson, G. H.; Bates, F. S. *Annu. Rev. Mater. Sci.* **1996**, *26*, 501.
- [Fre2001] Frey, P. A. *Magn. Res. Chem.* **2001**, *39*, S190.
- [Gei99] Geisinger, T.; Müller, M.; Binder, K. *J. Chem. Phys.* **1999**, *111*, 5241.
- [Gre2001] Green, P. F.; Limary, R. *Adv. Colloid Interface Sci.* **2001**, *94*, 53.
- [Gua2001] Guarini, K. W.; Black, C. T.; Milkove, K. R.; Sandstrom, R. L. *J. Vac. Sci. Technol. B* **2001**, *19*, 2784.
- [Gua2002] Guarini, K. W.; Black, C. T.; Yeung, S. H. I. *Adv. Mater.* **2002**, *14*, 1290.
- [Gua2002a] Guarini, K. W.; Black, C. T.; Yeung, S. H. I. *Adv. Mater.* **2002**, *14*, 1290.
- [Gua2002b] Guarini, K. W.; Black, C. T.; Zhang, Y.; Kim, H.; Sikorski, E. M. Babich, I. V. *J. Vac. Sci. Technol. B* **2002**, *20*, 2788.
- [Gur95] Gurovich, E. *Phys. Rev. Lett.* **1995**, *74*, 482.
- [Hah2001] Hahm, J.; Sibener, S. J. *J. Chem. Phys.* **2001**, *114*, 4730.
- [Haj94] Hajduk, D. A.; Harper, P. E.; Gruner, S. M.; Honeker, C. C.; Kim, G.; Thomas, E. L. Fetters, L. J. *Macromolecules* **1994**, *27*, 4063.
- [Haj97] Hajduk, D. A.; Takenouchi, M. A.; Hillmyer, M. A.; Bates, F. S.; Vigild, M. E.; Almdal, K. *Macromolecules* **1997**, *30*, 3788.
- [Ham2003] PhysloHamley, I. W. *Nanotechnology* **2003**, *14*, 39.
- [Ham94] Hamley, I. W.; Pederson, J. S. *Journal of Applied Crystallography* **1994**, *27*, 29.
- [Ham98] Hamley, I. W. *The physics of block copolymers*; Oxford University Press: Oxford, 1998.
- [Han2000] Hanley, K. J.; Lodge, T. P.; Huang, C.-I. *Macromolecules* **2000**, *33*, 5918.
- [Har2000] Harrison, C.; Adamson, D. H.; Cheng, Z.; Sebastian, J. M.; Sethuraman, S.; Huse, D. A.; Register, R. A.; Chaikin, P. M. *Nature* **2000**, *290*, 1558.

- [Har98a] Harrison, C.; Park, M.; Chaikin, P. M.; Register, R. A.; Adamson, D. H. *J. Vac. Sci. Techn. B* **1998**, *16*, 544.
- [Har98b] Harrison, C.; Park, M.; Chaikin, P.; Register, R. A.; Adamson, D. H.; Yao, N. *Macromolecules* **1998**, *31*, 2185.
- [Hau2003] Haupt, M.; Miller, S.; Glass, R.; Arnold, M.; Sauer, R.; Thonke, K.; Möller, M.; Spatz, J. P. *Adv. Mater.* **2003**, *15*, 829.
- [Hel76] Helfand, E.; Wasserman, Z. R. *Macromolecules* **1976**, *9*, 879.
- [Hol94] Holy, V.; Baumbach, T. *Phys. Rev. B* **1994**, *49*, 10668.
- [Hon83] Hong, K. M.; Noolandi, J. J. *Macromolecules* **1983**, *16*, 1083.
- [Hor2003] Horiuchi, S.; Fujita, T.; Hayakawa, T.; Nakao, Y. *Langmuir* **2003**, *19*, 2963.
- [Hua98a] Huang, C.-I.; Lodge, T. P. *Macromolecules* **1998**, *31*, 3556.
- [Hua98b] Huang, E.; Russell, T. P.; Harrison, C.; Chaikin, P. M.; Register, R. A.; Hawker, C. J.; Mays, J. *Macromolecules* **1998**, *31*, 7641.
- [Hua98c] Huang, E.; Rockford, L.; Russell, T. P.; Hawker, C. *Nature* **1998**, *395*, 757.
- [Hua99] Huang, E.; Pruzinsky, S.; Russell, T. P.; Mays, J.; Hawker, C. J. *Macromolecules* **1999**, *32*, 5299.
- [Hui2000] Huinink, H. P.; Brokken-Zijp, J. C. M.; van Dijk, M. A. *J. Chem. Phys.* **2000**, *112*, 2452.
- [Jia2001] Jiao, H.; Goh, S. H.; Valiyaveetil, S. *Macromolecules* **2001**, *34*, 7162.
- [Jef97] Jeffrey, G. A. *An Introduction to Hydrogen Bonding*; Oxford University Press: New York, 1997.
- [Jeo2001] Jeoung, E.; Gallow, T. H.; Schotter, J.; Bal, M.; Ursache, A.; Tuominen, M. T.; Stafford, C. M.; Russell, T. P.; Rotello, V. M. *Langmuir* **2001**, *17*, 6396.
- [Jeo2002] Jeoung, U.; Kim, H.-C.; Rodriguez, R. L.; Tsai, I. Y.; Stafford, C. M.; Kim, J. K.; Hawker, C. J.; Russell, T. P. *Adv. Mater.* **2002**, *14*, 274.
- [Kat92] Kato, T.; Kihara, H.; Uryu, T.; Fujishima, A.; Frechet, J. M. J. *Macromolecules* **1992**, *25*, 6836.
- [Kel96] Kellogg, G. J.; Walton, D. G.; Mayes, A. M.; Lambooy, P.; Russell, T. P.; Gallagher, P. D.; Satja, S. K. *Phys. Rev. Lett.* **1996**, *76*, 2503.
- [Ker90] Kern, W. *J. Electrochem. Soc.*, **1990**, *137*, 1887.
- [Kha95] Khandpur, A. K.; Förster, S.; Bates, F. S.; Zhao, J.; Ryan, A. J.; Bras, W.; Hamley, I. W. *Macromolecules* **1995**, *28*, 8796.
- [Kim2001] Kim, H.-C.; Russell, T. P. *J. Polym. Sci.* **2001**, *39*, 663.
- [Kim98a] Kim, G.; Libera, M. *Macromolecules* **1998**, *31*, 2569.

- [Kim98b] Kim, G.; Libera, M. *Macromolecules* **1998**, *31*, 2670.
- [Kim2000] Kim, H.-C.; Russell, T. P. *J. Polym. Sci. B* **2001**, *39*, 663.
- [Kop94] Koppi, K. A.; Tirrell, M.; Bates, F. S.; Almdal, K.; Mortensen, K. *J. Rheol.* **1994**, *38*, 999.
- [Kos2000] Koslowski, B.; Strobel, S.; Herzog, T.; Heinz, B.; Boyen, H. G.; Notz, R.; Ziemann, P.; Spatz, J. P.; Möller, M. *J. Appl. Phys.* **2000**, *87*, 7533.
- [Kra2002] Kraush, G.; Magerle, R. *Adv. Mater.* **2002**, *14*, 1579.
- [Kun93] Kunz, M. S.; Shull, K. R.; Kellock, A. J. *J. Coll. Int. Sci.* **1993**, *156*, 240.
- [Lam2000] Lammertink, R. G. H.; Hempenius, M. A.; van den Enk, J. E.; Chan, V. Z.-H.; Thomas, E. L.; Vansko, G. J. *Adv. Mater.* **2000**, *12*, 98.
- [Lec87] Leckner, J. *Theory of Reflection*; Martinus Nijhoff Publishers: Dordrecht, 1987.
- [Lee86] Lee, J. Y.; Painter, P. C.; Coleman, M. M. *Macromolecules* **1988**, *21*, 954.
- [Lee88] Lee, J. Y.; Moskala, E. J.; Painter, P. C.; Coleman, M. M. *Appl. Spectrosc.* **1986**, *40*, 991.
- [Lei80] Leibler, L. *Macromolecules* **1980**, *16*, 1602.
- [Li2000] Li, R. R.; Dapkus, P. D.; Thompson, M. E.; Jeong, W. G.; Harrison, C.; Chaikin, P. M.; Register, R. A.; Adamson, D. H. *J. Appl. Phys. Lett.* **2000**, *76*, 1689.
- [Lin2002] Lin, Zh.; Kim, D. H.; Wu, X.; Boosahda, L.; Stone, D.; LaRose, L.; Russell, T. P. *Adv. Mater.* **2002**, *14*, 1373.
- [Liu94] Liu, Y.; Zhao, W.; Zheng, X.; King, A.; Singh, A.; Rafailovich, M. H.; Sokolov, J.; Dai, K. H.; Kramer, E. J.; Schwartz, S. A.; Gebizlioglu, O.; Sinha, S. K. *Macromolecules* **1994**, *27*, 4000.
- [Liu2003] Liu, T.; Burger, C.; Chu, B. *Prog. Polym. Sci.* **2003**, *28*, 5.
- [Lod2003a] Lodge, T. P.; Hanley, K. J.; Pudil, B.; Alahapperuma, V. *Macromolecules* **2003**, *36*, 816.
- [Lod2003b] Lodge, T. P. *Macromol. Chem. Phys.* **2003**, *204*, 265.
- [Lop2001] Lopes, W. A.; Jaeger, H. M. *Nature* **2001**, *414*, 735.
- [Lop2002] Lopes, W. A. *Phys. Rev. E* **2001**, *65*, 031606.
- [Mag97] Magonov, S. N.; Elings, V. Whangbo, M.-H. *Surf. Sci.* **1997**, *375*, L385.
- [Mai92] Maier, E.E.; Krause, R.; Deggelmann, M.; Hagenbuchle, M.; Weber, R.; Fraden, S. *Macromolecules* **1992**, *25*, 1125.
- [Mäk2000] Mäkinen, R.; Ruokolainen, J.; Ikkala, O.; de Moel, K.; ten Brinke, G.; de Ododrico, W.; Stamm, M. *Macromolecules* **2000**, *33*, 3441.

- [Mäk2001] Mäki-Ontto, R.; de Moel, K.; de Odorico, W.; Ruokolainen, J.; Stamm, M.; ten Brinke, G.; Ikkala, O. *Adv. Mater.* **2001**, *13*, 117.
- [Man95] Mansky, P.; Chaikin, P.; Thomas, E. L. *J. Mater. Sc.* **1995**, *30*, 1987.
- [Man97] Mansky, P.; Liu, Y.; Huang, E.; Russell, T. P.; Hawker, C. *Science* **1997**, *275*, 1458.
- [Mat94] Matsen, M. W.; Schick, M. *Phys. Rev. Lett.* **1994**, *72*, 2660.
- [Mat96] Matsen, M. W.; Bates, F. S. *Macromolecules* **1996**, *29*, 1091.
- [Mat97] Matsen, M. W. *J. Chem. Phys.* **1997**, *106*, 7781.
- [Mat2001] Matsen, M. W. *J. Chem. Phys.* **2001**, *114*, 10528.
- [Max04] Maxwell-Garnett, J. C. *Philos. Trans. R. Soc. London A* **1904**, *203*, 385.
- [McR58] McRae, E.G.; Kasha, M. *J. Chem. Phys.* **1958**, *28*, 721.
- [Min2002] Minko, S.; Patil, S.; Datsyuk, V.; Simon, F.; Eichhorn, K.-J.; Motornov, M.; Usov, D.; Tokarev, I.; Stamm M. *Langmuir* **2002**, *18*, 289.
- [Mis2003] Misner, M. J.; Skaff, H.; Emrick, T.; Russell, T. P. *Adv. Mater.* **2003**, *15*, 221.
- [Mor90] Mori, K.; Hasegawa, H.; Hashimoto, T. *Polymer* **1990**, *31*, 2368.
- [Mor94] Morkved, T. L.; Wiltzius, P.; Jaeger, H. M.; Grier, D. G.; Witten, T. A. *Appl. Phys. Lett.* **1994**, *64*, 422.
- [Mor96] Morkved, T. L.; Lu, M.; Urbas, A. M.; Elrich, E. E.; Jaeger, H. M.; Mansky, P.; Russell, T.P. *Science* **1996**, *273*, 931.
- [Mor97] Morkved, T. L.; Jaeger, H. M. *Europhys. Lett.* **1997**, *40*, 643.
- [Mor2001] Morales, M. E.; Buschmann, V.; Dobrev, D.; Neumann, R.; Scholz, R.; Schuhert, I. U.; Vetter, J. *Adv. Mater.* **2001**, *13*, 62.
- [Mui79] *Handbook of X-ray and Ultraviolet Photoelectron Spectroscopy*; Muilenburg, G. E., Ed.; Physical Electronics Div., Perkin Elmer Corp.: Norwalk, 1979.
- [Mül2000] Müller-Buschbaum, P.; Gutmann, J. S.; Stamm, M.; Cubitt, R.; Cunis, S.; von Krosigk, G.; Gehrke, R.; Petry, W. *Physica B* **2000**, *283*, 53.
- [Mül98] Müller-Buschbaum, P.; Stamm, M. *Macromolecules* **1998**, *31*, 3686.
- [Mut97] Muthukumar, M.; Ober, C. K.; Thomas, E. L. *Science* **1997**, *277*, 1225.
- [Nai2002] Naito, K.; Hieda, H.; Sakurai, M.; Kamata, Y.; Asakawa, K. *IEEE Trans. Magn.* **2002**, *38*, 1949.
- [Nie2000] Nielsch, K.; Müller, F.; Li, A.-P.; Gösele U. *Adv. Mater.* **2000**, *12*, 582.
- [Par2001] Park, M.; Chaikin, P. M.; Register, R. A.; Adamson, D. H. *J. Appl. Phys. Lett.* **2001**, *79*, 257.
- [Par54] Parrat, L. G. *Phys. Rev.* **1954**, *55*, 359.

- [Par97] Park, M.; Harrison, C.; Chaikin, P. M.; Register, R. A.; Adamson, D. H. *Science* **1997**, *276*, 1401.
- [Per92] Perkampus, H.-H. *UV-VIS Spectroscopy and its Applications*; Springer; Berlin, 1992.
- [Pic97] Pickett, G. T.; Balazs, A. C. *Macromolecules* **1997**, *30*, 3097.
- [Roc99] Rockford, L.; Liu, Y.; Mansky, P.; Russell, T. P.; Yoon, M.; Mochrie, S. G. J. *Phys. Rev. Lett.* **1999**, *82*, 2602.
- [Ruo96] Ruokolainen, J.; ten Brinke, G.; Ikkala, O.; Torkkeli, M.; Serimaa, R. *Macromolecules* **1996**, *29*, 3409.
- [Ruo99] Ruokolainen, J.; Saariaho, M.; Ikkala, O.; ten Brinke, G.; Thomas, E. L.; Torkkeli, M.; Serimaa, R. *Macromolecules* **1999**, *32*, 1152.
- [Ruo98a] Ruokolainen, J.; Mäkinen, R.; Torkkeli, M.; Mäkelä, T.; Serimaa, R.; ten Birke, G.; Ikkala, O. *Science* **1998**, *280*, 557.
- [Rus89] Russell, T. P.; Coulon, G.; Deline, V. R.; Miller, D. C. *Macromolecules* **1989**, *22*, 4600.
- [Rya97] Ryan, A. J.; Hamley, I. W. In *The Physics of Glassy Polymers*; Haward, R. N.; Young, R. J., Ed.; Chapman & Hall: London, 1997.
- [Sän97] Sänger, J.; Gronski, W.; Maas, S.; Stühn, B.; Heck, B. *Macromolecules* **1997**, *30*, 6783.
- [Sch92] Schwark, D.; Vezie, D. L.; Reffner, J.; Annis, B.; Thomas, E. L. *J. Mater. Sci. Lett.* **1992**, *11*, 352.
- [Seg2001] Segelman, R. A.; Yokoyama, H.; Kramer, E. J. *Adv. Mater.* **2001**, *13*, 1152.
- [Seg2003] Segelman, R. A.; Hexemer, A.; Hayward, R. C.; Kramer, E. J. *Macromolecules* **2003**, *36*, 3272.
- [Sem92] Semenov, A. N. *Macromolecules* **1992**, *25*, 4967.
- [Shi2002] Shin, K.; Leach, K. A.; Goldbach, J. T.; Kim, D. H.; Jho, J. Y.; Tuominen, M. T.; Hawker, C. J.; Russell, T. P. *Nano Lett.* **2002**, *2*, 933.
- [Shi83] Shibayama, M.; Hashimoto, T.; Hasegawa, H.; Kawai, H. *Macromolecules* **1983**, *16*, 1427.
- [Sch96] Schulz, M. F.; Khandpur, A. K.; Bates, F. S.; Almdal, K.; Mortensen, K.; Hajduk, D. A.; Gruner, S. M. *Macromolecules* **1996**, *29*, 2857.
- [Sem85] Semenov, A. N. *Soviet Physics JETP*, **1985**, *63*, 70.
- [Spa96] Spatz, J. P.; Roescher, A.; Möller, M. *Adv. Mater.* **1996**, *8*, 337.
- [Spa97] Spatz, J. P.; Möller, M.; Noeske, M.; Behm, R. J.; Pietralla M. *Macromolecules* **1997**, *30*, 3874.

- [Spa99] Spatz, J. P.; Herzog, T.; Mössmer, S.; Ziemann, P.; Möller, M. *Adv. Mater.* **1999**, *11*, 149.
- [Sta92] Stamm, M. In *Physics of Polymer Surfaces and Interfaces*; Sanchez, I. C., Ed.; Butterworth-Heinemann Publ.: Boston, 1992.
- [Stö2000] Stöhr, J.; Anders, S. *IBM J. Res. Develop.* **2000**, *44*, 535.
- [Thu2000a] Thurn-Albrecht, T.; Derouchey, J.; Russell, T. P.; Jaeger, H. M. *Macromolecules* **2000**, *33*, 3250.
- [Thu2000b] Thurn-Albrecht, T.; Schotter, J.; Kästle, A.; Emley, N.; Shibauchi, T.; Krusin-Elbaum, L.; Guarini, K.; Black, C. T.; Tuominen, M. T.; Russell, T. P. *Science* **2000**, *290*, 2126.
- [Thu2000c] Thurn-Albrecht, T.; Steiner, R.; DeRouchey, J.; Stafford, C. M.; Huang, E.; Bal, M.; Tuominen, M.; Hawker, C. J.; Russell, T. P. *Adv. Mater.* **2000**, *12*, 787.
- [Tol99] Tholan, M. *X-ray Scattering from Soft-Matter Thin Films. Springer Tracts in Modern Physics. Vol. 148*; Springer-Verlag: Berlin, 1999.
- [Ves93] Vesenka, J.; Manne, S.; Giberson, R.; Marsh, T.; Henderson, E. *Biophysical J.* **1993**, *65*, 992.
- [Vis2002] Vishweshwar, P.; Nangia, A.; Lynch, V. M. *J. Org. Chem.* **2002**, *67*, 556.
- [Vis2003] Vishweshwar, P.; Nangia, A.; Lynch, V. M. *J. Org. Chem.* **2003**, *5*, 164.
- [Wan2001] Wang, Q.; Nealey, P. F.; de Pablo, J. *Macromolecules* **2001**, *34*, 3458.
- [Whi92] Whitmore, M. D.; Vavasour, J. D. *Macromolecules* **1992**, *25*, 2041.
- [Yan2000] Yang, X. M.; Peters, R. D.; Nealey, P. F.; Solak, H. H.; Cerrina, F. *Macromolecules* **2000**, *33*, 9575.
- [Yon63] Yoneda, Y. *Phys. Rev.* **1963**, *131*, 2010.
- [Zeh98] Zehner, R. W.; Lopes, W. A.; Morkved, T. L.; Jaeger, H.; Sita, L. R. *Langmuir* **1998**, *14*, 241.
- [Zeh99] Zehner, R. W.; Sita, L. R. *Langmuir* **1999**, *15*, 6139.
- [Zha96] Zhao, J.; Majumdar, B.; Schulz, M. F.; Bates, F. S.; Almdal, K.; Mortensen, K.; Hajduk, D. A.; Gruner, S. M. *Macromolecules* **1996**, *29*, 1204.

Appendix A. List of publications

Publications and patents

1. Minko, S.; Patil, S.; Datsyuk, V.; Simon, F.; Eichhorn, K.-J.; Motornov, M.; Usov, D.; Tokarev, I.; Stamm, M. Synthesis of Adaptive Polymer Brushes via “Grafting To” Approach from Melt. *Langmuir* **2002**, *18*, 289-296.
2. Draper, J.; Luzinov, I.; Tokarev, I.; Minko, S.; Stamm, M. Morphology and Wettability of Mixed Polymer Brushes. *Polym. Mater. Sci. Eng.* **2002**, *87*, 187-188.
3. Tokarev, I.; Minko, S.; Stamm, M. Hairy Tube" Polymer Templates From Diblock Copolymer Thin Films. *MRS Proc.* **2002**, *728*, 11-16.
4. Sidorenko, A.; Tokarev, I.; Minko, S.; Stamm M. Ordered Reactive Nanomembranes/ Nanotemplates from Thin Films of Block Copolymer Supramolecular Assembly. *J. Am. Chem. Soc.* **2003**, *125*, 12211-12216.
5. Sidorenko, A.; Tokarev, I.; Minko, S.; Stamm, M. Novel Supramolecular Approach to Periodic Nanostructures in Thin Polymer Films. *Polym. Mater. Sci. Eng.* **2003**, *89*, 115-116.
6. Minko, S.; Stamm, M.; Sydorenko, O.; Tokarev, I. Method for Producing Nanostructured Surfaces and Thin Films. Patent WO 03/101628 A1 **2003**.
7. Sidorenko, A.; Tokarev, I.; Krenek, R.; Burkov, Y.; Schmeisser, D.; Minko, S.; Stamm M. Generation of Nanostructured Materials from Thin Films of Block Copolymer Assemblies. Submitted to *Adv. Eng. Mat.* **2003**.
8. Stamm M.; Minko, S.; Tokarev, I.; Fahmi, A.; Usov, D. Nanostructures and Functionalities in Polymer Thin Films. *Macromol. Symp.* **2004**, *214*, 73-84.
9. Tokarev, I.; Sidorenko, A.; Minko, S.; Stamm M. Switching Nanotemplates. *Polym. Mater. Sci. Eng.* **2004**, *90*, 292-293.
10. Draper, J.; Luzinov, I.; Minko, S.; Tokarev, I.; Stamm, M.; Mixed Polymer Brushes by Sequential Polymer Addition: Anchoring Layer Effect. *Langmuir* **2004**, *20(10)*, 4064-4075.

Contribution to academic conferences

1. Tokarev, I.; Sidorenko, A.; Motornov, M.; Minko, S.; Stamm, M. Nanoporous Membranes and Patterned Surfaces from Block Copolymers (poster) *SMARTON 5 Workshop ,Functional Surfaces and Materials. Exploring the Vectorial World'*, Kasteel Vaeshartelt Maastricht, The Netherlands, November 15-18, 2001.
2. Tokarev, I.; Sidorenko, A.; Minko, S.; Stamm, M. Nanotemplates and nanoporous membranes from block copolymers (poster) *66th Frühjahrstagung der DPhG*, Regensburg, March 10-15, 2002.
3. Tokarev, I.; Minko, S.; Stamm, M. "Hairy Tube" Polymer Templates From Diblock Copolymer Thin Films (poster) *American Material Research Society Spring Meeting*, San Francisco, USA, April 2-4, 2002.
4. Tokarev, I.; Sidorenko, A.; Minko, S.; Stamm, M. Organized array of metallic nanoclusters via self-organization of block-copolymers (poster) *International Workshop on Nanostructures for Electronics and Optics (NEOP)*, Dresden, October 6-9, 2002.
6. Tokarev, I.; Sidorenko, A.; Minko, S.; Stamm, M. Nanotemplates from block copolymers for fabrication of regular arrays of nanowires and nanodots (poster) *Discussion Meeting on Multi-level Ordering 'Molecular Organization for Nanosystems'*, Kloster Banz, February 15-20, 2003.
7. Tokarev, I.; Sidorenko, A.; Minko, S.; Stamm, M. Nanotemplates based on block copolymer assemblies (poster) *67th Frühjahrstagung der DPhG*, Dresden, March 24-28, 2003.
8. Tokarev, I.; Sidorenko, A.; Minko, S.; Stamm, M. Switching nanotemplates (oral) *227th ACS National Meeting*, Anaheim, California, March 28 - April 1, 2004.

Appendix B. Acknowledgement.

I gratefully acknowledge Prof. Dr. Manfred Stamm for giving an opportunity to carry out this work, Prof. Dr. Sergiy Minko and Dr. Alexander Sydorenko for scientific supervision.

I would like to thank my colleagues Dr. Dieter Jenichen and Torsten Hofmann for technical assistance during the X-ray reflectivity measurements, Dr. Mirko Nitschke who helped me to perform the plasma etching experiments, Dr. Klaus-Jochen Eichhorn, Gudrun Adam and Dr. Hartmut Komber who measured and helped with interpretation of the infrared and ^1H NMR spectra.

The GISAXS measurements on the beamlines BW4 and A2 (HASYLAB at DESY, Hamburg) could not be carried out without assistance of Dr. Nadja Hermsdorf (IPF Dresden), Dr. Peter Müller-Buschbaum (TU München), Dr. Sabina Cunis, Dr. Rainer Gehrke, Dr. Sergio Funari, Dr. Andreas Meyer (HASYLAB). I am very grateful to all them.

I express thanks to Prof. Dr. Dieter Schmeisser and Yevgen Burkov (BTU Cottbus) for giving an opportunity to perform the XPEEM measurements on the beamline U49/2-PGM2 (Bessy-II, Berlin) and for valuable discussions.

BMBF (grant 05KS1BPA/4) is gratefully acknowledged for financial support.

I am also grateful to my colleagues Mikhail Motornov, Pylyp Volodin, Radim Krenek, Dr. Anton Kiriya, Denys Usov, Leonid Ionov, Anna Gorodyska, Nikolay Houbenov for help during experiments, stimulating discussions and friendliness.

My special thanks to my parents and friends who countenance me during my stay in Dresden.

Appendix C. Versicherung.

Hiermit versichere ich, dass ich die vorliegende Arbeit ohne unzulässige Hilfe Dritter und ohne Benutzung anderer als der angegebenen Hilfsmittel angefertigt habe; die aus fremden Quellen direkt oder indirekt übernommenen Gedanken sind als solche kenntlich gemacht. Die Arbeit wurde bisher weder im Inland noch im Ausland in gleicher oder ähnlicher Form einer anderen Prüfungsbehörde vorgelegt.

Die vorliegende Arbeit wurde unter der wissenschaftlichen Betreuung von Prof. Dr. Manfred Stamm und Prof. Dr. Sergiy Minko am Institut für Polymerforschung Dresden e. V. angefertigt.

Die Promotionsordnung der Technischen Universität Dresden der Fakultät Mathematik und Naturwissenschaften erkenne ich an.

Ihor Tokarev